3D Cell Shape Dynamics in *Drosophila* Wound Repair

Shu En Lim

Laboratory for Molecular Cell Biology

University College London

Thesis submitted for the degree of

Doctor of Philosophy

In

Developmental Biophysics

August 2025

Declaration

I, Shu En Lim, confirm that the work presented in this thesis is my own. Where information has been derived from other sources, I confirm that this has been indicated in the thesis.

Abstract

Epithelial tissues must repair wounds quickly and accurately to minimise damage and preserve organ function. Wound healing requires complex coordination of internal cell behaviours and their external environment, the basement membrane (BM), to close the gap. While the mechanisms behind wound healing in 2D epithelial sheets are well-studied, how cells change shape in 3D, particularly along the apicobasal axis, is less known. The *Drosophila* wing disc is composed of approximately 50μm tall cells encased by BM offers an ideal wound healing model to investigate 3D cell behaviours.

This thesis aims to investigate 3D cell behaviours driving wound repair. My work builds on previous experiments in the lab that proposed a new 3D wound healing mechanism in which cell shortening accelerates wound closure by allowing cells to expand into the wound gap. We hypothesise that contractile lateral actomyosin cables in wound edge cells drive cell shortening.

Using laser ablation, live imaging and quantitative analysis, I investigate how lateral cables form and their possible roles in *Drosophila* wing disc wound repair. I further quantified wound edge cell shape changes during repair and explored improvements to image the 3D molecular structure of lateral cables. Next, I examined the use of FRET-based tension sensors to measure forces during wound repair. I encountered experimental and technical challenges suggesting that these sensors are unsuitable to measure apicobasal forces in wounded *ex vivo* wing discs. Then, I genetically perturbed a variety of actomyosin-associated regulators to identify molecular regulators of lateral cable assembly. Finally, I removed BM at the wound site before wounding which appeared to alter cell shape in healing cells around the wound. Altogether, my work provides new insights into the possible molecular and mechanical mechanisms, both intracellular and extracellular, behind 3D cell shape changes during wound repair.

Impact Statement

This work bridges the gap between cell biology, biophysics, tissue engineering and regenerative medicine, offering implications for both healthcare and scientific advancement. At the fundamental level, this work provides crucial insights into the complex mechanisms that drive wound healing. These insights can deepen our understanding of the biochemical and mechanical crosstalk involved in tissue regeneration. This work has also identified key bottlenecks in the imaging and analysis of subcellular structures in the context of complex live 3D tissues, which may aid the development of advanced microscopy and computational techniques.

From a clinical perspective, understanding how 3D cell shape changes are driven during wound healing can aid the design of targeted interventions that accelerate healing, reduce scarring, and minimise complications such as infection. Such solutions may range from novel biomaterials or scaffolds to improve the natural wound healing environment to new drugs to alter cell or extracellular matrix properties, or gene therapies targeting aberrant genes or modulating key biological pathways involved in wound repair to prevent the onset of wound healing diseases. Ultimately, these advancements aim to enhance patients' quality of life.

This knowledge forms the foundation for developing more effective treatments for wounds, a significant burden on healthcare systems worldwide. Wound management is estimated to cost the NHS £8.3 billion a year (2017/18), and 50% of community nurse time [1]. By delivering more efficient and cost-effective care, we can reduce healthcare costs associated with prolonged treatments and hospitalisations while ensuring faster healing and minimising resource consumption. This will not only improve patient outcomes but also contribute to a more equitable healthcare system.

Acknowledgements

Thank you, Prof Yanlan Mao, for your support and guidance for the past four years. I am extremely grateful for your mentorship and for welcoming me into your wonderful lab.

Thank you to my second supervisor, Dr Sabrina Simoncelli, and my thesis committee, Prof Sophie Acton, Prof Guillaume Charras & Prof Franck Pichaud, for helpful discussions.

Thank you to Dr Helen Weavers and Dr Mie Wong for taking the time to read and examine my thesis.

Thank you to the LMCB core staff for your care of the building and equipment. Ki, for training me on my first microscope!

Thank you to the past and present members of the Mao lab. Sam, for defending the lab from floods and mites. Ricardo, for patient explanations of fly genetics. Nargess, for your ablation guidance and kind words when I was a shrimp. Giulia, for reminding me to un-shrimp, encouraging advice and head pats. Veronika, for exposing me to morning exercise. Lady Katherine, for sweet treat chatties and fashion love. Martin, for segmentation summer and contributing to this thesis! Elder Rob Tetley, for expanding my world and microscopy mentorship. I'm grateful for your pioneering lateral cable experiments! Pablito, por tu entusiasta y honesto apoyo desde la primera día. Estoy realmente agradecida de que estés en mi vida. FTWD. Alé, mi dama, por ayudarme a darle sentido al mundo dentro y fuera del laboratorio y por ser los últimos juntos en la pista de baile. Jimmy, for always picking up the phone and yapping anywhere in the world - weaaow weaaow weeaow. Thank you both for putting in a word for me.

Thank you to friends across the LMCB, Fish Floor and climbing community. Courtney, for your companionship from Day 1 Franco Manca and for supplying top-tier cats. Bailey, for benchtop debriefs and being my first LMCB friend. Esteemed friend Delan, for teaching me Inkscape shortcuts and front-row support. Thank you to my flatmates Vanda, Aleks, Stephen & Ed for motivation. Thank you to Maddy for taking me on long uphill walks.

Merci beaucoup Kayvan, pour tes doux mots d’encouragement et ta beta.

婆婆，多謝你一直以來給我煲美好的食物。同時你的笑容給了我無限量的支持。我會繼續努力下去。衷心的感謝你。

Thank you to my Mum for your unwavering support and cheer. This thesis is dedicated to you.

Figure 0: Dr Siew Fung Lee,

UCL Institute of Education 2014-2018

Dr S.F. Lee has granted permission for the use of this photograph.

Contents

List of Figures

List of Tables

Abbreviations

1P: One-photon

2P: Two-photon

AEL: after egg laying

AJ: Adherens junction

BM: Basement membrane

BSA: Bovine serum albumin

Cg: collagen

DNA: deoxyribonucleic acid

DN: dominant negative

E-cad: E-cadherin

ECM: Extracellular Matrix

EMT: epithelial mesenchymal transition

ExM: Expansion Microscopy

FBS: Fetal Bovine Serum

FLIM: Fluorescence Lifetime Imaging Microscopy

FRET: Förster resonance energy transfer

GAL4: Galactose-responsive transcription factor

GAP: Rho Guanosine Triphosphate activating protein

GEF: Rho Guanine nucleotide exchange factor

HyD: Hybrid detector

JNK: Jun N-terminal kinase

LC: Lateral cable

LINC: Linker of nucleoskeleton and cytoskeleton

Mbs: Myosin binding subunit

MHC: Myosin heavy chain

MRLC: Myosin regulatory light chain

Myr: myristoylated

Mys: myospheroid

Nub: nubbin

PBS: Phosphate-buffered saline

PBT: Phosphate buffer saline/0.3% Triton X-100

PCR: Polymerase chain reaction

PFA: Paraformaldehyde

Pro-ExM: Protein retention expansion microscopy

Pro-K: Proteinase-K

PS: Purse string

px: pixel

RNAi: Ribonucleic acid interference

ROI: region of interest

Rok: Rho-kinase

RT: Room temperature

SD: standard deviation

Shi^{TS}: shibire temperature sensitive

Sqh: spaghetti squash

TS: Tension sensor

UAS: Upstream Activation Sequence

Vkg: Viking

1 Introduction

1.1 Epithelial tissue morphology and function

1.1.1 Epithelial cell shape and organisation

Epithelial tissues are continuous cell sheets that cover and line organs, glands, and body cavities. These cells adopt different shapes and can be single or multi-layered depending on their function (Figure 1.1.A) [2,3]. For example, a single layer of flat squamous cells lines blood vessels and the lungs to allow for fast gaseous exchange between their lumen and surrounding tissues. In contrast, tall columnar cells lining the gastrointestinal tract secrete mucus to protect the lining from digestive enzymes and acid. Multilayered or stratified epithelia, such as the skin epidermis, mostly assume protective roles, enduring abrasions from the external environment.

To achieve such diverse functions, epithelial cells are polarised into structurally and functionally distinct domains (Figure 1.1.B). As a tissue develops, cells must maintain the correct cell polarity for cells to assume the correct shape and size. The apical domain faces the external environment or lumen, the lateral domain opposes neighbouring cells, and the basal domain lies on an underlying sheet of extracellular matrix (ECM) called the basement membrane (BM). These domains polarise the cell through asymmetric distribution of membrane phospholipids, contacts with the external cell environment and localised recruitment of specific proteins, including the cytoskeleton. This polarisation of cellular components creates a mechanical gradient within the cell, which influences cell shape and stiffness. For instance, atomic force microscopy of live fibroblasts has shown that the stiffness of curved actin bundles at the cell edge correlates with their curvature radius [4]. Similarly, during migration, cells generate a rearward mechanical gradient via actomyosin contractility with high cortical tension at the cell rear and low tension at the leading edge [5]. In tissue morphogenesis, apical constriction during *Drosophila* gastrulation provides another example of how the accumulation of actomyosin at the apical

surface increases local tension relative to the basal side, causing cells to constrict apically and change shape [6].

The cytoskeleton, particularly the actin network, plays a pivotal role in determining cell shape (Figure 1.1.C). This network is organised into an actin cortex beneath the cell membrane, whose structure and composition generate a cortical tension that controls the mechanics of the cell surface (Figure 1.1.C-D) [7]. Furthermore, cell volume is influenced by water permeation and ion exchange across the membrane, which together create an intracellular pressure [8].

In addition to internal forces, cells are subject to external forces arising from neighbouring cells, the extracellular matrix, and interstitial fluid. The actin cortex is tethered via adapter proteins to neighbouring cells through adhesions at cell-cell junctions [9,10] (Figure 1.1.D) and to the external environment through cell-BM adhesions [11] (Figure 1.1.E). These external forces can compress or stretch the cell, leading to adaptive changes in cortical tension and actin organisation [7].

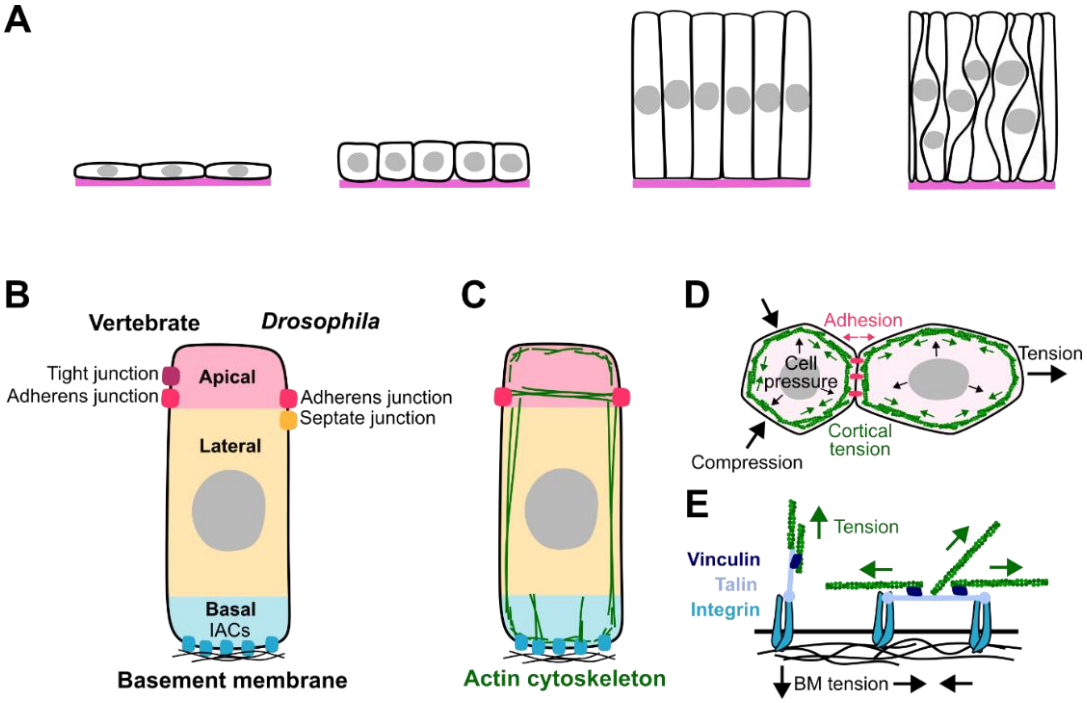

Figure 1.1 Epithelial cell shape and organisation.

A) Different types of cell shapes in epithelial tissue. From left to right: squamous, cuboidal, simple columnar and pseudostratified columnar. B)

Organisation of apical, lateral and basal domains and junctions in vertebrate and *Drosophila* epithelial cells. IAC: Integrin adhesion complex (blue squares). C) Organisation of the actin cytoskeleton (green) in epithelial cells. D) Internal and external factors contribute to cell shape. Actin filaments are represented in green. E) Epithelial cells form mechanosensitive contacts with the basement membrane (BM, black lines) via IACs with core proteins Vinculin (navy), Talin (pastel blue) and Integrin (blue).

1.1.2 Actomyosin cytoskeleton

The actomyosin cytoskeleton generates the mechanical forces required to shape and move cells [12–14]. It is composed of globular actin monomers that polymerise into filamentous actin and the motor protein non-muscle myosin II (NMII), referred to as myosin. Actin filaments are polarised with a fast-growing plus end favouring polymerisation and a slow-growing minus end favouring depolymerisation (Figure 1.2.A) [13]. Different actin-binding proteins can assemble filaments into parallel or anti-parallel linear bundles or branched networks. These networks can form specialised structures such as contractile rings, lamellipodia or filopodia that facilitate cell movement [12,13]. Myosin is composed of two heavy chains and four light chains, organised into head, neck and tail domains [14]. The tail domain binds cargo or polymerises with other myosin subunits. The head domain binds to f-actin and adenosine triphosphate (ATP). It has an ATPase to hydrolyse ATP to provide energy for a conformational change in myosin via its neck domain to move the head domain along an actin filament [15]. The head domain also contains two essential light chains (ELC) and two regulatory light chains (RLC). ATPase activity is controlled by the phosphorylation of the myosin regulatory light chain. Myosin can dimerise, forming a pair of antiparallel molecules. Dimers can then assemble into large filaments termed mini filaments (Figure 1.2.B). Actomyosin contraction is generated by myosin pulling two actin filaments together (Figure 1.2.C). Myosin motor activity is required for generating subcellular contraction for apical constriction and to generate tension to fold tissues in *Drosophila* morphogenesis [16].

The activity of the actomyosin is tightly regulated by various signalling pathways, including those involving kinases, phosphatases and G-proteins, as summarised in Figure 1.2.D. Key kinases such as myosin light chain kinase (MLCK) and Rho kinase (ROCK) phosphorylate MRLC to promote actomyosin contraction [17–19]. Conversely, the dephosphorylation of MRLCs by myosin phosphatase can inhibit myosin activity [20]. ROCK can also phosphorylate and activate Lin-11, Isl-1, and Mec-3 kinase (LIMK), which phosphorylates cofilin, an actin depolymerising protein [21]. However, phosphorylated cofilin inhibits its depolymerising activity, promoting stable actin filaments.

These kinases can be activated by upstream activators from the Rho family [22]. These are a family of small GTPases that act as molecular switches through alternating between GDP- and GTP-bound forms. This switching is mediated by Rho GTPase-activating proteins (GAP) and Rho GTPase exchange factors (GEF). Rho GTPases can also activate actin regulators such as Diaphanous (Dia), a formin which regulates the nucleation of linear actin filaments [23,24]. GEFs are activated by G-protein-coupled receptors (GPCRs) by extracellular ligand-binding. The organisation of the actomyosin cytoskeleton can also be indirectly or directly controlled by cell-cell junctions and cell-matrix adhesions.

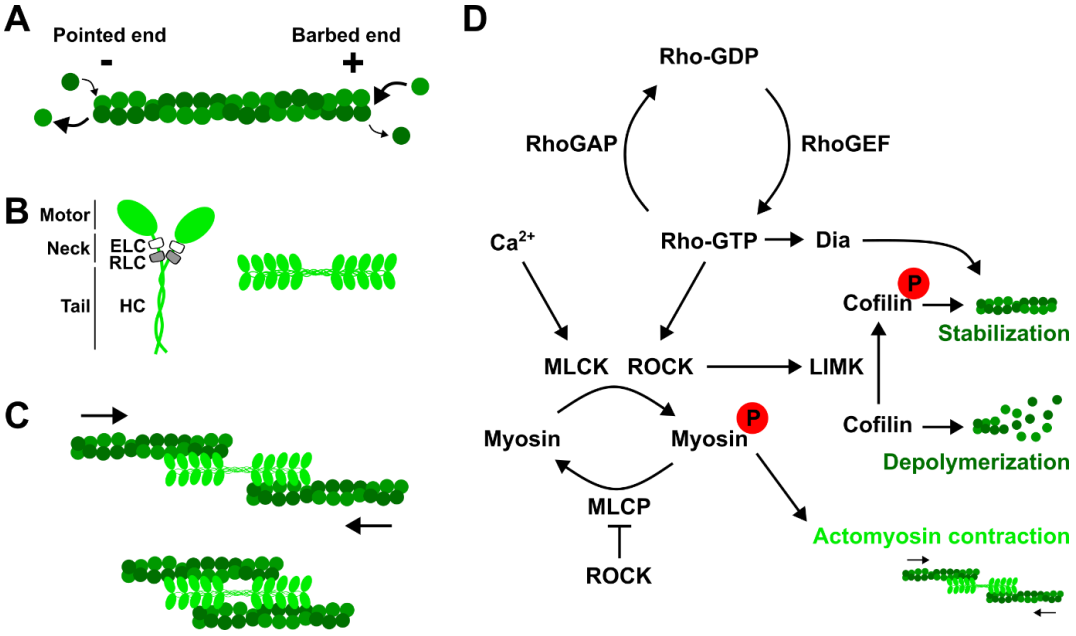

Figure 1.2: Actomyosin structure and function.

A) Actin filament structure. B) Non-muscle Myosin II structure and Myosin mini filament. ELC: Essential light chain. RLC: Regulatory light chain. HC: Heavy chain. C) Myosin mini filaments bind to actin filaments and contract to move actin filaments.

1.1.3 Cell Adhesions

Cells form contacts with neighbouring cells via cell-cell junctions and with the underlying BM via cell-BM adhesions [10,11]. These contacts act as important biochemical and mechanical signalling hubs. Positioned at the apical domain, cell-cell junctions are multiprotein complexes that facilitate mechanical integrity, transcriptional regulation and intracellular communication. A major type of cell-cell junction is the Adherens junctions (AJs), which lie at the boundary of the cell's apical and lateral domains. Epithelial AJs are composed of transmembrane E-cadherin clusters whose extracellular domains bind to other E-cadherins from neighbouring cells [10,25]. Their cytosolic tail domains bind to β-catenin, α-catenin and p120-catenin that link to the actin cytoskeleton directly and indirectly via vinculin or other actin-binding proteins [10,25]. Other cell-cell junctions, such as tight junctions in vertebrates or septate junctions in *Drosophila,* create seals between neighbouring cells [10].

At the basal domain, Integrins form core components of cell-BM adhesions and are highly conserved across all multicellular animals [11,26]. Upon activation to ligands either outside or inside the cell, integrin recruits other proteins and additional integrins to form heterogeneous multiprotein signalling centres known as integrin adhesion complexes (IACs). Integrins are heterodimeric proteins formed of an α and a β subunit. Both subunits consist of an extracellular globular head domain, a single transmembrane domain and a tail domain. Integrins follow a stepwise activation from an inactive bent closed conformation to an intermediate extended closed conformation and finally an extended open conformation with an increased affinity for extracellular ligands and clustering activity [27,28]. Integrin can bind several components of the BM, for example, Collagen IV and Laminin, via its extracellular head region [11]. This binding can activate "outside-in"

signalling cascades in the cell. Integrin's intracellular tail region can bind a variety of proteins, notably the mechanosensitive adapter Talin [11].

Talin is composed of an N-terminal four-point-one, ezrin, radixin, moesin (FERM) head domain joined via a flexible linker to a C-terminal rod domain consisting of 13 helical bundles and a dimerisation domain (DD). There are two integrin binding sites: integrin binding site 1 (IBS1) in the head domain and integrin binding site 2 (IBS2) in the rod domain [29]. There are 3 actin-binding regions located at the head region, the centre of the rod domain and at the C-terminal [30]. Talin can dimerise via its C-terminal DD. As such, each talin homodimer may bind four integrin heterodimers and multiple actin filaments. When inactive, Talin exists as compact autoinhibited dimers in the cytoplasm, where the rod domain covers the integrin binding site 1 on the head domain [31] (Figure 1.3). Recruitment of Talin to the plasma membrane is regulated by GTPase Rap1 and membrane lipid phosphatidylinositol 4,5-bisphosphate (PIP_2) [32,33]. PIP_2 binding induces a conformational change to expose IBS1, which will subsequently bind the integrin β subunit. Upon talin binding, inactive closed integrin unfolds into its extended closed conformation and can be further activated via tension known as "inside out signalling" (Figure 1.3). Talin responds to tension exerted by actin through the reversible unfolding of the helical bundles in its rod domain [34]. This conformational change can reveal cryptic binding sites, such as those for vinculin (Figure 1.3). Other proteins, such as vinculin, kindlin and paxillin, can be recruited to enhance integrin-talin binding and activation [35].

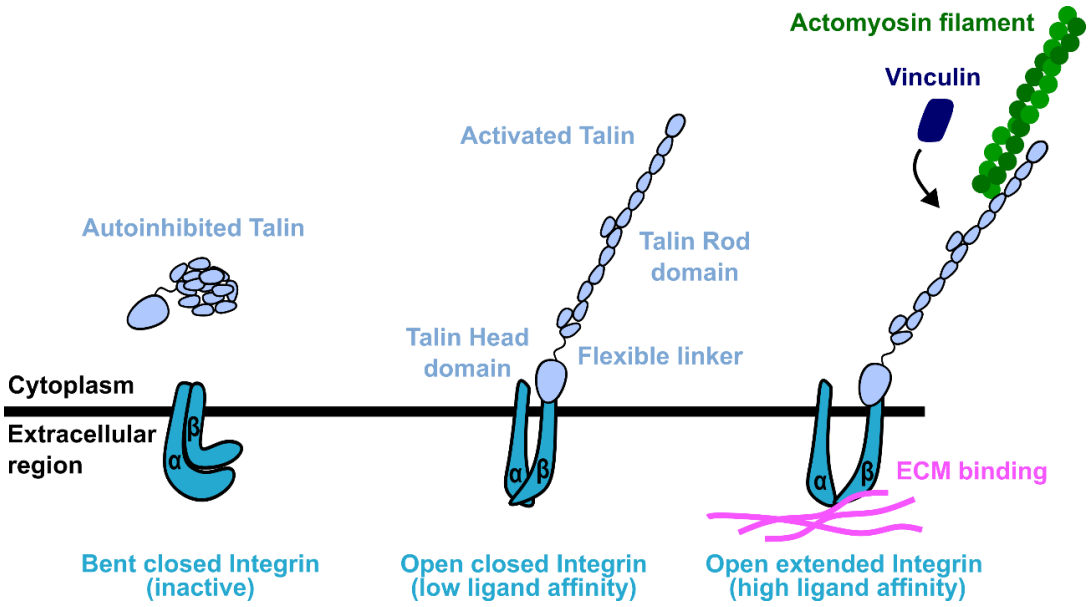

Figure 1.3: Integrin Adhesion Complex

Left: Integrin (blue) in a bent closed conformation, unbound to any partners or ligands. Talin (pastel blue) is in an autoinhibited closed conformation in the cytoplasm. Its large globular head is attached to the rod domain via a flexible linker. Middle: When Talin is activated, it unfolds and binds to Integrin. Integrin changes to an open closed conformation. Right: When activated via tension from the actomyosin cytoskeleton (green) bound to Talin, Integrin changes to its open extended conformation. Tension across Talin may open cryptic binding sites to allow additional binding partners, such as vinculin (navy), to join the growing integrin adhesion complex. Alternatively, Integrin can be activated by binding to ECM ligands (pink).

1.1.4 The basement membrane

The basement membrane is a specialised extracellular matrix sheet underlying all epithelial cells. Their emergence coincides with the evolution of multicellular animals, and their main constituents are highly conserved [36]. The basement membrane is a mechanical scaffold, physical barrier and biochemical signalling platform with roles in tissue morphogenesis and disease [37,38]. All basement membranes contain Collagen IV, Laminin, Perlecan and Nidogen (Figure 1.4) [36,39]. Collagen IV is the most abundant component of the BM and forms a non-fibrillar multilayered sheet. Each Collagen IV molecule is composed of heterotrimeric α chains that can form a

tetramer with other Collagen IV molecules (Figure 1.4, purple). The Collagen IV network associates with a network of Laminin, a heterotrimer protein composed of α, β, and γ chains (Figure 1.4, blue). The glycoprotein Nidogen (Figure 1.4, green) and the heparan sulphate glycoprotein Perlecan (Figure 1.4, magenta) link to both the Laminin and Collagen IV networks, as well as each other. The BM is remodelled by matrix metalloproteinases (MMPs), which are regulated by tissue inhibitors of metalloproteinases (TIMPs) [40,41].

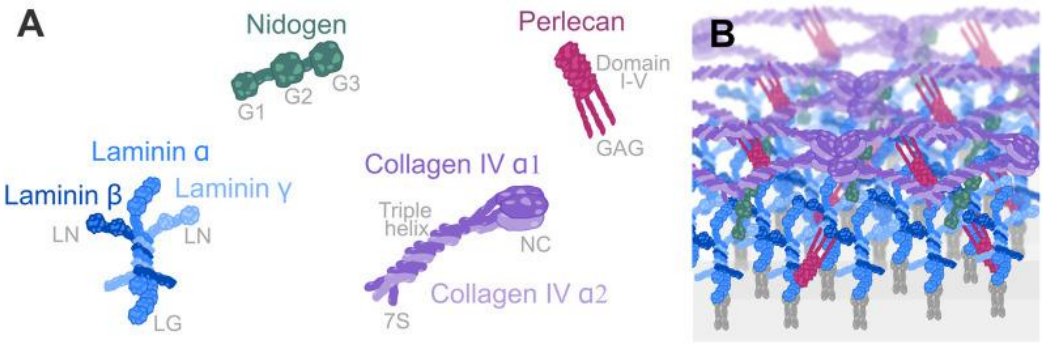

Figure 1.4: Basement membrane structure and composition.
Adapted from [38].

1.2 Wound repair in epithelial tissues

As the first tissues to be exposed to damaging external stimuli, epithelia must be able to repair efficiently and accurately to maintain the structure and function of their underlying organs. Damaging stimuli may come in the form of physical damage, pathogens, noxious chemicals or radiation in the natural lifetime of any living organism. Failure to prevent further damage will result in disease. Many pathological factors can disrupt wound healing, and conversely, disrupted wound healing, either under- or over-healing, may cause further infection or disease.

When wounds repair too slowly or even completely fail to re-epithelialize, chronic wounds can arise. Vascular insufficiency, diabetes, neuropathies, immobility, and ageing are risk factors for increased susceptibility to impaired wound healing [42–44]. Alternatively, fibrosis results from over-healing, where healthy tissue is replaced with excessive accumulation of ECM components, particularly Collagen, resulting in hypertrophic or keloid scars in

the skin [45,46]. Fibrosis of internal organs can cause hardening and blockages, eventually leading to organ malfunction as seen in diseases such as Crohn's disease [47], idiopathic pulmonary fibrosis [48], and liver fibrosis [49].

Even when fully healed, the scarred tissue never regains its original strength or flexibility. Keloid tissues are approximately 10-fold stiffer than normal skin tissue [50]. In contrast, embryonic tissues heal seamlessly, without scarring or inflammation [51,52]. Instead, experimentally induced inflammation induces scarring, such as seen in fetal rabbit wounds [53].

In developing tissues, a continuous epithelium is important to maintain correct tissue patterning. Tissue patterning instructs cells on how to self-organise through cell growth, migration, and differentiation, giving rise to highly precise and reproducible tissues. These patterns result from the interplay between fate-determining genes, biochemical cues [54–56] and mechanics [57–60]. A gap in the epithelia can disrupt these patterns, inducing morphological defects or fatality.

Identifying the tissue intrinsic mechanisms behind seamless healing in developing tissues may suggest ways in which to recapitulate more efficient healing in adults. Treatment of impaired healing is challenging, as wound healing is a highly complex and dynamic process, in addition to pre-existing comorbidities and lifestyle factors [61]. Many diverse cell types and signalling molecules are tightly coordinated within four main steps in response to tissue wounds: haemostasis, inflammation, proliferation, and remodelling [62,63]. As such, it is difficult to study the epithelium in isolation from extrinsic factors such as the immune system and simplified systems are needed to do this. Various adult and embryonic epithelial systems have been used to study wound healing, from mammalian cell cultures [64–68], 3D organoids [69–71], tissue explants [72] to whole organisms [73–78]. Such studies have shown that across model organisms, many signalling pathways and cellular behaviours driving wound healing are highly conserved in humans.

Regardless of the participating signalling pathways or cell types involved, wound closure must involve the mechanical movement of cells to close a

physical gap. When epithelia are wounded, BM, together with epithelial cells, undergo biochemically and mechanically driven changes to coordinate wound closure [62].

1.2.1 Mechanics in Wound Repair

Upon wounding, cell membranes are physically damaged, disrupting cell-cell junctions and consequently interrupting cellular tension. The causes of such damage may range across chemical, thermal and mechanical sources depending on how the wound was created. When tissues are wounded by laser ablation, cells experience a radius of different types of damage, ranging in severity [79]. The choice of wound healing mechanism is affected by the model system, type of damage and wound size [80].

Wound healing can be divided into three phases defined by wound area changes: expansion, fast closure, and slow closure, where different mechanisms dominate each phase. During expansion, tissue tension is released at the wound site, causing recoil of the wound area. Factors leak from damaged cells at the wound site, called Damage Associated Molecular Patterns (DAMP), including cytoplasmic metabolites, peptides and proteins such as ATP [81]. These factors contact and bind to receptors on cells immediately adjacent to the new wound gap and stimulate transcriptional cytokine and chemokine cascades, such as interleukin-1. Rapid calcium waves, which are propagated to neighbouring cell rows from the wound edge, are triggered by both biochemical and mechanical signalling [82–84]. Explant wing discs display intercellular calcium waves that increase locally when subjected to mechanical stress [85]. When mechanically injured, repair can progress without calcium waves, but wound healing failure greatly increases.

These initial signals trigger the actomyosin cytoskeleton to assemble a supracellular purse string at the wound edge to rapidly close together [86–88] (Figure 1.5.A). Actin purse strings were first reported in incisional wounds of the embryonic chick wing bud and have since been found across many animal models, including *Xenopus [89]*, *Drosophila [88]*, zebrafish [90,91] and mice [92]. Mechanical signals are critical to cytoskeleton organisation

during wound closure [93]. *Drosophila* embryonic repair has been used to demonstrate that myosin stability is regulated by high mechanical tension at the wound edge [94]. Indeed, reducing purse string tension by laser ablation resulted in increased turnover and loss of myosin [94]. The geometric properties of the wound can influence actin assembly. For instance, wound curvature can influence lamellipodia assembly [95,96].

Many actin-related proteins have explicit roles in purse string or lamellipodia assembly. These regulators ensure that actin assembles in the correct location by remodelling the cell membrane and junctional complexes, for instance, SCAR [97], WASp [97], Dynamin [97] or Septins [98]. Proteins from GTPase families, such as Rho, may be necessary for mediating the cadherin-based intracellular linking of the actin cable through its association with α-catenin and p120catenin [99,100]. Rab5 also has roles in membrane trafficking, which is crucial in assembling actomyosin structures during wound healing [97]. Many regulators ensure that actin assembles into required structures by promoting actin stabilisation or branching during wound healing, for instance, Arp2/3 [65,101], Diaphanous [97], and Zasp52 [102]. Wound repair may also adapt to the disruption of these regulators by assembling alternate actin structures to seal the wound. For example, when branched actin regulated by Arp2/3 is absent in *Drosophila* embryos, cells compensate by forming parallel linear actin filaments that generate a chiral swirling motion to facilitate closure, although the precise molecular mechanism behind these novel structures is currently unknown (Figure 1.5.B) [103].

During the slow phase, cell intercalations are vital for seamless closure, allowing wound edge cells to flow past each other, away from the wound as shown in the *Drosophila* wing disc [104] or by releasing tension in cells away from the wound as shown in the *Drosophila* embryo [105] (Figure 1.5.C). Changing tissue intrinsic properties such as tissue tension, by inhibiting ROCK, can impact speed of closure; for example, softer tissues heal faster than stiffer tissues in the *Drosophila* wing disc [104]. Kinases such as MLCK and ROCK are also essential for the activation of actomyosin contraction and tissue fluidity. Upstream regulators, such as Rho GTPases, are also

essential for the correction formation of actomyosin machinery [24,76,88]. The function of Rho GTPases is dependent on their subcellular localisation [22,23,106,107].

Some tissues increase wound edge cell volume to plug the wound gap via endoreplication, cell fusion or autophagy in combination with the purse string to aid wound closure (Figure 1.5.D) [108–113]. These volume-expansion strategies have been observed in the squamous cells of the adult *Drosophila* abdominal epidermis [108,109,112,113], pupal notum [114] and embryo [110]. In contrast, such mechanisms are not seen after wounding in columnar tissues like the *Drosophila* wing disc. This may be due to differences in cell division speed between cell types, making some more capable of rapid fusion and volume changes than others, for example, cell size or DNA regulation [115,116].

Changes in volume have implications for global and local tissue tension around the wound. Directly, by compressing neighbouring cells or indirectly by triggering myosin II upregulation, which may provide a way to restore lost tension [108]. Cell fusion allows wound edge cells to increase their volume without making new material and may also reduce intercalation, the slowest step of closure. Cell fusion may also reduce local tissue tension by dissipating high tension at tricellular junctions by removing them. Alternatively, cells can quickly pool actin resources to the wound edge [111].

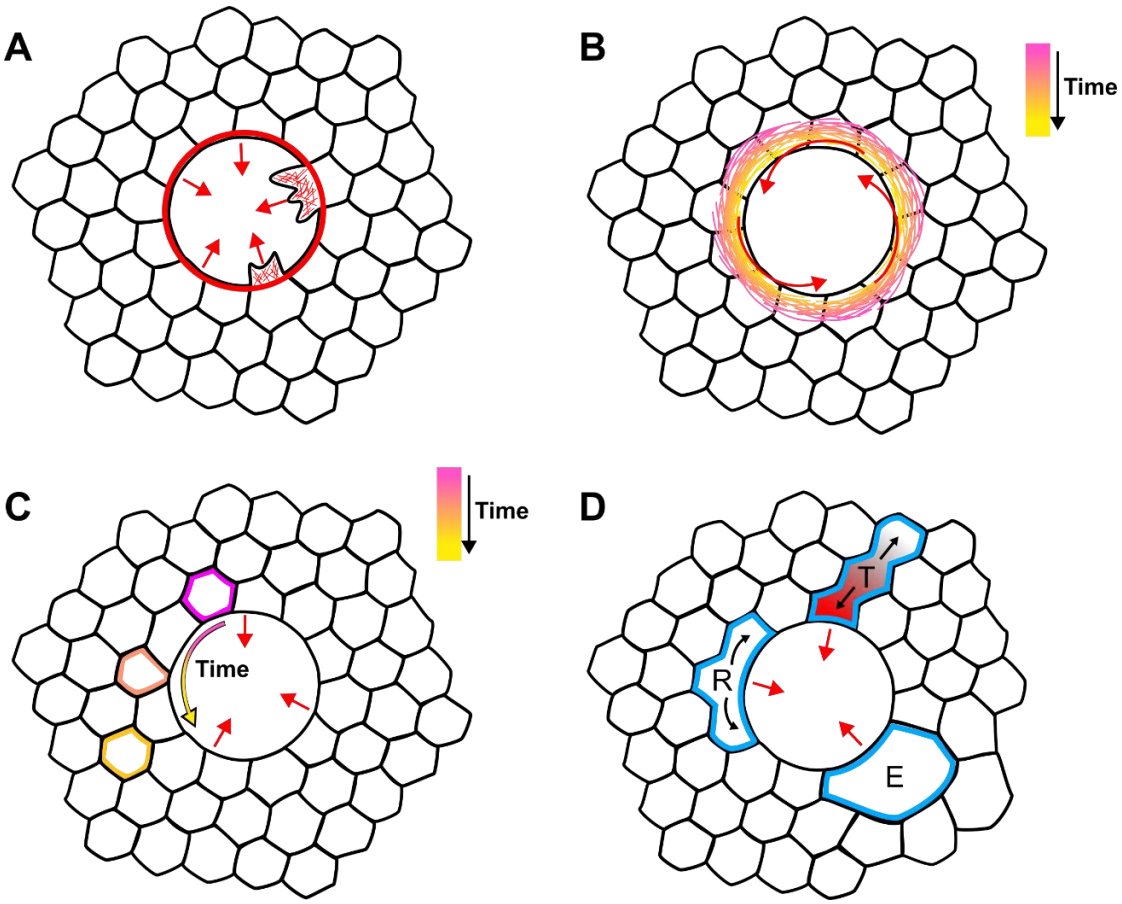

Figure 1.5: Two-dimensional wound healing mechanisms.

A) Purse string and lamellipodia (red). B) Linear actin assembling in a swirling mechanism. C) Wound edge cells intercalating from the wound edge. D) Blue cells undergoing either endoreplication (cell 'E') or fusion (tangentially as 'T' or radially as 'R'). Red gradient in cell 'T' indicates resources moving towards the wound edge cell after tangential fusion. Adapted from [117].

1.2.2 Basolateral dynamics in wound repair

3D cell shape is governed by surface tension, which is in turn controlled by cortical tension, cell–cell contacts, and cell-ECM contacts, which are all altered during tissue repair. MDCK scratch wound studies have observed that actomyosin localises at the lateral membrane at the wound edge during closure (Figure 1.6.A) [118] and that cell height decreases at the wound site (Figure 1.6.B) [95]. Computational wound healing models have also proposed that cells must shorten to preserve their volume [119].

However, most wound healing behaviours have only been extensively described on the apical cell surface as 2D phenomena, whereas cells, particularly in the wing disc, are 3D structures. MDCK cells are, on average, 7 µm in height and 30 µm in diameter [120]. How changes in cell shape are coordinated across the apicobasal axis in the wound healing of non-squamous cells has not been studied before.

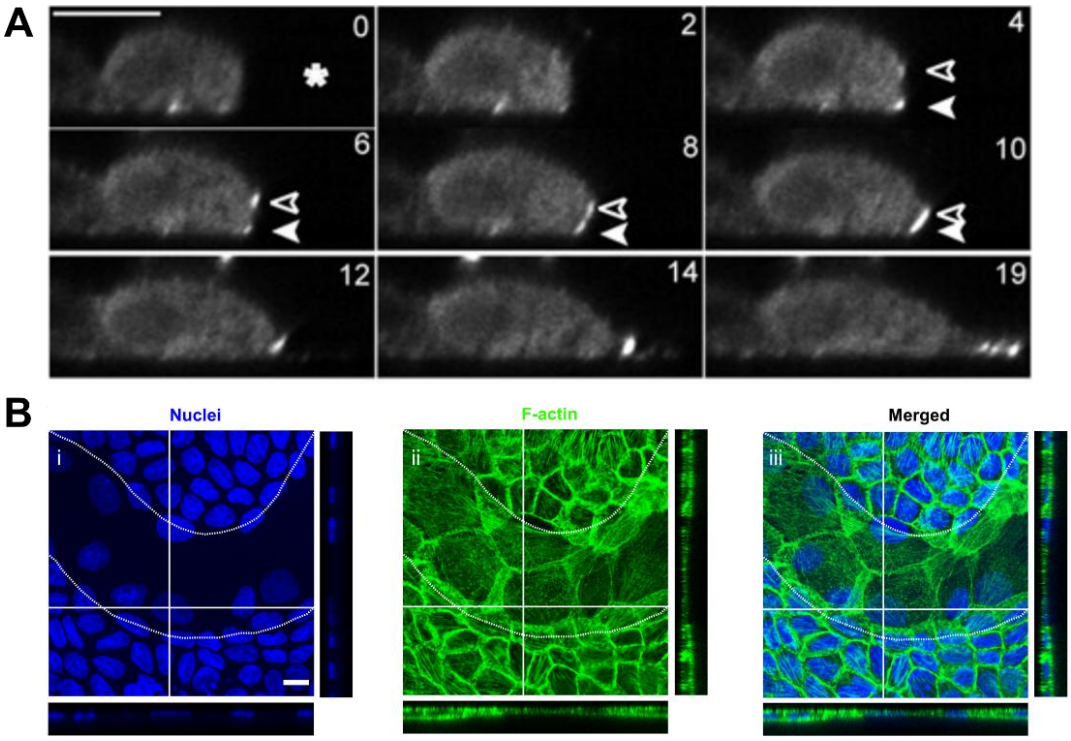

Figure 1.6: Basolateral dynamics in MDCK wound healing.
A) Cross-sectional views of lateral myosin light chain (MLC-EGFP) accumulation in wound edge cells. Adapted from [118]. B) Orthogonal views of scratch wounds. Adapted from [95]. Scale bars are 10 µm.

1.2.3 Parallels to 3D tissue morphogenesis

Although little is known about how 3D tissues behave during wound healing, there are many examples of apicobasal coordinated behaviours in tissue morphogenesis. In *Drosophila* wing disc folding, cell shortening is facilitated by actomyosin accumulation at lateral cell interfaces to generate increased lateral tension [121]. Alternatively, in *Drosophila* leg disc folding, apoptotic cells use apicobasal actomyosin cables attached to their nucleus to generate apical deformation to initiate fold formation [122,123]. These cables were

anchored basally via F-actin to Talin and the linker of nucleoskeleton and cytoskeleton (LINC) complex.

There are many conserved physical mechanisms between wound healing and morphogenesis, for example, in *Drosophila*: purse string contraction and intercalations are crucial to dorsal closure and germband extension, respectively [88,124]. In the latter basal intercalations precede apical intercalations via basal protrusions (Figure 1.7) [124]. In wound healing, wing disc epithelia return to their original arrangement via intercalations on the apical surface after closure, but it is unknown if this also happens on the basal surface.

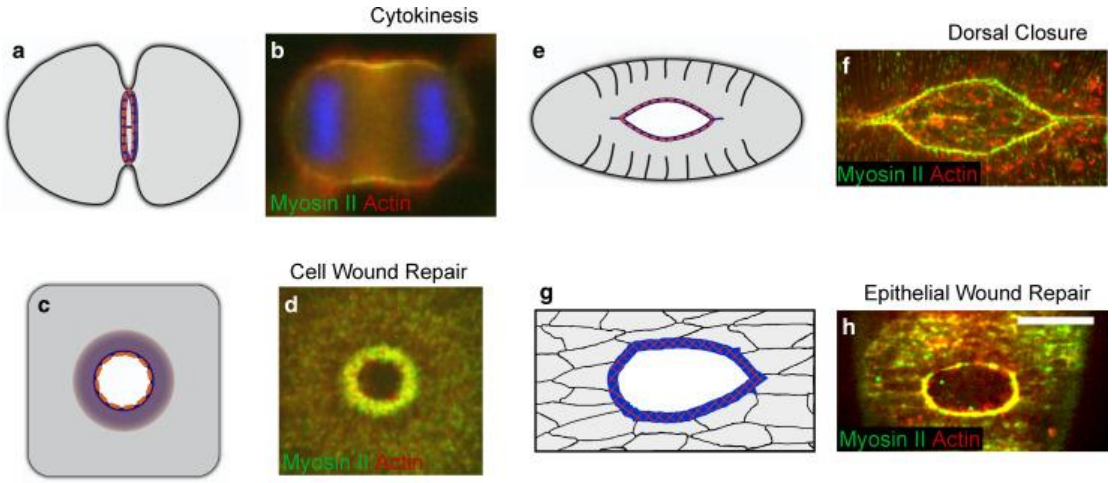

Figure 1.7: Actomyosin purse strings in morphogenesis and repair. Actin (blue) and Myosin (orange). Adapted from [125].

1.3 The BM in wound repair

In *in vitro* scratch wounds, the stiffness and alignment of the BM affect cell migration [126,127]. In mammalian cell scratch wound assays, Ajeti et al. show that the choice of wound healing mechanism depends on substrate stiffness, with lamellipodia-driven closure favoured on stiff substrates while purse-strings were favoured on softer substrates [128]. Cells clearly sense and respond to properties of the underlying substrate. Perhaps there are roles for cell-BM adhesions and the BM itself in modulating 3D cell shape

during wound healing in complex epithelia. Traction force microscopy of MDCK cells revealed that supracellular actomyosin not only contributes to wound closure through a purse string mechanism but also transmits part of its contractile force to focal adhesions to compress the underlying substrate [64]. Cell-BM adhesions are remodelled during wound healing and, when perturbed, can delay repair. In i*n vivo Drosophila* embryos, Talin is polarised at wound edge cells, and Integrin knockdown reduces E-cadherin and the actin purse string [129]. Cell-BM adhesion receptors, such as integrins, attach cells to the BM and form complexes with other molecules that link to the actomyosin cytoskeleton. In wound healing, loss of integrin leads to increased skin blisters along with BM defects in mice [130], whilst activating JNK signalling and multinucleate syncytium formation in *Drosophila* epidermis, which are important behaviours for wound healing [131]. These adhesions facilitate biochemical and mechanical communication between cells and the BM, which regulates cell shape, movement, function, and fate.

The role of the BM during *in vivo* wound repair will also depend on whether the BM is itself damaged or not during wounding. In *Clytia hemisphaerica* wounds, when the BM is damaged, there is a rapid switch from lamellipodia-dependent cell crawling to purse-string-mediated closure [74,132]. However, in some tissues, removal of BM at wounds can accelerate healing, as demonstrated in corneal wounds [72,133].

The BM and integrin-mediated cell-BM adhesion are essential for establishing cell polarity. MDCK systems have been used to show that interaction between BM, integrin and Rac1 orients the apicobasal axis perpendicular to the BM [134,135]. Inhibition of integrin or Rac1, or addition of exogenous BM components, can reverse or restore apicobasal polarity [134,135]. Loss of cell polarity is an early hallmark of cancer, leading to uncontrolled cell division and invasion into surrounding tissues [136]. Similarly, loss of the BM or BM attachment is another characteristic feature of cancer progression, enabling cells to transition into increased proliferative and invasive behaviour [137–140]. The close parallels between wound healing and cancer progression have led to the characterisation of cancer as a “wound that never heals” [141,142]. Physical defects in BM-mimicking

Collagen IV-matrices triggered epithelial-mesenchymal transition (EMT) and invasion in normal epithelial cells [140]. This demonstrates that defects in the BM can trigger pathological cell transformations. Mechanical wounds or aberrant expression of BM-degrading enzymes like MMPs or their regulators, TIMPs, can create physical defects in the basement membrane (BM). These defects can exacerbate existing wounds and contribute to the development of chronic degenerative diseases and vascular complications in diabetes [41]. This aberrant expression is the initial cause of many chronic degenerative diseases and vascular complications in diabetes [41].

1.3.1 The role of BM in tissue morphogenesis

Even though the role of the BM in wound healing is understudied, its significance in maintaining 3D cell and tissue shape during morphogenesis is well-established [126]. Changes in BM composition can change its mechanical properties, such as stiffness and ultimate tensile strength, which are crucial to its compressive roles [126]. For example, elongation in the *Drosophila* egg chamber is driven by the alignment of Laminin fibrils and f-actin to generate a corset that mechanically constrains the egg [143]. Collagenase-induced BM removal results in rounding, emphasising the BM's structural role (Figure 1.8.A). Furthermore, *collagen IV* knockdown or using collagenase and MMP overexpression to remove the BM in the *Drosophila* wing disc induces ectopic folds and cell height reduction and in the *Drosophila* ventral nerve cord, an extended tissue morphology (Figure 1.8.B-C) [144–146]. Generally, BM removal by *collagen IV* knockdown or MMP2 overexpression causes a decrease in cell compression, causing expansion or incorrect tissue folding (Figure 1.8) [144,147,148]. Perturbing integrin can reproduce similar phenotypes; for example, cells lacking the βPS integrin subunit have a reduced height compared to their wildtype neighbours [146]. The correct spatiotemporal expression of MMPs and TIMPs has various roles in human embryonic morphogenesis, including in the kidneys, liver, colon, placenta, intestines, stomach, bladder, pancreas, ovary, uterus, heart, skin, lungs, brain and bone marrow [41]. The BM can also act as a “tissue memory”, for example, following actomyosin-mediated bending of the wing disc pouch, the BM maintains the cell deformation with curvature correlated

with local integrin concentration levels after the actomyosin network is removed [149].

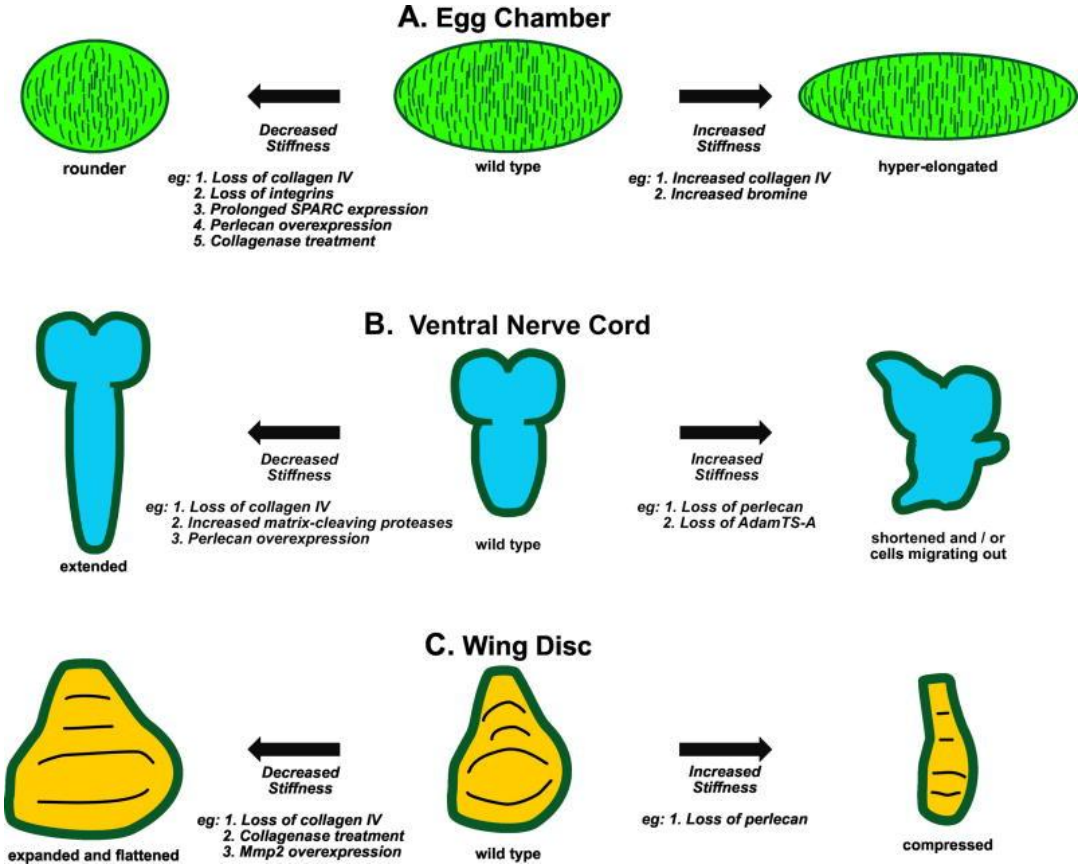

Figure 1.8: Examples of how changes in basement membrane stiffness can alter organ shape in *Drosophila*.

A) Egg chamber. B) Ventral nerve cord. C) Wing disc. Adapted from [147].

Beyond its mechanical functions, the BM plays crucial signalling roles. Unexpectedly, *perlecan* knockdown appears to increase compressive forces, which increases cell height and cell surface area in *Drosophila* wing discs. Conversely, *perlecan* overexpression decreases cell height and wing disc surface area (Figure 1.8.C) [144,145]. Ma et al. found that this was not directly caused by changes in compression but rather a Dpp-signalling deficit. Without Perlecan, the BM cannot act as a barrier required for Dpp signalling [145]. During mouse neural tube closure, there is also an integrin-mediated zippering mechanism driving closure, in addition to the actomyosin purse-string and cell crawling [150].

1.4 Drosophila wing discs as a 3D wound repair model

The *Drosophila* wing disc is a larval epithelial sac that will become the adult wing and notum. It consists of a layer of pseudostratified columnar epithelia connected to a sheet of squamous cells, the peripodial layer, all encased in a thin layer of basement membrane (Figure 1.9). At the third larval instar, wing disc proper cells are up to 50μm tall and 3μm wide scutoids [151,152]. Wing discs are powerful systems for studying epithelial wound repair as they robustly heal, even regenerating whole tissues from severed fragments [153–158]. *Drosophila melanogaster* is highly genetically tractable due to its small genome with well-characterised genetics. Indeed, 65% of human disease-causing genes have a functional homolog in *Drosophila* [159]. Furthermore, many powerful genetic tools have been developed to manipulate various biological processes, for instance, the GAL4/UAS system described in 2.2 [160,161]. They are attractive for studying the physical mechanisms of wound healing as they can be cultured *ex vivo* for up to 8 hours, allowing high-resolution live imaging [162–164].

Large-scale genetic screens and functional imaging in wing discs have identified key conserved wound healing signalling pathways and related genes, including the JNK, Wnt/Wg, JAK/STAT, Hippo and TGFβ pathways [165–170]. Moreover, mechanical forces themselves have been shown to modulate signalling pathways such as JNK activation in mechanically stretched *Drosophila* S2 cells [130].

It is difficult to study the separate effects of intrinsic tissue, such as cell mechanics and extrinsic mechanisms, such as the immune system, during wound healing. Advantageously, wound healing in the *Drosophila* wing disc does not require an immune response [104,171]. Wing discs wound healing involves the rapid formation of a purse string within five minutes of wounding, followed by steady cell intercalation at the wound edge throughout closure [104]. In contrast to the *Drosophila* embryo, which forms a rosette-like scar upon closure, wing discs are capable of sealing wounds seamlessly through intercalations, which is reflected in the lower percentage of cell junctions at

the wound site in wing discs compared to embryos at closure [104]. Additionally, unlike the embryo or the abdominal epidermis [99–104], wing discs do not exhibit cell fusion or endoreplication during wound healing. Cell division is also not required for wing disc wound closure [172].

Additionally, the tall columnar shape of cells in the wing disc proper provides an intriguing model for studying 3D shape change during wound repair. This complex shape allows the study of basolateral dynamics often overlooked in simpler, flatter models, such as MDCK cell scratch assays or epidermal wounds. There is a clear distinction between protein composition and mechanics in apical and basal domains of wing discs, with examples of distinct behaviours during morphogenesis [161,162]. Furthermore, there are many human epithelial tissues, such as the intestinal epithelium, with similar columnar morphologies, making the wing disc a relevant model for studying human tissue repair. In addition, dissected wing discs retain a thin layer of BM, offering a simple model to investigate the roles of the BM during wound healing.

Preliminary imaging performed in the lab has revealed that the apical and basal domains of the wing disc undergo distinct behaviours during wound healing and will be discussed in Chapter 3. Wounds are made in the centre of the pouch region on the apical surface (See Methods Figure 2.3 for more detail). However, visualising the basal surface during this process presents a significant imaging challenge. Due to the tall, columnar architecture of the wing disc proper epithelium, the basal surface lies far from the coverslip when mounted for wounding the apical surface (Figure 1.9). This increased depth leads to light scattering and reduced image resolution, making it difficult to image the basal lateral regions of the cell and BM. These limitations, and how they are addressed, will be further explored in Chapters 2 and 3.

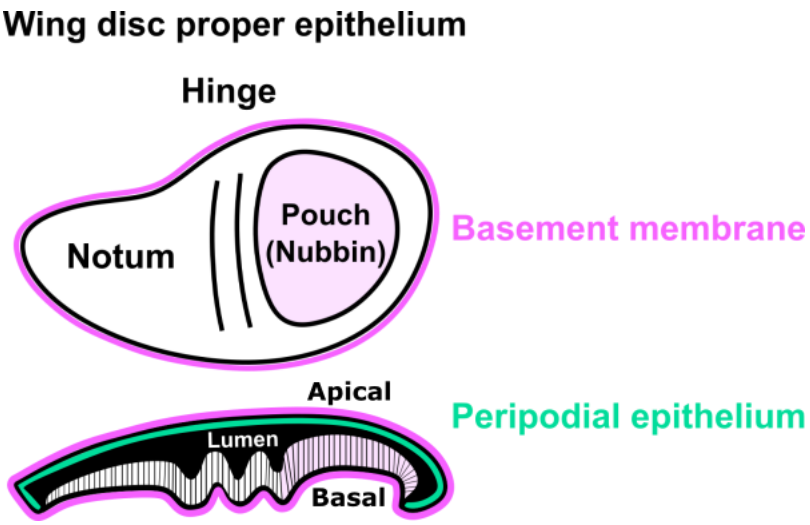

Figure 1.9: Structure of the third instar wing disc.

Top: The cells of the wing disc proper are organised into the notum, hinge and pouch (pastel pink) regions, with the basement membrane encasing the wing disc (magenta). Nubbin is expressed in the pastel pink pouch region. Bottom: A cross section of the wing disc shows that over the wing disc proper lies the peripodial layer of squamous cells (green) with a lumen (black) between the peripodial and wing disc proper layers.

1.5 Project rationale and aims

While the wing disc has been well studied in the context of wound healing and morphogenesis for many decades, very little is known about its lateral and basal behaviours during wound closure despite its extremely 3D properties. Similarly, the BM has clear roles in maintaining cell and tissue in wing disc morphogenesis but not in cell and tissue shape during wound healing [121,145,174]. As morphogenesis and wound closure share many mechanisms to close gaps and change cell shape, there are likely to be basolateral and BM behaviours driving cell shape change in wound healing as there are in morphogenesis [88,105,175]. Furthermore, many organs in the human body take on a similar morphology to *Drosophila* wing disc columnar epithelia. For example, the digestive tract, respiratory system and reproductive organs [3]. Various wound healing-associated diseases in these tissues would benefit from studies focusing on their columnar cell shape properties [176,177].

This thesis aims to use the *Drosophila* wing disc as a model to investigate the role of 3D cell shape changes during wound healing. Furthermore, to determine how these 3D cell shape changes are driven by cell intrinsic and extrinsic factors, such as the actomyosin cytoskeleton and BM, respectively. This thesis hopes to uncover new biochemical and mechanical mechanisms behind 3D cell shape changes during wound healing.

Preliminary experiments performed by Dr Rob Tetley demonstrate these 3D wound healing behaviours and will be discussed in Chapter 3.1. Together with this previous work, this thesis proposes that cell shortening during *Drosophila* wing disc wound healing is driven by lateral actomyosin cables in wound edge cells. Secondly, that cell shape, including shortening, is affected by integrin-mediated attachment to the BM. I will address these hypotheses with the following aims:

1. Characterise the molecular and mechanical differences in wound edge cells upon wounding. (Chapter 3)
2. Quantify the forces acting along the apicobasal axis during wound repair. (Chapter 4)
3. Determine the molecular mechanisms driving lateral cable formation and regulation during wound repair. (Chapter 5)
4. Determine the role of the BM during wound repair. (Chapter 6)

2 Materials & Methods

2.1 Fly stocks

Drosophila stocks were raised on conventional cornmeal media at 25°C or 18°C for *shibire^{TS}* stocks. Crosses were performed at 25°C or 18°C for *shibire^{TS}* crosses. Virgins carrying the *nubGAL4* driver were crossed with males carrying the relevant UAS line constructs in a ratio of at least 5 females to 1 male. To ensure accurate staging for early-mid third instar larvae, experimental fly stocks and crosses were flipped into new tubes 4 days before dissection and flipped daily. A small wad of tissue was added to prevent fungal growth in low-density population tubes. Alleles and transgenes used to generate stocks and experimental crosses are shown in Table 2.1.

Genotype	Source
sqh^{AX3};sqhGFP;	BL 57144; Gift from F. Pichaud
;nubGAL4	BL 86108
;UAS-LifeActRuby	BL 35545
;sqhGFP,nubGAL4;	Recombined by Dr R. Barrientos
;GFP-CAAX,cgGAL4;vkgSca	Recombined by Dr R. Barrientos
;;rheaF40TS	Gift from F. Schnorrer
;;rheaHPTS	Gift from F. Schnorrer
;;rheaHPTSCterm	Gift from F. Schnorrer
;;rheaYPetCterm	Gift from F. Schnorrer
;;rheamCherryCterm	Gift from F. Schnorrer
;;rheaYPetInternal	Gift from F. Schnorrer
;;rheamCherryInternal	Gift from F. Schnorrer
yw;;	
shibire^{TS}	Gift from N. Tapon
UAS-rheaRNAi	BDSC 33913
UAS-rheaRNAi	VDRC 40399
UAS-rokRNAi	VDRC 104675
UAS-mbsRNAi	VDRC 105762

UAS-mysDN	Martin-Bermudo & Brown (1999) [178]
w;If/CyO;CdepGFP/TM6B	Gift from Y. Bellaiche
UAS-CdepRNAi	VDRC 104438
sqhAX3;sqhGFP,nubGAL4;	Recombined for this thesis

Table 2.1: *Drosophila* genotypes for stocks and experimental crosses.

2.1.1 DNA sequencing shibire alleles

There are four alleles: shi^1, shi^2, shi^4 and shiST139 which display similarly impaired endocytosis phenotypes however, shi^2 has a higher viability [179,180]. Shi^2 is a point mutation at location X:15,895,035, where nucleotide base G is replaced with A, replacing amino acid glycine with serine. To confirm that shi^2 was the allele present in the shi^{TS} stocks used in Chapter 5.2, I performed polymerase chain reaction (PCR) followed by DNA sequencing as summarised below.

DNA was extracted from shi^{TS} flies and compared against DNA extracted from yw flies. 50 adult flies from each stock were thoroughly ground in a 1.5 ml micropipette with a disposable micropestle. DNA was extracted using a DNeasy Blood and Tissue Extraction kit (Qiagen) according to the manufacturer's instructions. The purity and quantity of DNA were assessed using a NanoDrop (ThermoFisher Scientific). I designed primers flanking the shi^2 gene location (Table 2.2). These primers were used with a Phusion High Fidelity PCR kit (New England Biolabs), resulting in amplified 1.2kb DNA segments. The amplified segments were extracted using a QIAquick Gel Extraction kit (Qiagen) and sent to the Medical Research Council Protein Phosphorylation and Ubiquitylation Unit (University of Dundee) for DNA Sequencing, where subsequent genotyping was performed by allele-specific PCR. The genotyping confirmed that the amplified segments contained the shi^2 allele.

Target	Forward primer	Reverse primer
shi^2	AACGTTTTCCCCATTTTACAGA	TCAAGAGCTACAAACGGAAATC

Table 2.2: Primers designed to identify the shi^2 allele.

2.2 GAL4/UAS system

The GAL4/UAS system is a transcription activation system originally from yeast [160,161] that has been adapted to several organisms, including *Drosophila* [181]. GAL4 is a transcriptional factor that is driven under a tissue-specific promoter. When GAL4 binds to the Upstream Activation Sequence (UAS), gene expression is activated. This system allows spatial control of subsequent gene expression in specific patterns and at much higher levels than endogenous tissue-specific promoters. I used the GAL4/UAS system to drive the expression of various fluorescent proteins, RNAis, and dominant negative proteins in the pouch region of the wing disc using *nubGAL4*. I also used *cgGAL4* to drive the expression of fluorescently labelled Collagen IV, specifically *UAS-vkg-mScarlet*, by the fat body tissue.

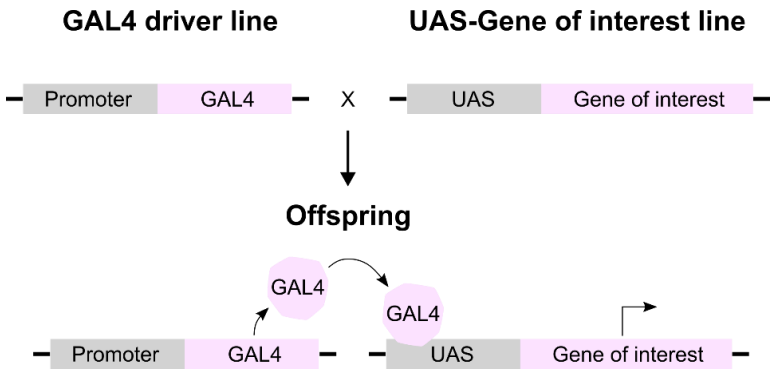

Figure 2.1: GAL4/UAS system.

The GAL4 driver fly line is crossed to a UAS fly line. In the offspring, the GAL4 drives the expression of the UAS and induces strong activation of the gene of interest.

2.3 *Ex vivo* wing disc culture

Prior to wing disc dissection, forceps and glassware were washed with 70% ethanol and phosphate-buffered saline (PBS). Wing discs are dissected and cultured in dissecting media, which consists of Shields and Sang M3 media (Sigma-Aldrich) supplemented with 2% fetal bovine serum (FBS, Sigma-Aldrich), 1% penicillin-streptomycin (pen/strep, ThermoFisher Scientific), 3 ng/mL ecdysone (Sigma-Aldrich) and 2 ng/ml insulin (Sigma-Aldrich). For long-term storage, dissecting media is made in 50 mL base aliquots of Shield

and Sangs M3 Insect medium, 2% FBS, and 1% pen/strep under a tissue culture hood, which are further divided into ten 5 mL aliquots and stored at 4°C. Before use, I add 0.3 µl of 0.05 mg/mL ecdysone stock and 1µL of 0.01 mg/mL insulin stock to a 5 mL base aliquot and gently shake to mix the hormones at RT. Each aliquot is used for no more than 3 days, as the media is highly susceptible to fungal growth once hormones are added.

I dissected wing discs using the protocol described by Klein et al [182]. Third instar (72-150 hrs AEL) larvae are washed in a glass dish containing 500 µl dissecting media. For dissection, individual larvae are transferred to a concave glass well on a Leica MZ125 stereomicroscope equipped with an external LED lamp. To remove the wing discs, I pinched the larvae with one pair of forceps and inserted another pair into the mouth of the larvae to pull the head from the body. The wing discs are found attached to the head by trachea tubes, which I detach using the forceps. Once the discs are removed, I transfer them with a P20 pipette to a glass well in a 9-well glass plate with 100µl of dissecting media. CellMask Deep Red (ThermoFisher Scientific) may be used to stain cell membranes. Dissected wing discs were incubated in 1:1000 CellMask diluted in dissecting media for 30 min before being washed and mounted as described in the next subsection (Chapter 2.3.1).

2.3.1 Mounting of live wing discs

Early third instar (72-96 AEL) wing discs are selected for live imaging, as younger wing discs are flatter. As the wing disc develops, the cells of the disc proper grow in size, and the pouch region adopts a domed morphology. Wing discs were mounted by two different methods, depending on the desired side of imaging and duration of acquisition and are described as follows.

The first method is termed the fluorodish method (Figure 2.2.A). Firstly, 1ul line of Cell-Tak (Corning) is dried onto a Fluoro glass-bottomed dish (World Precision Instruments) on a heat plate set to 29°C. Cell-Tak is a cellular adhesive that is used to prevent the wing discs from moving during imaging and adhere the discs to the surface of the glass. Dissected wing discs are transferred in 10 µl of dissecting media with a P20 pipette to the glass-

bottom dish, ensuring wings fall adjacent to the Cell-Tak line. Using forceps, wings are quickly re-positioned apical side down onto the Cell-Tak, which adheres to the Cell-Tak immediately. I added a further 1 mL of dissecting media before sealing the dish with parafilm. Dextran Alex Fluor 647 may be added to the dissecting media in the fluorodish at a 1:100 dilution.

The second method is termed the coverslip sandwich and was developed by Dr Rob Tetley and the Dahmann lab [121] (Figure 2.2.B). It consists of a channel formed by two strips of double-sided tape with 0.1 mm thickness (Tesa 05338) sandwiched between two coverslips [121]. Discs are transferred to the centre of the channel in 10ul of dissecting media with a P20 pipette. Using forceps, the discs are repositioned to all face the same orientation. A second coverslip is placed on top, and the channel is filled via capillary action with 20 µl of dissecting media. Through this method, discs were wounded on the apical surface as described, then flipped over and replaced so that the basal surface faced the objective. To attempt to further compress the discs, I tried using a thinner 0.05 mm width tape, 467 MP Adhesive Tape (3M™ VHB™); however, the discs were excessively compressed and suffered from glue toxicity.

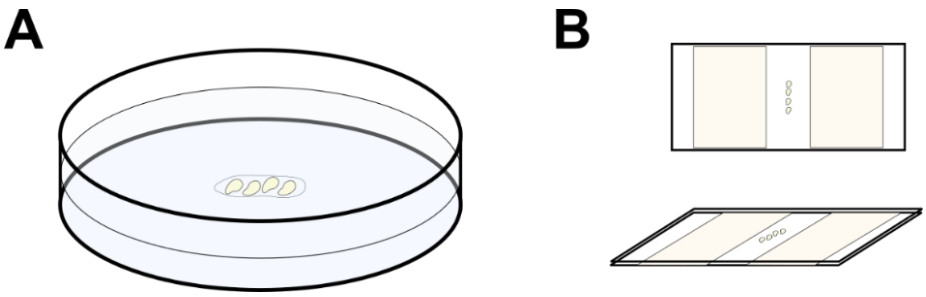

Figure 2.2: Wing disc mounting methods.
A) Fluorodish method. B) Coverslip sandwich method.

2.3.2 Temperature shift

For temperature shift experiments involving shi^{TS} flies and controls, dissected and mounted wing discs were incubated on a pre-heated microscope stage at 31°C for at least 1 hr before imaging to ensure maximum gene expression. Subsequent wounding and imaging are also performed at 31°C. Imaging discs mounted in the coverslip sandwich is not suitable, as there is only 20 µl

of media in the channel, which would evaporate quickly under the increased temperature.

2.4 Immunofluorescence and dyes

After dissection, wing discs were fixed at room temperature (RT) for 30 min in 4% paraformaldehyde (PFA) in PBS or for 18 min in 18% PFA in PBS. Fixed wing discs were washed 4 times for 10 min each in phosphate-buffered solution with 0.3% Triton X-100 (PBT), then 4 times for 10 min each in PBT with 0.5% bovine serum albumin (PBT-BSA). Then, primary antibody staining was performed at appropriate concentrations diluted in PBT-BSA (Table 2.3) overnight at 4°C. Wing discs were washed again with PBT and PBT-BSA as described in the previous step. Then, secondary antibody staining and addition of dyes (Table 2.4) were performed for 1-2 hrs at RT. These primary antibodies were combined with mouse, rabbit, or goat secondary antibodies conjugated to atto647, Rhodamine Red-X, and FITC, respectively, at a 1:200 dilution in PBT-BSA. Discs were washed 3 times for 20 min each with PBT and finally rinsed 3 times with PBS. Discs were mounted in Fluoromount G slide mounting medium (Southern Biotech) on a glass microscope slide (VWR 631-0905) for imaging.

Antigen	Antibody #	Species	Origin	Concentration
GFP*	AB6662	Goat	Abcam	1:200
LanB1	AB_2133633	Rabbit	Invitrogen	1:500
Mys	CF.6G11	Mouse	DSHB	1:100

Table 2.3: Primary antibodies.

Developmental Studies Hybridoma Bank (DSHB). *Performed during secondary antibody staining.

Dye	Stock	Dilution	Cat. No.
Hoechst	50 mg/ml	1:25000	Sigma B2261
Alexa Fluor 647 Phalloidin	200 units/ml	1:20	Life Technologies A22287
CellMask Deep Red	5 mg/ml	1:500	ThermoFisher Scientific C10046

Dextran Alexa Fluor 647 10,000 MW	1mg/ml	1:100	ThermoFisher Scientific D22914

Table 2.4: Dyes.

2.5 Expansion microscopy

For optimising fixation, third instar wing discs were fixed at RT with either 4% PFA for 30min, 18% PFA for 10min, or 36% PFA for 4min, all diluted in PBS. Discs were then washed 3 times for 10 min each with PBT. Discs were stained with anti-GFP-FITC and Alexa Fluor 647 Phalloidin for 1 hr at RT with gentle rocking, then washed 3 times with PBS before being mounted in Fluoromount G slide mounting medium (Southern Biotech) on a glass microscope slide (VWR 631-0905) for imaging.

For protein retention expansion microscopy (Pro-ExM) experiments, third instar wing discs were fixed with 18% PFA in PBS for 10 min at RT. They were then washed 3 times for 10 min each in PBT and rinsed 4 times with PBS, followed by primary and secondary antibody staining as described in Chapter 2.4. All steps were carried out with gentle rocking. Next, wing discs were incubated in 1% Acryloyl-X in PBS overnight at RT in a humid box to attach anchors to the tissue. The next day, wing discs were washed 3 times in PBS and transferred to a coverslip, ensuring the basal side of the wing disc faced the coverslip. For the gelation step, wing discs were immersed in a droplet of activated monomer solution (SA; AA; bis-AA; TEMED; APS) and covered with a 13 mm coverslip on ice for 10 min, then for 1 hr at 37°C in a humid box. Afterwards, the circular coverslip with the attached gel was carefully removed using forceps and incubated with gentle agitation in a wash glass with digestion buffer for 15 min at RT to separate the gel from the coverslip. For the digestion step, the gel was transferred to a 2 ml Eppendorf with varying concentrations of Proteinase K (Pro-K) and 1 ml digestion buffer overnight with gentle rocking, see Chapter 3.5 for further details. The next day, gels were washed in PBS and then incubated with 0.01% Hoechst diluted in PBS for 30 min. Finally, gels are expanded in ddH2O overnight and washed 3 times for 3 min each with ddH2O. Excess gel around the wing

discs was trimmed with a scalpel. Individual gels were placed on a rectangular coverslip and imaged on an inverted Zeiss LSM 900 microscope. To calculate the gel expansion factor, the diameter of the post-expansion gel was measured using a ruler and divided by the pre-expansion gel diameter, which was the diameter of the circular coverslip.

2.6 Confocal imaging

Fixed wing discs were imaged on an inverted Zeiss LSM 980 microscope with a x63 oil objective (NA 1.4). Live wing discs were imaged on an inverted Zeiss LSM 880 microscope with a x63 oil objective (NA 1.4). Images were taken at 512 x 512-pixel resolution under x4 or x5 zoom and 0.3 or 0.5 µm Z step interval. The LSM880 Airyscan detector was used in confocal mode for sensitive imaging. For high-resolution snapshots of the lateral cables, the detector was used in SR mode with suggested optimal parameters, usually 632 x 632-pixel resolution and 0.17 µm Z step interval for x4 zoom. The laser settings are summarised in Table 5. Imaging parameters for FRET-based TS wing discs are further detailed in Chapter 4.

Fluorophore	Laser line	Power (%)
GFP	488nm Argon	0.1-0.5
FITC	488nm Argon	0.2
mCherry	561nm DPSS	0.2-0.8
mScarlet	561nm DPSS	0.1
Rhodamine Red X	561nm DPSS	0.2
Atto647	633nm HeNe	0.2
Alexa Fluor 647	633nm HeNe	0.2
Hoechst	405nm diode	0.2
CellMask Deep Red	633nm HeNe	0.1-0.2

Table 2.5: Fluorophores and respective laser settings used for imaging.

The wing disc is sensitive to light exposure, so laser power must be balanced between cell survival and imaging resolution [183], especially when the tissue is already under stress in wounded conditions. I have found that this is highly dependent on the fly stocks used, with some more amenable to Airyscan imaging than others. For example, I was unable to image lines with

sqhAX3; sqhGFP, nubGAL4; genotype with live Airyscan imaging, but was able to image *;cgGAL4, GFP-CAAX; UAS-vkg-mScarlet* genotype flies. Different genotypes may respond differently to imaging due to variations in fluorescent protein expression. Additionally, genetic background can influence cell physiology and stress responses, meaning some stocks are inherently more robust than others.

In Chapter 3.3, after ablation on the Zeiss LSM 880 (as described in 2.7.1), wing discs were imaged on a Leica STELLARIS DIVE equipped with a x63 oil objective (NA 1.4) with x5 zoom, 512 x 512-pixel resolution, and 0.3 µm Z step interval. Imaging is deliberately oversaturated apically to image the full apicobasal length of the cables.

2.7 Multiphoton laser ablation

Laser ablation can be used to create uniform, reproducible wounds in tissues. It has previously been shown that laser ablation produces tissue damage in a reproducibly graded pattern where damage is most severe at the focal point of the laser and decreases in severity with distance from this focal point [79]. Wing discs were ablated on the Zeiss LSM 880 confocal microscope equipped pulsed Chameleon Vision II Titanium Sapphire (TiSa) laser (Coherent), following the protocol established by Dr Rob Tetley [104].

2.7.1 Cell ablation

Wing disc epithelia were wounded using a pulsed Chameleon Vision II TiSa laser (Coherent) tuned to 760nm with 45-50% laser power. As cell size and packing can vary between different mutants, the ablation regions of interest (ROIs) were manually drawn using circles spanning the entire tricellular junction between cells, typically 1-2 µm in diameter. For each wound, 14 circular ROIs were drawn, consistently resulting in the death of 10–15 cells. For wounds without a clear apical marker, the same ROI template with 14 circular ROIs was used for each wound.

The ROIs were positioned at tricellular junctions in a single z-plane at the level of AJs. Most imaging was performed using fluorescently tagged myosin as a marker. AJs were located 0.3-0.5 µm below the strongest myosin signal.

For wing discs with cell membranes stained with CellMask or marked by GFP-CAAX, the z-plane 2-3µm below the strongest apical signal was chosen as described in Chapter 5.5. For FRET experiments where Talin was the only marker, wounds were made at the z-plane 5 µm below the Talin signal of the peripodial cells. This standard distance was found to be successful by previous experiments by Dr Rob Tetley.

2.7.2 BM ablation

BM ablations were performed on the same microscope as described in 2.7.1 using a pulsed Chameleon Vision II TiSa laser (Coherent) tuned to 760nm with 70-80% laser power and a single large circular ROI with approximately 15 µm diameter. The ROI was placed in the z-plane with the most BM marker signal. When the tissue is particularly curved, the area is ablated again at the z plane with any remaining fluorescent signal to ensure all BM fibres are destroyed.

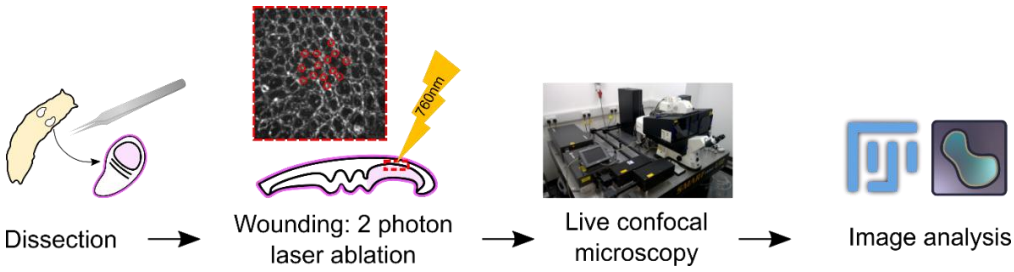

Figure 2.3: Wing disc ablation workflow.
Wing discs were first dissected and mounted. Then, the apical surface was wounded with a 2P laser, and subsequent wound healing was imaged using confocal microscopy. Images were quantified in Fiji/ImageJ [184] and napari [185].

2.8 Image processing and analysis

Image reconstruction and analysis were performed using Fiji/ImageJ [184]. 3D reconstructions were performed in napari [185]. Graphs were produced in GraphPad Prism 10. Figures were mounted in Inkscape 1.1. The following pre-processing steps were performed on all image stacks: rolling ball background subtraction with a radius of 12 px for images collected with 5X

zoom or a radius of 10 px for images collected with x4 zoom settings. Then, a 3D gaussian blur with a radius of 1.0 followed by the 3D Correct Drift ImageJ plugin is applied.

2.8.1 Clone cell height and volume

A custom ImageJ and python-based pipeline developed by Martin Zhang was used to segment and quantify wound edge clones. These wound-edge clones were filled with a cytoplasmic mCherry marker, but there were large holes in the signal due to the presence of untagged nuclei. These holes needed to be accurately filled to quantify the clone volume. This pipeline involved converting the mCherry intensity into a binary mask via Li thresholding, then performing repeated dilation and erosion operations to completely enclose any holes and applying the Fill Holes ImageJ plugin. Next, cell masks were manually corrected in napari to fill any holes that were missed by the plugin and remove any mask regions outside of the clone. Finally, the volume and height of the segmented cells were extracted. To visualise segmented volumes, a median filter was applied to the binary masks to smooth their edges.

2.8.2 Fluorescence intensity on the basal surface

For each wing disc, I generated a maximum intensity projection of 100 z-slices to capture the Talin signal on the basal cell surface. Activated Talin must be localised to the plasma membrane, therefore, maximum intensity projections are appropriate to capture Talin fluorescence, as Talin is not distributed throughout the cytoplasm and they are confined to the plane of the membrane. On the plasma membrane, Talin typically localises to focal adhesion–like structures, appearing as circular, patchy puncta in the basal medial regions of cells. While it is not known how many cells contribute to each punctum, their regular 3 μm spacing suggests they are organised one per cell.

To quantify Talin fluorescence intensity relative to the wound, I adapted a custom ImageJ script (originally developed by Dr. Rob Tetley) to create band-shaped masks. These masks were generated by manually outlining the

wound edge, then expanding this outline by 1 μm into surrounding cells to form consistent 1 μm-thick bands around the wound perimeter. This thickness was chosen to satisfy the Nyquist sampling criterion, given that wing disc cells are approximately 3 μm in diameter, 1 μm-thick bands ensure sufficient resolution to detect cell-scale changes in fluorescence while avoiding undersampling or averaging across multiple cells. Using band masks provides an unbiased, reproducible method to measure fluorescence at consistent distances from the wound, accurately following the wound contour.

2.8.3 Wound area

The wound edge was manually outlined with the ImageJ Polygon tool, and its area was measured using Analyze/Measure in ImageJ. The area was normalised to the area of ablated cells before wounding, which was denoted as the 0 min timepoint. The wound area over time for each wound was fitted with a one-phase decay (Equation 1) in GraphPad Prism 10 from the timepoint after recoil (3 min or 5 min). The following equation was used:

$$y = Plateau + (y_0 - Plateau)e^{-kx} \quad (1)$$

Where x is time, y is the wound area starting from $y_{0,}$ and k is the rate constant. The Plateau is constrained to be equal to 0, and k must be greater than 0.

2.8.4 Myosin intensity quantifications

I measure myosin intensity as a marker of contractility, as it is a motor protein that drives actomyosin contraction [15,17,94,186,187]. I manually select structures of interest, specifically the purse string and lateral cables, through visual inspection as the brightest structures in each image. Timelapse 3D wound healing image stacks present two major challenges in analysis. Firstly, 3D segmentation of these filamentous structures is time-consuming and cannot be automated (see further discussion in Chapters 3 and 5). Secondly, standardising normalisation methods to account for both light attenuation with z-axis depth and photobleaching with time. Furthermore, wounds also vary in size, change size as they heal, and indent at different

orientations. Additionally, wing discs will have intrinsic differences, such as protein expression and external differences, such as mounting position and laser power.

To allow comparison of wounds from different wing discs, intensity measurements are normalised to the apical myosin intensity of the disc before wounding. The z-slices containing the apical myosin cortex are maximum projected, and the borders of future ablated cells are manually outlined using the ImageJ Polygon tool with line width set to 5 px for x5 zoom images or 4 px for x4 zoom images. The mean intensity was measured using Analyze/Measure. The intensity measurement at each timepoint is divided by this value so that they are relative to the resting apical myosin intensity.

To correct for photobleaching, these relative mean intensities were multiplied by a bleach correction factor. This correction factor was derived from mean apical myosin intensity values of unwounded cells at each timepoint. Mean apical myosin intensity is the mean myosin intensity from a maximum projection of the z slices containing apical myosin signal in a 100 px x 100 px ROI positioned in a region at least 1 cell row away from the wound edge cells. I chose apical myosin intensity as a photobleaching reference because the apical myosin cortex in unwounded cells should remain consistent if there is no bleaching. The correction factor is calculated for each timepoint by dividing the mean apical myosin intensity of the respective timepoint by the mean apical myosin intensity at timepoint, 0 min.

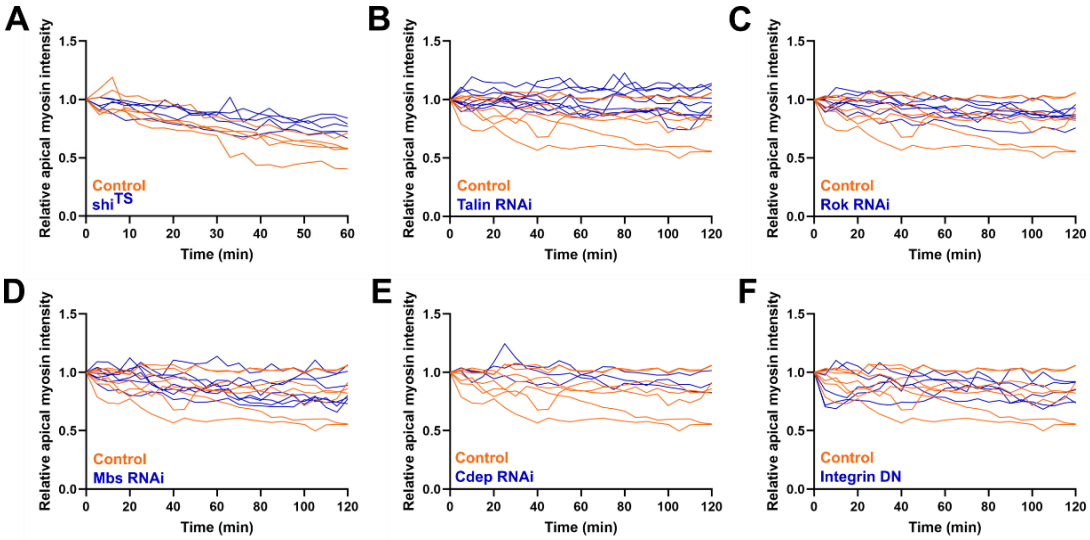

Figure 2.4: Bleach correction factor curves.

A) Bleach correction factor vs time for temperature-shifted control (orange, n=5) and shi^{TS} (blue, n=5) wounds. B) Bleach correction factor vs time for control (orange, n=7) and Talin RNAi (blue, n=9) wounds. C) Bleach correction factor vs time for control (orange, n=7) and Rok RNAi (blue, n=7) wounds. D) Bleach correction factor vs time for control (orange, n=7) and Mbs RNAi (blue, n=7) wounds. E) Bleach correction factor vs time for control (orange, n=7) and Cdep RNAi (blue, n=3) wounds. F) Bleach correction factor vs time for control (orange, n=7) and Integrin DN (blue, n=5) wounds.

To further standardise the analysis, maximum intensity projections of wound structures were used throughout this thesis. Maximum projections are appropriate for structures such as the apical purse string, as the purse string forms the brightest pixels, typically confined within 3-4 z-slices of the wound edge. Maximum projections help to standardise this analysis, as the plane of the purse string may tilt due to the 3D nature of wing disc wound healing, resulting in the purse string spanning different z-slices. Consistently, many other published wound healing studies analysing purse string dynamics have also relied on maximum projections to quantify fluorescence intensity [97,104,129].

Similarly, maximum intensity projections were used to quantify myosin intensity in lateral cables from wound cross sections (XZ slices). As healing progresses and the tissue deforms in 3D and the lateral edges of cells tilt and twist, causing the cables to span multiple XZ slices. Given the complexity of accurately segmenting and thresholding cables in 3D, which will be discussed in detail in Chapter 3, maximum intensity projections allow intensity measurements of the lateral cables to be standardised in a similar manner as the purse string.

However, there are limitations to using maximum intensity projections. By flattening 3D structures into 2D, volumetric information is lost, which can cause underestimation of signal intensity in thicker cables, as differences in thickness are not accounted for. Additionally, maximum intensity projections can overemphasise bright artefacts, but this is mitigated by manually

selecting Z-slices that correspond specifically to the cables of interest, helping to exclude signals from unrelated structures. Overall, this approach gives us an indication of the relative maximum myosin enrichment in the apical purse string and lateral cables over time.

To quantify apical purse string myosin intensity, the z-slices containing the purse string, typically 3-4, were maximum projected for each timepoint. Then, the purse string was manually outlined with the ImageJ Polygon tool. The mean intensity was measured using Analyze/Measure. The mean PS intensity over time for each wound was fitted with either a one-phase association (Equation 2) or a straight-line (Equation 3) from the timepoint after the PS intensity peaks in GraphPad Prism 10.

$$y = y_0 + (Plateau - y_0)(-e^{-kx}) + 1) \quad (2)$$

Where x is time, y is mean myosin intensity starting from $y_{0,}$ and k is the rate constant.

$$y = y_0 + kx \quad (3)$$

Where x is time, y is mean myosin intensity starting from $y_{0,}$ and k is the gradient of the slope.

To quantify lateral myosin intensity, image stacks were resliced to produce XZ stacks. These XZ stacks were manually inspected for cables, and the corresponding XZ slices for each cable were max-projected. On the max projection, a 10 μm line was drawn over the cable starting from beneath the apical surface signal using the line tool set with width set to 5 px for x5 zoom images or 4px for x4 zoom images. A 5 μm line was drawn for temperature-shifted experiments, as the myosin-GFP signal in these discs was weaker and was more quickly attenuated in the z-axis. The mean intensity was measured using Analyze/Measure. This measurement also provides the number of lateral cables at each timepoint. As these measurements require time-consuming manual identification of individual lateral cables for each wound, I focused on 10 min and 60 min post-wounding. At 10 min, we observe from previous quantification (Chapter 3.1) that lateral cables have already formed, and apical indentation has started. At 60 min, there is

notable apical indentation, approximately 4 μm, and basal indentation begins (data not shown).

2.8.5 Apical indentation

Image stacks were resliced to produce XZ stacks. The orthogonal view is used to locate the centre of the wound. Using the ImageJ Line tool, a line was drawn across the apical surface, and the centroid position was measured. Another line was drawn across the purse string, and the centroid position was measured. The apical indentation is defined as the difference in apical and purse string y centroid positions. The apical indentation over time for each wound was fitted with a straight line (Equation 3, where y is apical indentation) in GraphPad Prism 10.

2.8.6 Apical junctions remaining

The initial number of wound edge cells was manually counted at the timepoint immediately after wounding. This step was repeated for every subsequent timepoint. This represents the number of apical junctions present at the wound edge. The percentage of apical junctions was calculated by dividing the number of wound edge cells at each timepoint by the initial number of wound edge cells. The percentage of apical junctions over time for each wound was fitted with a straight line (Equation 3, where y is the percentage of apical junctions) in GraphPad Prism 10.

2.8.7 Basal curvature

Image stacks were resliced to produce XZ stacks, and then slices containing the wound were max projected. The number of slices varied between timepoints depending on how quickly the wound closed. The ImageJ Kappa plugin was used to measure the average curvature and curvature variance of the lateral to basal surfaces of the tissue [188]. Starting from the edge of the purse string, 5 nodes were manually specified along the lateral to basal surface of the wound edge. Kappa fits a B-spline to the joining lines created by the nodes. This was repeated for the left and right sides of the wound.

2.8.8 Cellpose segmentation

Preliminary cell segmentation was performed using Cellpose 1.0 on the online graphical user interface available at https://www.cellpose.org/ [189]. The cytoplasm model was used to segment the green channel, GFP-CAAX, with an average cell diameter of 40.

2.9 Statistical analysis

Statistical tests were performed in GraphPad Prism 10. Specific tests and p-values are reported in the corresponding figures.

3 Characterising 3D cell dynamics during wound healing

3.1 Introduction

The *Drosophila* wing disc is a highly 3D tissue with cells up to 50 μm in height and 3 μm in diameter. When the wing disc is wounded, the wound leaves a 40-50 μm tall gap in the tissue (Figure 3.1.A). Following the initial recoil of the wound edge cells, a supracellular actomyosin purse string is assembled at the wound edge. The purse string contracts, rapidly decreasing the area of the wound gap by up to 50%. In the latter stages of healing, the wound edge cells intercalate away from the edge to prevent cell jamming and return elongated cells to their original shape [104]. In the wing disc, the purse string forms on the apical surface and there are numerous apical markers such as E-cad, myosin and actin to track cell intercalations. On the other hand, the basolateral behaviour of cells during wound healing is relatively understudied, with most findings confined to flatter cells [117].

Dr Rob Tetley, a previous postdoctoral researcher in the Mao lab, discovered that within minutes of wounding, the apical surface indents towards the wound gap and indentation increases as healing progresses (Figure 3.1.B). The basement membrane also indents into the wound gap, but only an hour after wounding (data not shown). Preliminary imaging shows that within 3 minutes of wounding, myosin had accumulated along the apicobasal axis of the wound edge (Figure 3.1.C-E). These myosin accumulations were termed “lateral cables”. Laser ablation of these cables resulted in a strong recoil of the apical purse string and reduction in the apical wound area (Figure 3.1.F-G). This suggested that these cables are under tension and help to maintain a purse string shape. There is also a strong positive correlation between basal myosin localisation and basement membrane deformation (data not shown).

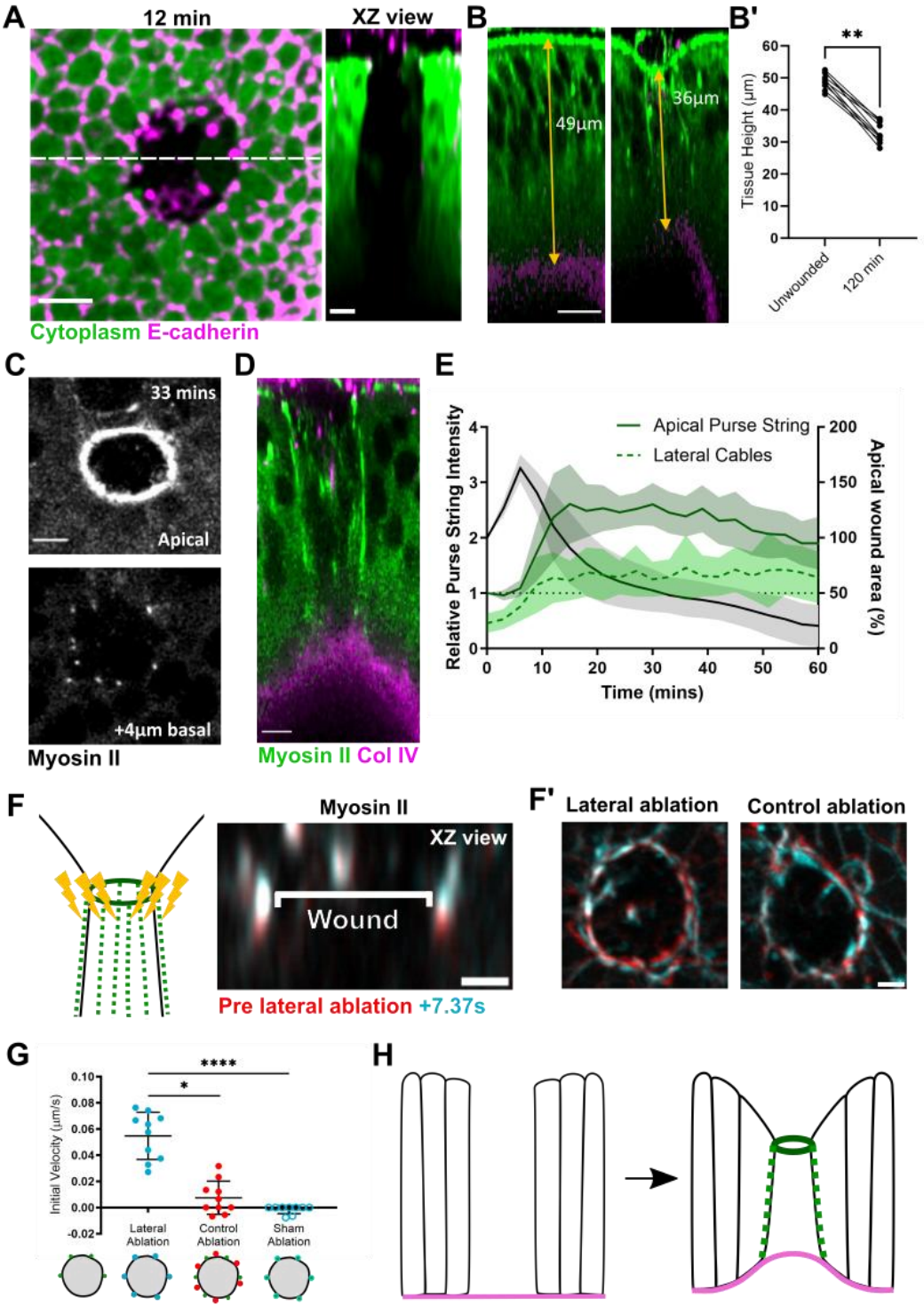

Figure 3.1: Preliminary data collected by Dr Rob Tetley.

A) Wounds in the wing disc propagate through the whole tissue. B) The apical and basal surface of the wing disc indent resulting in overall tissue shortening. B') Quantification of tissue height in unwounded discs and 120 min post-wounding. C) A conventional purse string was observed 33 min post-wounding. 4 µm below the purse string, filamentous myosin structures

are observed. D) The myosin structures stretch along the apicobasal axis of the wound edge. E) Quantification of wound area, purse string myosin intensity and lateral cable myosin intensity in the first 60 min post-wounding. F) Laser ablation of the lateral cables. F') The apical purse string before and after lateral cable ablation and control ablation. G) Recoil velocities for lateral cable ablation, control ablation and sham ablation. H) Wound edge cell shortening hypothesis. In B', ** represents $p<0.01$ from a paired Wilcoxon test. In E, lines are mean values, and shaded areas are SD. In G, lines represent means, bars represent SDs, * represents $p<0.05$, and **** represents $p<0.0001$.

These observations led to the hypothesis that a reduction of cell height at the wound edge could cause cells to increase their width, thereby reducing the area of the wound. Wound closure is accelerated by the simple 3D shape change of cells flattening into the wound gap without the need to create new cell material to compensate for lost cells or process phagocytosed dead cell debris. To drive cell shortening, we propose that wound edge cells use contractile lateral actomyosin cables due to their concomitant timing with apical indentation and drastic apical surface recoil upon their ablation. The laser ablations of the lateral cables are not further explored, as the cables rapidly reform after laser ablation. In Chapter 5, I explore permanent methods to disrupt the lateral cables by genetic perturbations. In this chapter, I quantify wound edge cell behaviour and further characterise the lateral actomyosin cables. I explore the use of expansion microscopy (ExM) to image the structure of the lateral cables and possible attachments to IACs.

3.2 Wound edge cells conserve their volume during repair

The 3D shortening hypothesis relies on the conservation of cell volume at the wound edge to force cells into flattening. Some *Drosophila* models utilise phagocytosis or endoreplication to enlarge wound edge cells during wound closure [110–113]. To verify whether volume is conserved in wing disc cells, wound edge cells must be segmented to quantify their volume. Segmentation is computationally intensive, and in previous wing disc segmentation studies,

including within the Mao lab, the maximum depth of segmentation is capped between 20-30μm as light is attenuated by the tissue [190–192]. To overcome this limitation, Dr Rob Tetley created two-cell cytoplasmic mCherry clones using the FLP/FRT heat shock system [193] and wounded adjacent cells. Consequently, the two-cell clones formed part of the row of cells lining the wound edge (Figure 3.2.A). He imaged these wound-edge cell clones at 3-minute intervals over 2 hours. As the clones are marked with cytoplasmic mCherry, there is a high concentration of fluorescence that is robust against photobleaching and axial light attenuation. Quantification of the clone cell volume and height was performed in Fiji and a python-based pipeline developed by Martin Zhang, a summer student in the Mao lab. These quantifications reveal that clone volume stays constant whilst clone height decreases throughout 2 hours of healing, supporting the 3D cell shortening hypothesis (Figure 3.2.C-E). The cell height decrease is also in agreement with the previous quantification of tissue shortening in the same timeframe (Figure 3.1.B'). A recent study in *Drosophila* embryos also found that cell volume does not change at the wound edge during closure [194].

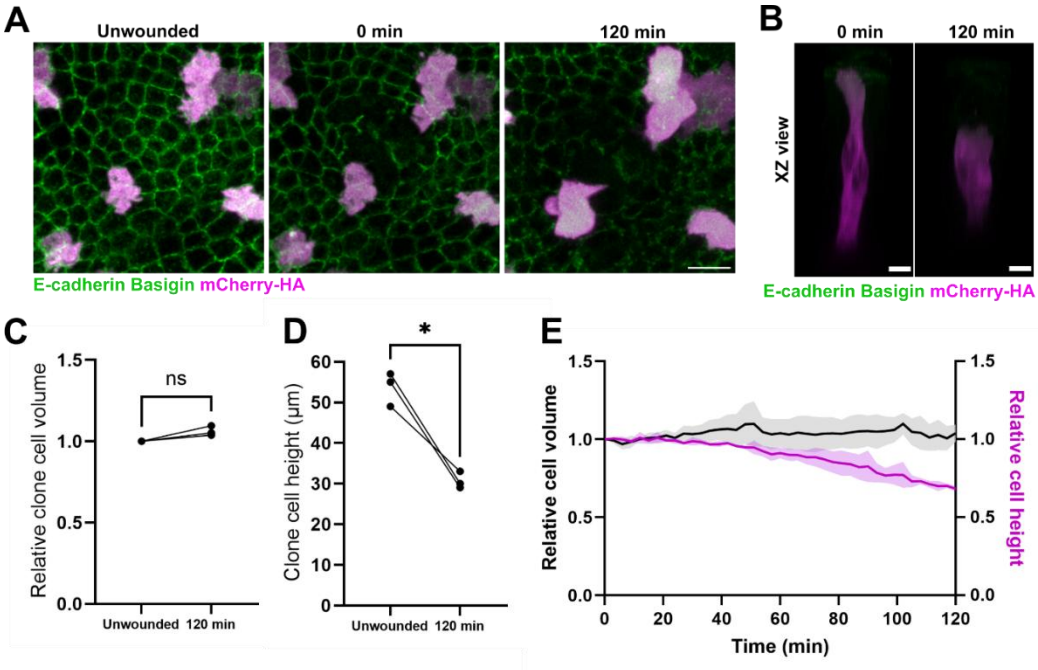

Figure 3.2: Wound edge cell clones conserve volume and decrease in height over 120 min.

A) Generation and imaging of cytoplasmic (HA) mCherry wound edge clones with membranes marked with E-cad-GFP and Basigin-GFP performed by Dr Rob Tetley. B) 3D renderings of a two-cell wound-edge clone. C) Relative clone cell volume to the unwounded (pre-wounded) cell volume (n=3 clones in separate wounds). D) Clone cell height before (unwounded) and 120 min post-wounding (n=3 clones in separate wounds). E) Relative cell volume (black) and relative cell height (magenta) as a function of time (n=3 clones in separate wounds). For C-D, ns represents $p>0.05$ and * represents $p<0.05$ from paired Wilcoxon tests. For E, solid lines are mean values, and shaded regions represent SD.

3.3 Lateral cables span the entire apicobasal axis

To further qualitatively characterise the lateral cables, I performed confocal imaging to verify that the myosin co-localised with actin. I live-imaged discs with endogenous myosin II and LifeActRuby on a Leica STELLARIS DIVE microscope, which has more sensitive hybrid detectors than the photon multiplier tube detectors on the microscope previously used to discover the cables, the Zeiss LSM 880 confocal microscope (Figure 3.3.A). These images are oversaturated to visualise the full length of the actomyosin cable across the apicobasal axis (Figure 3.3.A-B).

Myosin II appears as inhomogeneous clumps, continuous with the apical purse string (Figure 3.3.A-B). Actin accumulates as cables around the wound edge, but in comparable intensities to the lateral domains of neighbouring cells away from the wound. The myosin localises adjacent to the actin cables, which is unlikely to be a drift artefact as each channel in the image stack is collected simultaneously. Here, the enrichment of Myosin II along the Actin filament drives the filaments to slide past each other, causing contraction of the lateral domain. The cable intensity decreases with z depth, which is likely to be due to light attenuation by the tissue. Attenuation increases with the depth of the sample as biological tissue scatters and absorbs light.

Next, I investigated ways to quantify the formation of lateral cables as a function of myosin II intensity [186,195]. The most accurate measure of cable

intensity would be from segmenting the cables in 3D. This would potentially be time-consuming and manually intensive, so I investigated the feasibility of 3D cable tracking using Trackmate [196] with these oversaturated images as they would provide the best signal for the segmentation of the cables (data not shown). I applied Otsu's method to threshold the image stack and make a mask of the myosin-GFP channel in Fiji. Masks were then manually corrected in napari viewer as it is fast and responsive with 3D data [185]. Corrections involved removing lateral accumulations of myosin in unwounded cells with similar intensities to sections of the lateral cable. Of course, lateral enrichments of Myosin II are not exclusive to wound healing and contribute to normal cell processes such as cell division. Notably, the large oval-shaped myosin accumulations in Figure 3.3.B are leftover structures of the cleavage furrow from cytokinesis. As the myosin cables are discontinuous structures, correction became more subjective as the signal was weaker deeper into the tissue. As such, it was difficult determining whether myosin segments were part of the same cable, even in a heavily oversaturated sample. As experimental image stacks would not be oversaturated, I decided that manual segmentation of the cables would be too time-consuming and subject to human error. Additionally, I did not want to introduce further bias when looking for cables or the absence of cables in perturbation experiments. Methods for quantifying the lateral cables will be discussed in Chapter 5.

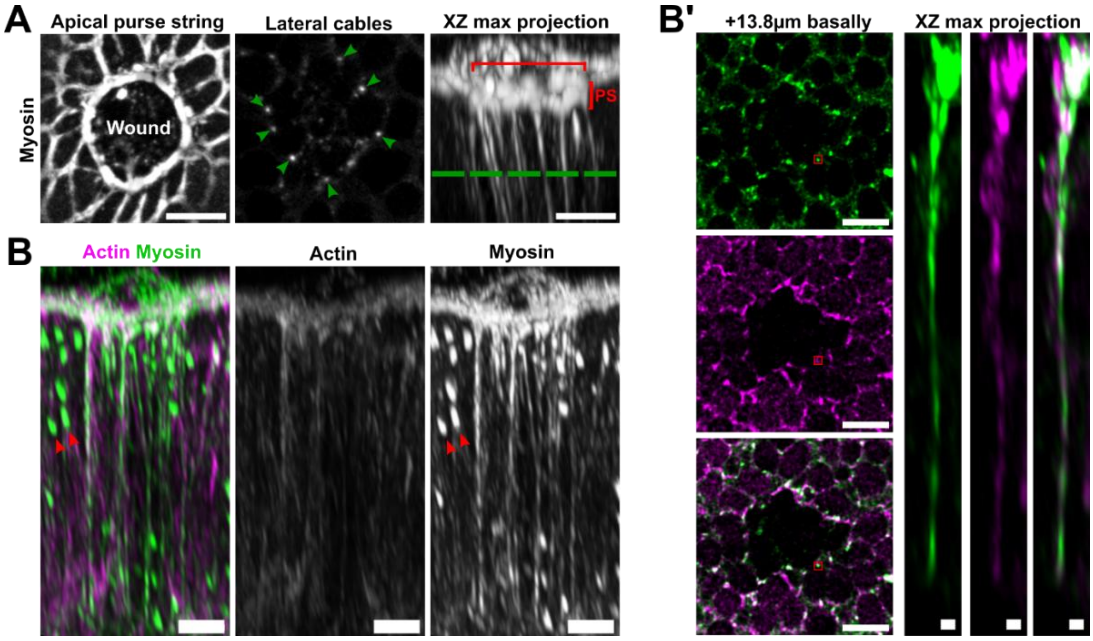

Figure 3.3: High-resolution images of the lateral cables.
A) Conventional purse string with myosin-GFP 30 min post-wounding. Images were collected on a Zeiss LSM880 with Airyscan. B-B') Oversaturated images of the lateral cables with LifeActRuby and Myosin-GFP acquired on a Leica STELLARIS DIVE microscope. B) Example of lateral cables assembling at the wound edge spanning the full apicobasal axis of the tissue. Red arrows indicate example remnants of cytokinesis myosin machinery from dividing cells. B') Image slice 13.8 μm below the purse string. Red box indicates the lateral cables XZ view shown on the right.

3.4 Cables colocalise with cell-ECM adhesion protein Talin

Preliminary imaging by Dr Rob Tetley showed that the lateral actomyosin cables appeared to contact the basal surface of the epithelial cells (Figure 3.1.D). At the basal surface, the actomyosin cytoskeleton is mechanically linked to the BM at cell-BM adhesions via Talin at integrin-based adhesions[115,11. To explore the contact between the lateral actomyosin cables and the basal cell surface, I co-imaged myosin II and talin. I imaged wounds with the Zeiss LSM 880 Airyscan detector in Super Resolution mode 30 minutes after ablation. To image the basal surface after wounding, I used the 'coverslip sandwich' mounting method as described in 2.6.

Talin localises into discrete round puncta on the basal cell membrane (Figure 3.4.A-B). The morphology of puncta are highly heterogeneous between wing discs, with shapes varying between circular and incomplete, irregular or ring-like, sometimes resembling cheetah-spot patterns with astral-like projections (Figure 3.4.C) [198]. The shapes of the puncta are likely to depend on the wing disc age as well as local variations in mechanical tension, integrin engagement or cell signalling [29,199]. Myosin II forms a ring around Talin puncta, which pepper the basal surface of the wing disc (Figure 3.4.A). There were occasional 'torpedo-like' myosin II structures projecting away from the basal surface in XZ (Figure 3.4.A''). The colocalisation of these Myosin II torpedoes with Talin suggests that Talin may serve as anchoring points for the lateral cables. It is difficult to visualise the basal cables as the debris cells

display strong basal signals at the centre of the wound, making it difficult to distinguish the cables in 2D projections (data not shown). Additionally, some cells are curved or slanted, resulting in Myosin II puncta with more smeared and elongated appearances. The location of successful wounds can be identified as the basal puncta in ablated debris cells rise above the plane of the puncta in non-ablated cells.

In the *Drosophila* embryo wounds, Talin increases by 3 ±1-fold (mean ± SD) at the wound edge over the first 40 min of healing [129]. In the wing disc, perhaps Talin is recruited closer to the wound to mediate the increased force required for cell shortening. To investigate if cell-BM adhesions are remodelled during wound closure in the wing disc, I quantified relative Talin and Myosin II intensity as a function of distance from the wound edge. I performed a sum projection as at 30 min we do not see a large deformation at the basal surface, so all z-stacks had roughly the same number of z slices. For each disc, I sum projected 100 z slices, ensuring I include the complete signal from the most basal surface. There is no correlation in either Talin or Myosin II intensity with distance from the wound edge (Figure 3.4.D-F). There is no significant difference between the distribution of Talin or Myosin intensity in wounded and unwounded discs (Figure 3.4.E and F, respectively). This negligible effect may be due to the neighbour contacts between cells. As scutoids, wing disc cells change their neighbour contacts along the apicobasal axis. Therefore, neighbouring puncta on the basal surface may not belong to neighbouring cells on the apical surface, averaging out any changes in intensity with distance.

This negligible change in Talin intensity could be because not all copies of Talin would be fluorescently tagged. These flies were male offspring from the cross between null background sqh-GFP flies and homozygous talin-mCherry flies so therefore, they only possessed one mCherry-tagged copy of *talin*. Therefore, I analysed Talin-YPet data from Chapter 4, where all copies of talin would be fluorescently marked (Figure 3.5.A). Here, max projections of the basal surfaces were taken as the basal surface starts at 60 min (data not shown). Surprisingly, I found a positive correlation between Talin intensity relative to the wound edge and the distance from the wound edge 30 min

and 60 min post-wounding (Figure 3.5.B). There was no correlation between Talin-YPet intensity and distance from the wound edge 90 min post-wounding (Figure 3.5.B).

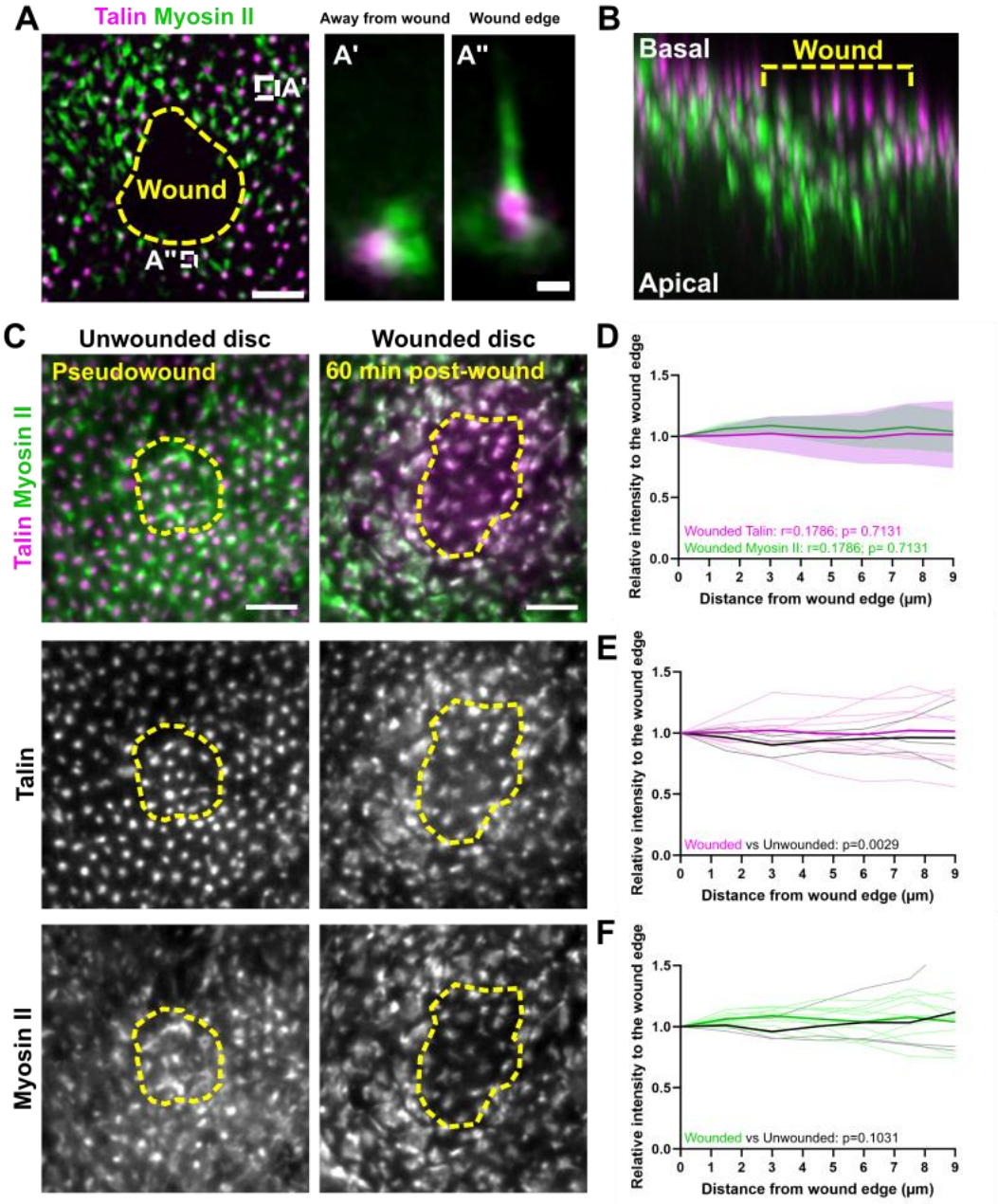

Figure 3.4: Talin and myosin colocalise on the basal surface.

A) Basal surface of wounded wing disc 30 min post-wounding. A') XZ view of Talin puncta away from the wound edge. A") XZ view of Talin puncta at wound edge with cable-like myosin structure. B) Maximum projection of XZ slices of wound in A. C) Wing disc expressing mCherry-tagged Talin and GFP-tagged myosin. Example of an unwounded control disc with a

hypothetical wound mask overlay (yellow) and a wounded disc with ablated wound mask overlay (yellow). Wing discs co-express endogenously tagged Talin-mCherry and Myosin-GFP. D) Relative mean intensity of Talin (pink) and Myosin (green) as a function of distance from the wound edge, n=10. E) Relative mean intensity of Talin as a function of distance from the wound edge in wounded (magenta, n=10) and unwounded (black, n=3) discs. F) Relative mean intensity of Myosin as a function of distance from the wound edge in wounded (n=10, green) and unwounded (black, n=3) discs. For D-F, r values are Spearman's rank-order correlation coefficients with respective p values. For E and F, individual wounds are shown in faded colours and the mean of all wounds in dark colours. In A-C, scale bars are 5 μm. In A' and A'', scale bars are 1 μm.

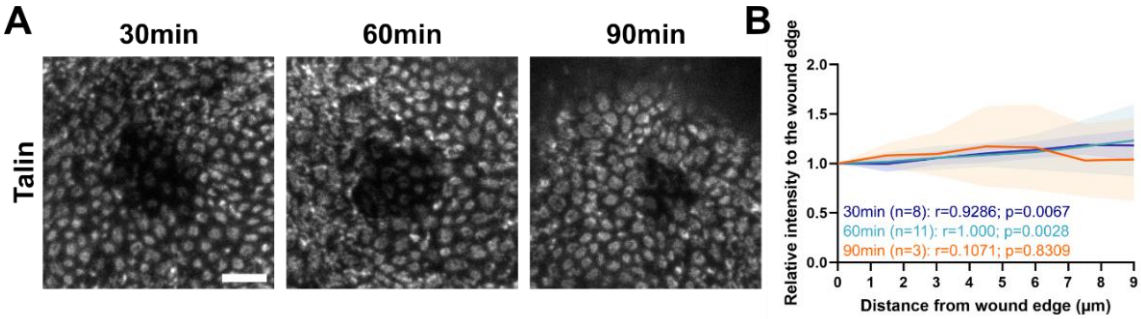

Figure 3.5: Talin-YPet intensity increases with distance from the wound edge.

A) Example images of Talin-YPet wounded discs 30 min, 60 min and 90 min post-wounding. B) Relative Mean Talin-YPet intensity vs distance from the wound edge 30 min (navy, n=8), 60 min (blue, n=11) and 90 min (orange, n=3) post-wounding. For B, r values are Spearman's rank-order correlation coefficients with respective p values. Solid lines are mean values of all wounds per timepoint, and shaded regions are SD. Scale bars are 5 μm.

A limitation of such basal wound intensity analysis is that the edge of the wound is unclear, as it is difficult to separate it from wound debris. Depending on the marker, some autofluorescence can be observed in the wound gap, as seen in both Talin and Myosin channels in Figure 3.4.C.

3.5 Expansion Microscopy to super-resolve basal surface structures

The basal surface is particularly crowded, with many proteins forming various cell-BM adhesions within a typical 2-3 μm diameter surface. As discussed previously, imaging and quantification of basal structures are restricted by the diffraction limit as well as light attenuation by the structure of the wing disc and its cell properties. As I could not sufficiently spatially resolve the myosin II structures and talin under confocal or multiphoton microscopy, I explored protein-retention expansion microscopy (Pro-ExM) closely with Dr Rob Tetley as a technique to improve the spatial resolution of my images. In parallel, our collaborator Emmanuelle Steib (Vermot lab, Imperial College London) alternatively optimised ultrastructure expansion microscopy (U-ExM), now published [200].

ExM is a super-resolution technique where following fixation, specimens are embedded in and crosslinked to swellable polymer networks, which are physically expanded [201]. Structures are expanded by approximately 4.5x with the possibility to further expand structures twice in series [202]. This increase in both lateral and axial resolution was desirable for examining both the lateral cables and the basal surface of the wing disc. However, ExM's major drawback is its incompatibility with live imaging. Other iterations of ExM have included improvements in specimen anchoring [203,204], post-expansion labelling [205] and ultrastructure expansion [206] as well as some tissue-specific variations [207–215]. *Drosophila*-specific examples include embryos [212], larval brains [212], larval and adult body walls [212], pupal wings [215] and spermatocyte centrioles [213]. Before Steib et al.'s work, there were no published examples of larval wing disc expansion.

Firstly, I tested different paraformaldehyde (PFA) concentrations for fixing unwounded wing discs, focusing on the integrity of the basal surface, which has a dense meshwork of actin and myosin II puncta. Previous immunostaining in the lab indicated that Myosin II does not fix well, so wing discs are typically fixed gently with 4% PFA for 30 minutes. However, because lateral actomyosin cables form within minutes of wounding, and

additional time is needed to unmount the wing discs after ablation, a faster fixation protocol may be necessary to accurately capture early events in wound healing.

I stained endogenous null background Myosin-GFP tagged flies with GFP-FITC and Phalloidin647 to stain f-actin. To preserve dynamic actomyosin structures during wound healing, I sought to decrease the time needed for fixation, typically 30 min for 4% PFA. Therefore, I tested higher concentrations of PFA for shorter fixation times to more rapidly crosslink cellular components before they might be redistributed or degraded. A disadvantage of using higher PFA concentrations is that some delicate structures may become excessively crosslinked, causing artificial aggregation or preventing antibody accessibility in later immunostaining. I qualitatively compared how well Myosin II was preserved when using 4%, 18% and 36% PFA in conventional slides (Figure 3.6). Myosin II structures were lost in 36% PFA, and actin appeared discontinuous compared to 18% or 4% PFA. To compromise between fast fixation and gentle PFA concentration, I proceeded with 18%.

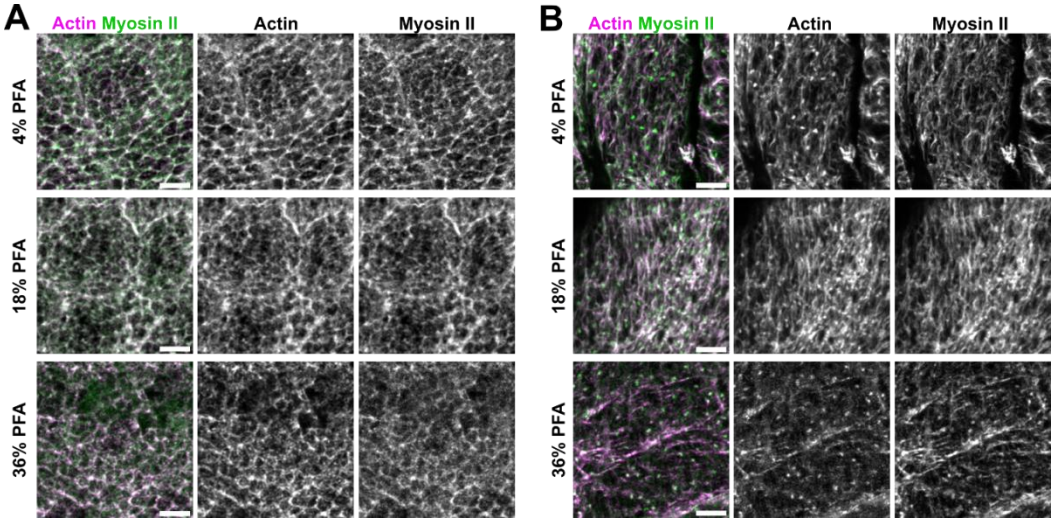

Figure 3.6: Optimising PFA fixation concentrations for Myosin II preservation.

A) Apical surface of the wing disc. B) Basal surface of the wing disc. Scale bars are 5 µm.

The ProExM protocol is described in detail in Chapter 2.5. In brief, I dissected wing discs with homozygous genotypes *sqhAX3; sqhGFP;* or ;*vkgGFP;* and fixed them as described in the previous section. Then, fixed samples were conventionally antibody-stained for Laminin (lanB1) and abundant BM components such as Integrin (mys). GFP FITC was used to stain either endogenously GFP-tagged Myosin or Collagen IV (vkg), depending on the genotype used. Next, labelled with Acryloyl-X anchors, attached to a hydrogel with an activated monomer solution (Figure 3.7.A), then mechanically homogenised Proteinase-K (Pro-K) digestion overnight (Figure 3.7.B) before finally being expanded through successive double-distilled water incubations (Figure 3.7.C). The expanded gels were trimmed and placed in 1 mL of distilled water on a glass slide for imaging (Figure 3.7.D). A consideration for mounting gels on the imaging slide was ensuring that the basal surface of the disc was close to the edge of the gel to use higher magnification objectives with lower working distances for Airyscan imaging.

To verify expansion, I compared the diameter of peripodial nuclei in unexpanded fixed slides and expanded gels and measured the expansion factor of the gels. The expanded nuclear diameter was approximately 3.5 times their unexpanded diameter, implying isotropic XY expansion (Figure 3.7.E-F). However, the myosin II signal was negligible, and the BM appeared fractured due to incomplete digestion, which prevented homogenous expansion. Instead, components seemed to bind with each other and resisted expansion into fragments.

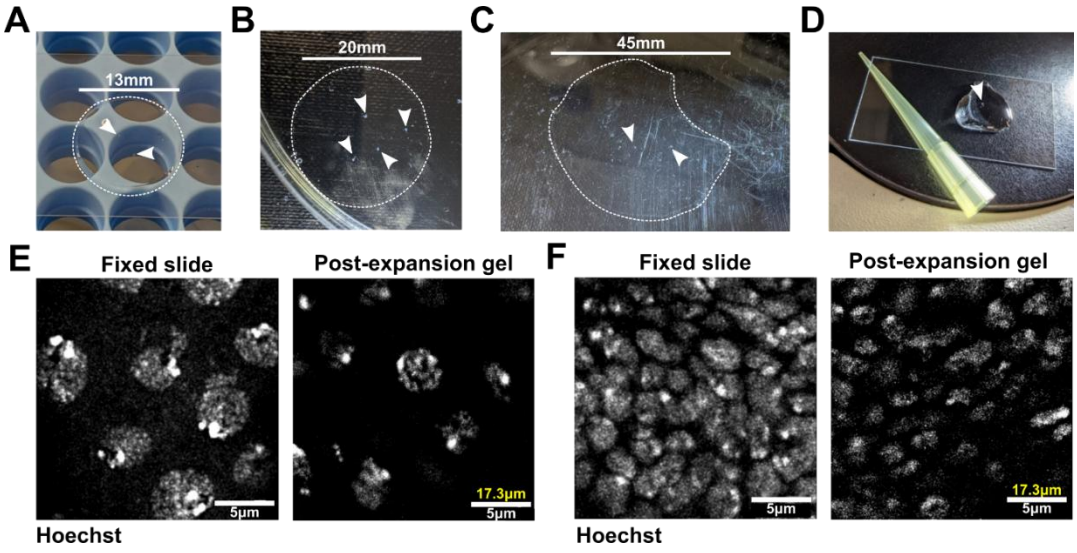

Figure 3.7: Pro-ExM gel expansion.

A) Gel after gelation step. B) Gel after the digestion step. C) Gel after the expansion step. D) Gel mounted for imaging on a coverslip with a P20 tip for scale. E) Peripodial nuclei. F) Wing disc proper nuclei. For E and F, the biological scale is in white, and the true scale is in yellow.

To optimise the digestion of BM components, I altered the concentration, temperature and duration of the digestion step. Pro-K concentrations 1% and 2% at both RT and 37°C overnight were unsuccessful in digesting the BM. Consequently, I couldn't resolve the organisation of individual BM components within the meshwork. This effect may be useful in quantifying the strength of the BM by measuring the size and separation of segments for different Pro-K concentrations. Collagenase may be more effective as it is specific to Collagen and has completely removed the BM in previous studies [144,146]. Collagen becomes very tough when fixed with formaldehyde and is resistant to Pro-K.

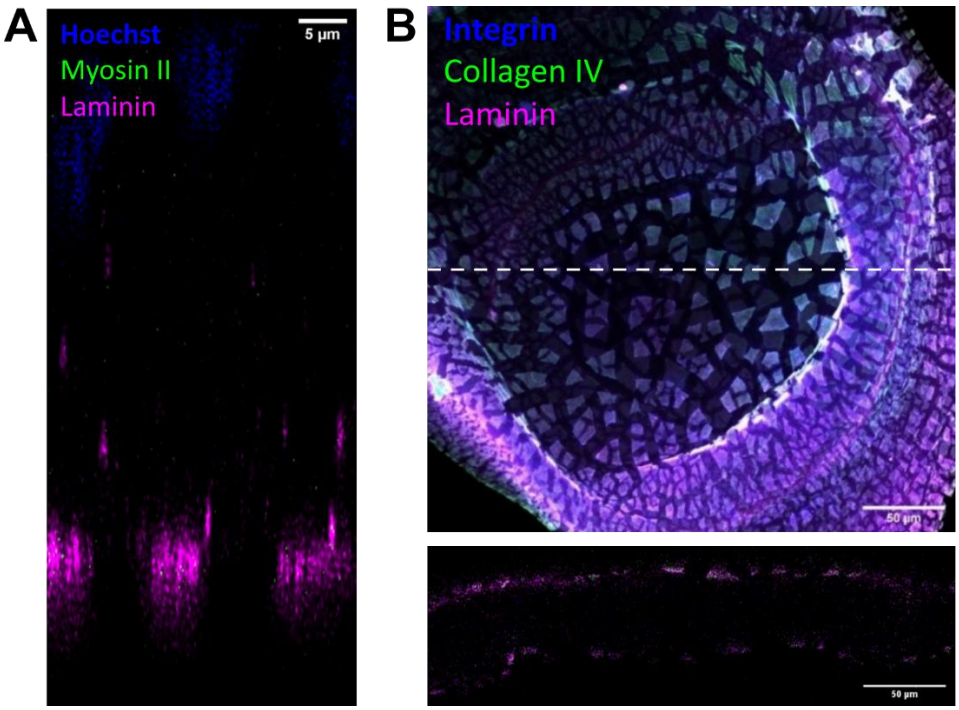

Figure 3.8: Incomplete digestion of the BM by Pro-K.

A) Cross-sectional view of an incompletely digested wing disc with genotype *sqhAX3; sqhGFP;* with Laminin (magenta), Myosin (green) and nuclei (blue). Segments of Laminin can be seen basally. B) Example of incompletely digested wing disc with genotype ;*vkgGFP*; with BM-related components stained and cross-sectional view. Segments of Integrin (blue), Collagen IV (green) and Laminin (magenta).

3.6 Discussion

In this chapter, I developed quantitative analysis of preliminary data collected by Dr Rob Tetley. Together with Martin Zhang, we confirmed that wound edge cell volume is conserved whilst cell height decreases during wound healing. This quantification confirms the prior assumption for the 3D shortening hypothesis. These experiments were performed using two cell clones; the behaviour of other wound-edge cells is unknown. For this, full segmentation of cells around the wound is required. A major challenge to segmentation is differentiating the dead cell debris signal from the wound edge cells. In future experiments, dextran could be used to mark the wound gap for segmentation. The size of dextran must be carefully determined, as some intact wound edge cells may be transiently damaged and more permeable

after wounding. These cells may absorb some dextran and, as a result, be incorrectly removed as debris in segmentation.

I show that the lateral cables span the complete apicobasal axis and are composed of Myosin II and Actin. These cables are difficult to segment along the apicobasal axis and require thorough manual correction. Such manual correction is time-consuming and subjective, particularly below 20μm from the apical surface, where the signal drops considerably. The spatial resolution of conventional confocal microscopy is limited by the diffraction limit to a few hundred nanometres. Specifically given by equations (1) and (2), laterally and axially, respectively.

$$d_{xy} = \frac{\lambda}{2NA} \qquad (1)$$

$$d_z = \frac{2\lambda}{NA^2} \qquad (2)$$

At optimum, a x63 oil objective lens (1.4 NA) and 488nm excitation laser would give a lateral resolution of 174nm and axial resolution of 498nm, whereas a myosin filament is only 10-20nm in width [216,217]. Zeiss's Airyscan aims to improve signal using a 32-channel hexagonally packed detector [218]. Consequently, raw Airyscan images must be processed under pixel reassignment and deconvolution to generate final super-resolved images [219]. In comparison, Leica's STELLARIS 8 DIVE microscope uses highly sensitive HyD hybrid detectors to improve signal-to-noise ratio (SNR) compared to conventional photon multiplier tubes (PMTs) [220]. Similarly, images can be deconvolved in Leica's LIGHTNING software to produce a final super-resolved image. Such advances in detection and image processing have allowed high-resolution images of the lateral cables but are unsuitable for their quantification. It is difficult to visualise the basolateral parts of the cables without oversaturating the apical surface of the wing disc, which has very strong Myosin II enrichment from the apical actomyosin cortex and the purse string. To compensate, adaptive laser power could be used to increase laser intensity with imaging depth. Slight variability between disc age or mounting may make comparing intensity quantifications across discs difficult.

I explored other image modalities for imaging Myosin in the complete apicobasal axis. Multiphoton microscopy seemed a promising technology as longer excitation wavelengths allow greater depth imaging and lower phototoxicity for deeper tissues. I used a Leica STELLARIS 8 DIVE equipped with a pulsed tunable and fixed (1040nm) multiphoton (2P) laser (Coherent) and non-descanned detectors (NDD). I found that multiphoton imaging lacked the resolution to capture cables. Using 924nm excitation resulted in a lateral and axial resolution of 330nm and 943nm, respectively. Furthermore, I killed my sample after imaging a few timepoints. As the epithelium is only one cell thick, it may not be as robust to photodamage as tissue of the same thickness made up of several layers of cells. Photobleaching increases exponentially with illumination power by 3-4 magnitudes [221,222].

Since performing my ExM experiments, numerous experimental modifications and tools for quantifying expansion have been published that would be useful for further wing disc gels. To address the BM digestion issues, I aim to use alternative digestion agents such as SDS in addition to Pro-K or collagenase for more aggressive digestion. Additionally, the digestion step could be repeated, and the temperature could be raised further. The phenomenon of BM patterns created by incomplete digestion under the original protocol could be used to infer structural and mechanical properties, as previously demonstrated in μExM developed for bacteria [175].

Improvements in imaging protocols for future gels include utilising spinning disc confocal microscopy to accelerate the image acquisition of expanded gels, compared to conventional laser scanning confocal microscopy. With 3.5x linear expansion, the wing disc will increase by about 40x volumetrically if expansion is isotropic. If the sample is embedded deeply in the gel, objectives with larger working distances are needed to image the sample. To minimise the distance of the sample from the edge of the gel, poly-L-lysine could be used to secure samples to the coverslip surface before gelation. The gel can be cut into an asymmetric shape to easily indicate the physical orientation of the gel. Additionally, to prevent sample drift, poly-L-lysine could be used to adhere expanded gels to the coverslip during imaging. GelMap, a gel-embedded reference grid to intrinsically calibrate hydrogel

measurements [223] would be useful to compare BM fragments from impartial digestion. Alternatively, nanobeads could be embedded in the gel to provide reference points for gel expansion. Individual gels should be imaged before expansion so that accurate expansion factors can be calculated. As gels are expanded, they have diminished fluorescence compared to their pre-expansion state, as the fluorescence signal becomes more dilute. Using a widespread, bright stain such as DAPI helps to visualise the sample within the gel. The gels could then be trimmed into non-symmetric shapes to enable easy orientation and mounting for imaging. Since U-ExM was successfully performed on unwounded wing discs, I plan to use this protocol for future ExM experiments to image IACs first, then, if successful, evaluate the feasibility of wounding wing discs before embedding them in gels for expansion.

Other super resolution microscopy techniques, such as DNA-PAINT could be used to could also be used to determine if there are any quantitative changes in talin activation or integrin clustering in wound edge cells. A recent publication demonstrates DNA-PAINT to resolve titin nano-architecture in adult *Drosophila* wings [224]. Such techniques are limited by the need for fixation and permeabilisation, rendering them impractical for visualising dynamic processes such as wound healing. Fluorescence correlation spectroscopy (FCS) has revealed that talin concentration increases over hours as the pupal wing develops [225]. FCS measures the statistical fluctuations of fluorescence intensity, which are often too small to be detected by conventional confocal microscopy. It would be interesting to perform FCS on wounded wing discs to quantify Talin density at different timepoints.

Further quantitative analysis of Talin, Integrin, and other IAC-related proteins will be conducted to evaluate wound healing at the basal surface. Additionally, the dynamics of the basal actomyosin network during wound healing and generally in morphogenesis remain unknown. Given that the wound exposes the underlying basement membrane (BM), these basal networks likely undergo significant remodelling. The neighbouring cells likely adapt their basal and basolateral surfaces to migrate over the exposed BM,

facilitating wound closure. In addition to measuring fluorescence intensity, the size and shape of these adhesions will also be measured using masking and segmentation techniques developed in Chapter 4. Understanding these processes will provide deeper insights into the coordination of basal and apical responses during tissue repair.

We can conclude that wound edge cells in the wing disc undergo 3D cell shape changes during wound healing. If the tissue cannot properly repair itself, these changes could potentially change the 3D architecture of the tissue through tissue gaps and aberrant folding. The next chapter focuses on measuring apicobasal forces during wound repair.

4 Measuring basolateral forces during wound healing

4.1 Introduction

Tissue morphogenesis and repair involve complex 3D cellular shape changes, including apical constriction, cell shortening and intercalation [58,104,121,123,124,226,227]. These cellular-level mechanical changes collectively drive tissue-level transformations such as folding, elongation, invagination and branching [3]. To achieve these shape changes, cells must generate and coordinate different forces apically, laterally and basally in a precise sequence and timing. Failure to coordinate cell shape changes can lead to developmental defects, inflammatory disease, cancer and metastasis [3,227–229].

The primary generator of such forces is the actomyosin cytoskeleton, which responds to both internal and external cues [58]. Additionally, cell adhesions play crucial roles in sensing and transmitting forces between cells and their external environments. *In vivo* force measurements of forces have been vital in elucidating the role of mechanics in cell shape and identifying the responsible molecular mechanisms. Outside of standard scratch wound migration studies [64,230], there have been no published studies reporting force measurements in the context of wounding in tissues. In this chapter, I set to quantify the mechanical forces driving 3D shape changes during healing.

We previously showed that wound edge cell height decreases whilst cell volume is conserved during healing. We hypothesised that the contraction of lateral actomyosin cables causes cell shortening in wound-edge cells. To determine if there was tension across the lateral cables, Dr Rob Tetley used laser ablation to cut the cables. Laser ablation is used to generate a sudden force imbalance in living tissues. If tissue tension is present, surrounding cells recoil in reaction before moving to restore mechanical equilibrium.

Quantifying this recoil velocity allows the inference of the relative contractile forces across the ablated region [231].

Upon ablating all the lateral cables present in a wound in a single z plane, Rob measured a strong recoil of the apical purse string and an increase in the apical wound area (Figure 3.1). Control ablations in the cell cortex adjacent to the lateral cables resulted in negligible recoil and no change in the apical wound area. These results indicate the presence of contractile forces at the lateral cables that pull on the apical surface at the wound. A similar mechanism was reported in the *Drosophila* leg disc, where tissue folding is driven by an apoptotic nucleus that is apically and basally anchored by an actomyosin cable. The contraction of the apico-basal cable deforms the apical surface. When this cable was ablated, there was a rapid retraction of the apical surface, whilst ablation of non-apoptotic cells in the same lateral region resulted in negligible recoil [123].

While laser ablation and subsequent recoil velocities provide insights into relative tensions between cells, this technique cannot identify the precise mechanisms of force generation and distribution, and it is hard to follow tension changes over time. Tension can arise from various sources located apically, basally or laterally within cells, such as the actomyosin cortex, cell-cell junctions or cell-BM adhesions. Moreover, the dynamic nature of wound healing further complicates the interpretation of tension measurements from ablation studies. In steady state scenarios, the behaviour of cells can be attributed to the ablation rather than ongoing dynamic processes in the tissue. To further investigate the contractile forces generated by the lateral cables, I sought to measure these forces using a Förster resonance energy transfer (FRET) Talin tension sensor (Talin-TS). This approach will provide more quantitative insights into the mechanical forces at play during wound healing and cell shape changes.

4.1.1 FRET-based tension sensors

There are many biophysical tools available to measure cellular forces quantitatively, particularly *in vitro* [232]. In contrast, it remains highly challenging to measure forces *in vivo* as some methods require invasive

preparation, such as the insertion of magnetic beads or direct physical manipulation to disrupt the tissue [233,234]. Genetically encoded FRET tension sensors offer a non-disruptive approach to measure forces during normal cell behaviours *in vivo* [233,234]. FRET-based TS modules are inserted into target proteins involved in mechanosensing to measure molecular forces. Genetically encoded FRET tension sensors have been successfully used to measure pico-Newton (pN) forces across several mechanosensitive proteins such as E-cadherin [230], talin [225,235] and vinculin [233].

To measure the possible forces exerted on IACs by the lateral cables during wound healing, I utilised flies expressing FRET-based Talin tension sensors (Talin-TS) generated by Lemke et al [225]. Talin was chosen as a potential basal anchor for the lateral cables as previous imaging showed co-localisation of cable-like Myosin structures with Talin puncta at the wound edge (Figure 3.3). Additionally, deformation of the BM was highly correlated with Myosin intensity at the basal surface (Figure 3.1). IACs are well-established regions of contact between the cell and BM [11]. There has been previous evidence of the dependence of myosin cable contraction on basal anchoring via Talin in *Drosophila* leg disc folding [123]. When Talin was inactivated, the apical surface failed to deform. Talin is a mechanosensitive core component of IACs. The N-terminal head domain of Talin binds to Integrin whilst its long flexible rod domain can bind actin directly or via vinculin [14–16]. Force is transmitted by Talin through the unfolding of its rod domains in a force-dependent manner [16]. Its weakest rods typically unfold at forces of 5 pN whilst its stiffer rods unfold between 10-20 pN [34,236].

FRET tension sensors consist of an elastic mechanosensitive linker peptide between two fluorophores belonging to a FRET pair. The mechanosensitive linker determines the distances between the two fluorophores. When the linker is relaxed, the fluorophores are positioned in close proximity to one another, allowing FRET to occur. FRET is a process where an excited fluorophore known as “the donor”, non-radiatively transfers energy to another fluorophore known as ”the acceptor”. The acceptor fluorophore is indirectly excited by the donor fluorophore, resulting in light emitted in the acceptor’s

emission wavelength. The distance between the donor and acceptor fluorophore is inversely related to how effectively energy is transferred via FRET known as FRET efficiency. This is defined by the Förster distance dependence equation:

$$E = \frac{{R_O}^6}{({R_O}^6 + r^6)}$$

Where E is the FRET efficiency, R_O is the distance with a 50% transfer efficiency, and r is the distance between the donor and acceptor fluorophores.

FRET efficiency is highest when the donor and acceptor fluorophores are within 10 nm of each other. Under low tension, the linker remains in a relaxed, coiled state, keeping the fluorophores close together and allowing for high FRET efficiency. In contrast, under high tension, the linker stretches, increasing the distance between the fluorophores and reducing FRET efficiency. Additionally, FRET efficiency is related to the spectral overlap of the fluorophores. The emission spectra of the donor needs to overlap with the excitation spectra of the acceptor. The relative alignment of the fluorophores' transition dipoles also affects FRET efficiency.

Lemke et al. inserted three genetically encoded sensors into the endogenous *talin* (*rhea*) gene via clustered regularly interspaced short palindromic repeats (CRISPR)/CRISPR-associated protein 9 (Cas9) genome engineering and ϕC31-mediated cassette exchange [225]. They used the sensors to measure *in vivo* forces in developing *Drosophila* wing muscles and validated the functionality of the Talin-TS flies by analysing localisation, western blot analysis, sarcomere length in flight muscles, adult flight ability and molecular dynamics via fluorescence recovery after photobleaching (FRAP) [225].

The Talin-TS modules are composed of a YPet-mCherry FRET pair sandwiching different mechanosensitive linkers. These are Flagelliform (F40), Villin headpiece peptide (HP), and HP's stable variant (HPst) which are sensitive to forces between 1-6pN, 6-8pN and 9-11pN, respectively [237,238]. The Talin-TS are inserted between the Talin head and rod domains whilst their respective tension-insensitive controls (C-F40-TS, C-TS,

C-stTS) are positioned C-terminally. YPet and mCherry will be referred to as the donor and acceptor, respectively. Linker and C-terminal located constructs will be referred to as linker and Cterm constructs, respectively.

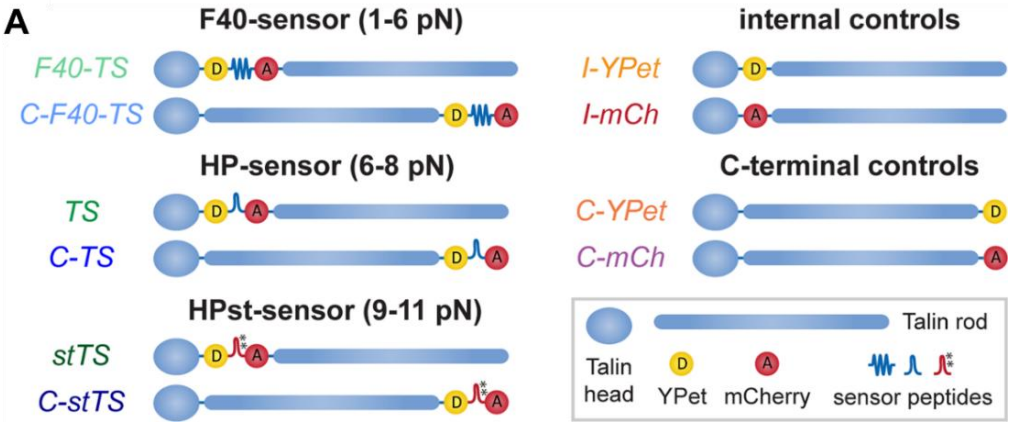

Figure 4.1: Talin tension sensor and control flies.

A) Left: Tension sensors with 3 different mechanosensitive linker peptides inserted internally (F40-TS, TS, stTS) or at the C-terminus (C-F40-TS, C-TS, C-stTS). Right: Internal and C-terminal controls with the individual fluorescent proteins from the FRET pair (I-YPet, I-mCh, C-YPet, C-mCh). Adapted from [225].

4.1.2 Sensitized emission

The simplest method to detect FRET is sensitized emission, where the acceptor's emission intensity is measured while exciting the donor. When FRET occurs, the donor's emission decreases while the acceptor's emission increases. The relative shift in acceptor and donor intensities as a result of FRET can indicate the FRET efficiency. If high FRET is occurring, the fluorophores must be close together. Here, FRET efficiency is the fraction of the acceptor's emission intensity relative to the total emission from both the donor and acceptor. The relationship is expressed by the equation:

$$E = \frac{I_A}{I_A + I_D}$$

Where E is the FRET efficiency, I_A is the intensity of the acceptor under donor excitation, and I_D is the intensity of the donor under donor excitation. However, there will be crosstalk artefacts due to the spectral overlap

between the donor and acceptor channels. To correct for these effects, careful controls must be implemented, including imaging donor-only and acceptor-only samples under donor and acceptor excitation, respectively (Table 4.1). When FRET samples are imaged, the acceptor intensity can be corrected for crosstalk artefacts (Chapter 4.2). These steps will be outlined in detail in the following subsections. This approach, known as three-channel emission measurement, ensures more accurate FRET quantification [239]. This ratiometric approach to calculating FRET efficiency also normalises for variations in sensor concentration and excitation laser intensity between different images, particularly in live samples. Additional ratios, generally named FRET indices, may be calculated to allow further relative comparisons between samples and are experiment-dependent. For example, I calculate a FRET index to compare the FRET efficiency relative to the wound edge in each disc (Chapter 4.3). Numerous methods to calculate FRET efficiency and FRET index have been previously reported [240].

Sensitised FRET can be performed in conventional fluorescence microscopes without the need for specialised equipment. Alternatively, Fluorescence Lifetime Imaging Microscopy (FLIM) is a popular method to image FRET, but can be unsuitable for technical reasons discussed in section 4.4. I measured FRET through sensitised emission on a Zeiss LSM880 confocal microscope with Airyscan equipped with 514nm Argon and 561nm Diode-Pumped Solid-State lasers. I used the Airyscan detector in confocal mode to take advantage of its improved SNR compared to standard photon multiplier tubes [218,219]. Discs were mounted with the coverslip sandwich method to bring both their apical and basal sides as close to the objective as possible for wounding and imaging, respectively. Stacks of 10-20 0.3 µm-thick z-slices were acquired for each region. The basal surface is curved, so z-stacks of varying heights were acquired. For each stack, images were collected in the acceptor, FRET and donor channels. Before wounding experiments, unwounded donor-only and acceptor-only control discs were imaged, and correction factor equations were calculated, which are discussed in the following subsection.

4.2 Controls and Correction Factors

Although YPet and mCherry are well-optimised for FRET due to their strong spectral overlap, high quantum yield and photostability [241], some spectral crosstalk remains (Figure 4.2). The FRET channel intensity must be corrected to account for spectral crosstalk artefacts known as cross excitation and bleedthrough. Cross excitation is the direct excitation of the acceptor by the donor excitation laser which can be expressed as a fraction of acceptor intensity. Whereas bleedthrough is the leak through of donor emission into the FRET channel which can be expressed as a fraction of donor intensity. The corrected FRET intensity, I_A^{corr} is given by:

$$I_A^{corr} = I_{FRET} - I_{Cross\ Excitation} - I_{Bleed\ Through} = I_{FRET} - I_A CE - I_D BT$$

where I_{FRET} is the intensity measured in the FRET channel, $I_{Cross\ Excitation}$ is the intensity contribution due to cross excitation and $I_{Bleedthrough}$ is the intensity contribution due to bleedthrough. CE and BT are correction factors for cross excitation and bleedthrough, respectively. Then, FRET efficiency would be given by:

$$E = \frac{I_A^{corr}}{I_A^{corr} + I_D}$$

Donor and acceptor only controls in cross excitation and bleedthrough conditions are used to calculate correction factors as a function of the mean fluorophore intensity of each image (Figure 4.3A-D). One area in the pouch region closest to the coverslip was imaged for each unwounded disc. Separate donor-only and acceptor-only images were collected for the linker and Cterm control constructs to generate a correction function for the cross excitation and bleedthrough factors for the linker and Cterm TS constructs, respectively.

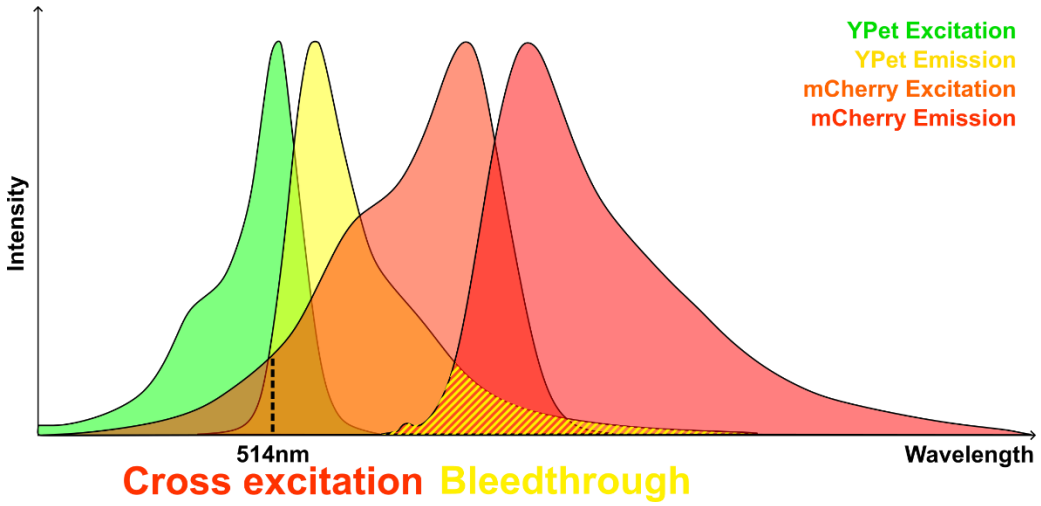

Figure 4.2: Excitation and emission spectra for YPet and mCherry.

Cross excitation occurs when the acceptor, mCherry is directly excited by the excitation laser at 514nm. Bleedthrough is indicated by the yellow stripes under the YPet emission spectra where YPet emission intensity will be detected in the FRET channel, alongside acceptor emission.

Control	Excitation wavelength	Detection wavelengths	Channel measures:
Acceptor-only (mCherry)	514	584nm – 696nm	Cross excitation
	561	584nm – 696nm	Total acceptor intensity
Donor-only (YPet)	514	519nm – 583nm	Total donor intensity
	514	584nm – 696nm	Bleed through

Table 4.1: Summary of cross excitation and bleed through control channels.

All channels were imaged with stacks of 512x512 frames with 10% laser power and 800 gain settings

Correction factors were calculated using custom ImageJ scripts written together with Dr Rob Tetley. This workflow was based on published ratiometric FRET ImageJ plugins [242,243] and other FRET-TS studies [244]. In brief, the correction factor analysis involves the following steps: maximum projection of the basal surface, Z stack registration with the Correct 3D drift ImageJ plugin, splitting the channels, applying a median filter

with radius of 1 pixel, background subtraction using the mode intensity value, otsu thresholding to create a mask of Talin puncta, applying the mask to images, assigning NaN values to zero-intensity pixels and finally, calculating correction factors on a pixel-by-pixel basis. Specifically, for each pixel, the cross excitation (or bleedthrough) channel is divided by the acceptor (or donor) only channel using the image calculator. The mean correction factor is calculated for each image and plotted against the mean intensity for each image. These individual points are fitted to a one-phase exponential decay in GraphPad Prism 10 (Figure 4.3.A-D).

The correction factor equations for the linker constructs are:

$$CE_{factor} = 0.9461e^{-0.5955mCherry_{mean}} + 0.3319$$

$$BT_{factor} = 0.3609e^{-0.1856YPet_{mean}} + 0.1425$$

The correction factor equations for the Cterm constructs are:

$$CE_{factor} = 0.7652e^{-0.2013mCherry_{mean}} + 0.0904$$

$$BT_{factor} = 0.5882e^{-0.2545YPet_{mean}} + 0.1107$$

The correction factors vary between the Cterm and linker constructs, suggesting that the difference in fluorophore positioning may influence FRET interactions. Additionally, there may be differences in protein conformation, expression levels and localisation between the constructs. There is a particularly high error in the mCherry fitting because of the very low mean intensities measured from each disc (Figure 4.3.E). The mean intensities are 3.537±0.806, 7.080±1.746, 5.307±2.512 and 8.217±2.877 for the linker mCherry, linker YPet, Cterm mCherry and Cterm YPet constructs, respectively. There are no significant differences between the YPet linker and Cterm mean pixel intensities (p=0.1887, t-test), whereas there is a significant difference between the mCherry linker and Cterm mean pixel intensities (p=0.0017, t-test) (Figure 4.3.E). There are weakly significant differences (p=0.0429, t-test) between the YPet linker and Cterm (bleedthrough) correction factors with means of 0.2442 ±0.0409 and 0.2026 ±0.066, respectively (Figure 4.3.F). There are weakly significant differences

(p=0.0165, t-test) between the mCherry linker and Cterm (cross excitation) correction factors with means of 0.4595 ±0.077 and 0.3773 ±0.103, respectively (Figure 4.3.F).

The mean intensities from the donor and acceptor channels in the wounded Talin-TS construct discs will be used together with the equations above to find the correction factors for each image stack.

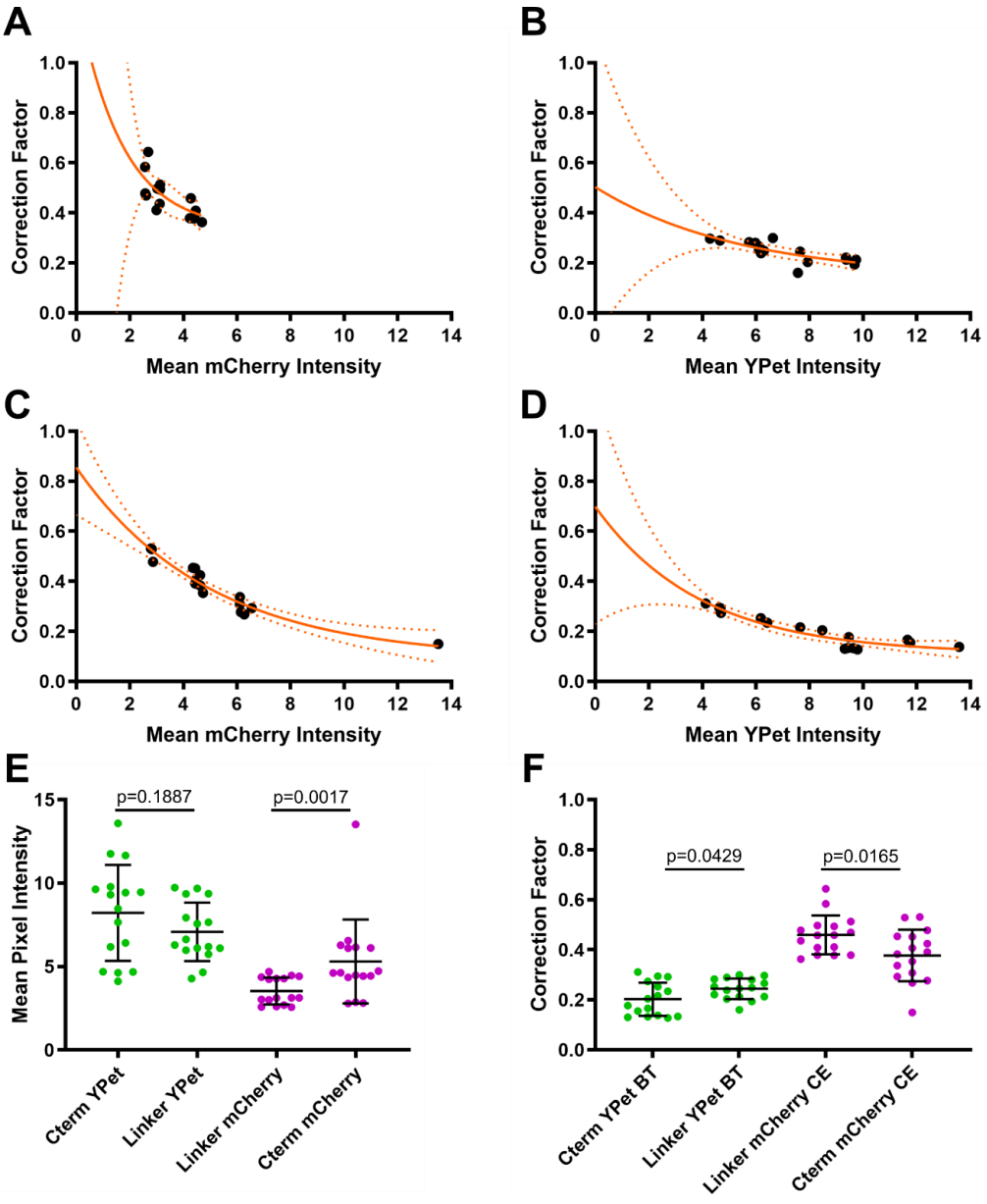

Figure 4.3: Fitting of correction factor equations for cross excitation and bleed through.

A) Mean cross excitation correction factor vs mean linker mCherry intensity (n=16 discs). B) Mean bleedthrough correction factor vs mean linker YPet

intensity (n=16 discs). C) Mean cross excitation correction factor vs mean Cterm mCherry intensity (n=16 discs). D) Mean bleedthrough correction factor vs mean Cterm YPet intensity (n=16 discs). E) Mean pixel intensity for each control genotype. For A-D, individual discs are plotted as black dots, and orange lines are fitted from one phase decay curves with dotted lines representing 95% confidence intervals. For E and F, plots show individual data points with the mean (horizontal line), SD (bars) and p values from t-tests with Welch's correction.

4.3 Measuring FRET efficiency and FRET index

Wing discs are mounted using the coverslip sandwich method and wounded apically as described in Chapter 2.6. The coverslip sandwich is then flipped, and the wing discs are imaged basally either 30 min, 60 min or 90 min after wounding. As high laser power was needed to sufficiently excite the fluorophores, only one time point per disc was imaged to prevent photobleaching effects. Talin localises into circular puncta located in the basal medial regions of the cells, as previously described in Chapter 3.4 (Figure 3.4 and [198]). The wound site is located on the basal surface using transmitted light. The wound appears as a darker region compared to its surrounding live cells. Intensity measurements are collected from the donor, FRET, and acceptor channels. The imaging parameters for each channel are summarised below:

Channel	**Excitation wavelength**	**Detection wavelengths**	**Images will measure:**
Donor	514	519nm – 583nm	Total donor intensity
FRET	514	584nm – 696nm	1) Acceptor intensity due to FRET 2) Cross excitation 3) Bleed through
Acceptor	561	584nm – 696nm	Total acceptor intensity

Table 4.2: Summary of FRET imaging channels.

All channels were imaged with stacks of 512x512 frames with 10% laser power and 800 gain settings.

In brief, the FRET analysis workflow involves the following steps: maximum projection of the basal surface, Z stack registration with the Correct 3D drift ImageJ plugin, splitting the channels, applying a median filter with radius of 1 pixel, background subtraction using the mode intensity value, otsu thresholding to create a mask of Talin puncta, applying the mask to images, assigning NaN values to black pixels, calculation of the cross excitation and bleed through correction factors from the mean intensity of the donor and acceptor channels respectively, applying the respective correction factors to the FRET image producing a corrected FRET image and finally, calculating FRET index pixel by pixel by using the image calculator to divide the corrected FRET channel image by the total donor intensity and corrected FRET intensity.

The mean cross excitation correction factor was 0.4812 ±0.0294 and the mean bleed through correction factor was 0.1900 ±0.0225. The range of cross excitation and bleed through correction factors were 0.1124 and 0.0797, respectively. The low ranges and standard deviations of both cross excitation and bleedthrough correction factors show that they were similar across wounded discs, suggesting that discs emitted consistent mean donor and acceptor intensities across different imaging sessions (Figure 4.3.C).

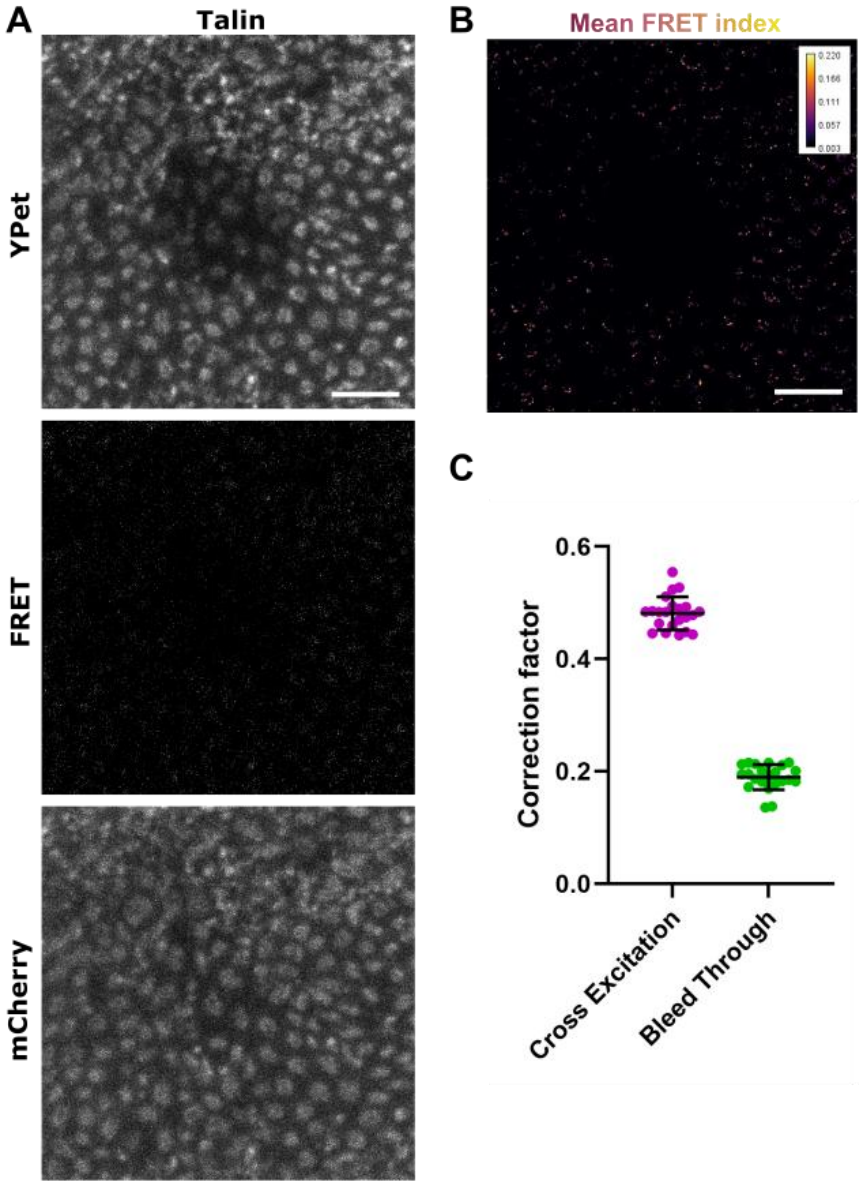

Figure 4.4: Examples from each FRET image channel.

A) Example images for the donor, FRET and acceptor channel, respectively. B) FRET index calculated from images in A. C) Cross excitation and bleed through correction factors calculated for all wing discs (1-6pN and 6-8pN linker and Cterm constructs) and timepoints shown as individual data points. Horizontal lines are the mean, and the bars are SD. n=30 wounded wing discs. Scale bars = 5μm.

I next investigated whether there was a relationship between FRET index and distance from the wound edge. To define the wound edge, I manually outlined the wound edge and made a binary mask of the wound gap using a maximum projection of the YPet channel for each wound, as this is the

strongest intensity channel, so the wound could be easily identified. Using a Python script, I calculated the distance from each pixel within the cell area to the nearest point on the wound edge mask. Then, I plotted individual FRET index values against distance from the wound edge to determine whether Talin TS closer to the wound exhibited different levels of activation compared to those farther away (Figure 4.5A–F). There were no clear trends in the FRET index and distance from the wound edge in either the 1-6pN, 6-8pN or tension-insensitive Cterm 6-8pN TS at any timepoint. The repetitive horizontal lines seen in the scatterplots are likely a technical artefact, resulting from the FRET index being saved to only three decimal places. This, combined with the inherently low dynamic range of the FRET signal, leads to visible steps in the plotted data.

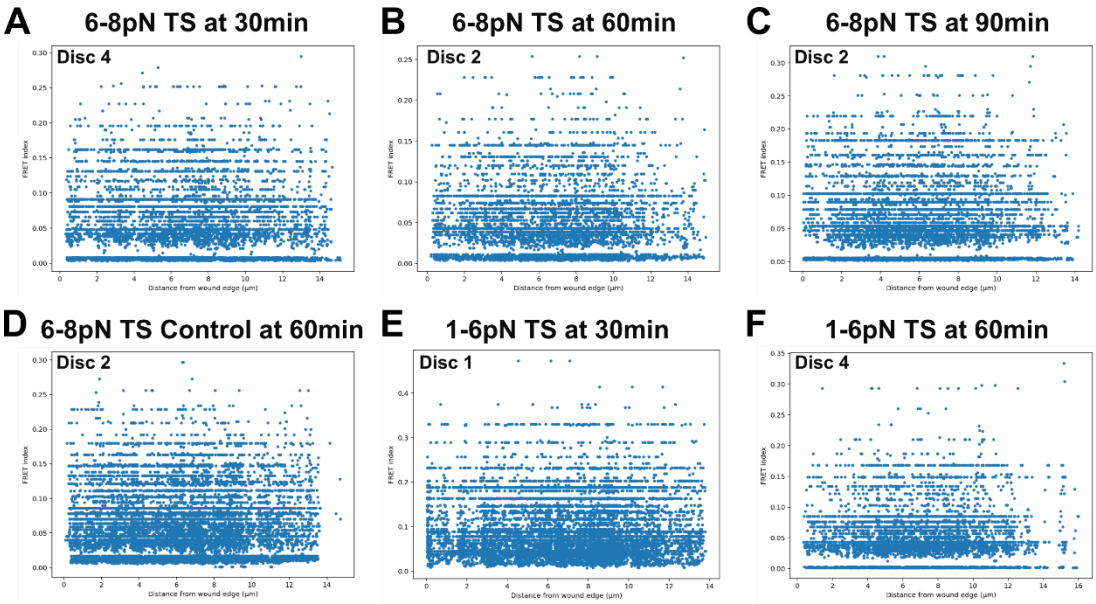

Figure 4.5 FRET index against distance from the wound edge

Example scatterplots of FRET index against distance from the wound edge (μm). A) 6-8pN TS at 30 min. B) 6-8pN TS at 60 min. C) 6-8pN TS at 90 min. D) 6-8pN TS Cterm at 30 min. E) 1-6pN TS at 30 min. F) 1-6pN TS at 60 min.

As discussed previously, I hypothesised that Talin in the wound edge cells would be under higher tension than Talin in cells away from the wound edge due to the contractile forces exerted by the lateral cables at the wound. Consequently, I expected to measure a lower FRET index in regions at the

wound edge. As there were no clear trends in plotting FRET index values against distance from the wound edge, I binned FRET index values into 1 μm-wide bands extending away from the wound edge, using the same spatial binning strategy described in Chapter 3.4 for Talin fluorescence analysis (Figure 4.6A–A'). Then, custom ImageJ scripts were used to make band-shaped masks and calculate the mean FRET index of each band as discussed in Chapter 2.8.2.

As more wing disc samples were analysed, it became clear that the diameter, shape and spatial arrangement of Talin puncta could vary. The Talin TS construct appeared to localise into puncta with different shapes compared to those observed in flies expressing the C-terminal control constructs (see Chapter 3, Figure 3.4). Specifically, the Talin TS construct displayed a pattern resembling the cheetah-spot-like myosin-GFP puncta shown in Figure 3.4, whereas the control Talin predominantly localised into more uniform, circular puncta. This suggests that the presence of the force-sensitive linker may influence Talin localisation within the wing disc, while its localisation in the pupal wing remains unaffected [225].

Additionally, as the pouch region is a curved bowl shape, when imaging the basal surface, the edges of the pouch regions can overlap. As such, Talin puncta in some areas around the wound were obscured by Talin puncta on the opposing overlapping surface. For example, in Figure 4.6.A, the Talin puncta in the upper region of the image appear smudged, which is probably due to this overlap effect. Individually segmenting puncta means I can exclude such regions from analyses and account for variation in puncta size, shape and arrangement. Therefore, in addition to the band analysis, I segmented individual Talin puncta using a pre-trained network in Cellpose 2.0 followed by manual correction in napari (Figure 4.6.B) [185,245]. In Cellpose 2.0 the cyto2 pre-trained network was used with the following parameters: cell diameter of 15, flow threshold of 0.4 and cell probability threshold of 0.0. Common errors that need to be manually corrected in napari include merging of adjacent puncta and removing puncta in possible regions of tissue folding. Next, I manually labelled puncta according to cell row (Figure 4.6.C). Custom Python scripts were used to calculate the mean

for labelled puncta (Figure 4.6.D) and the mean for each cell row (Figure 4.6.E).

Binning was used to reduce noise and reveal subtle spatial trends in FRET index that may not be evident in raw data. Previous studies in both cell culture scratch assays [68] and in *Drosophila* embryo wounds [105] have shown that cells behind the wound edge undergo shape changes and increased mobility in a graduated manner, suggesting possible spatial variation in mechanical tension. Additionally, binning allows for comparisons between cell rows across different wounds, as puncta shape and size are highly heterogeneous across different wing discs. However, binning in cell rows may also mask cell-to-cell and intracellular variability.

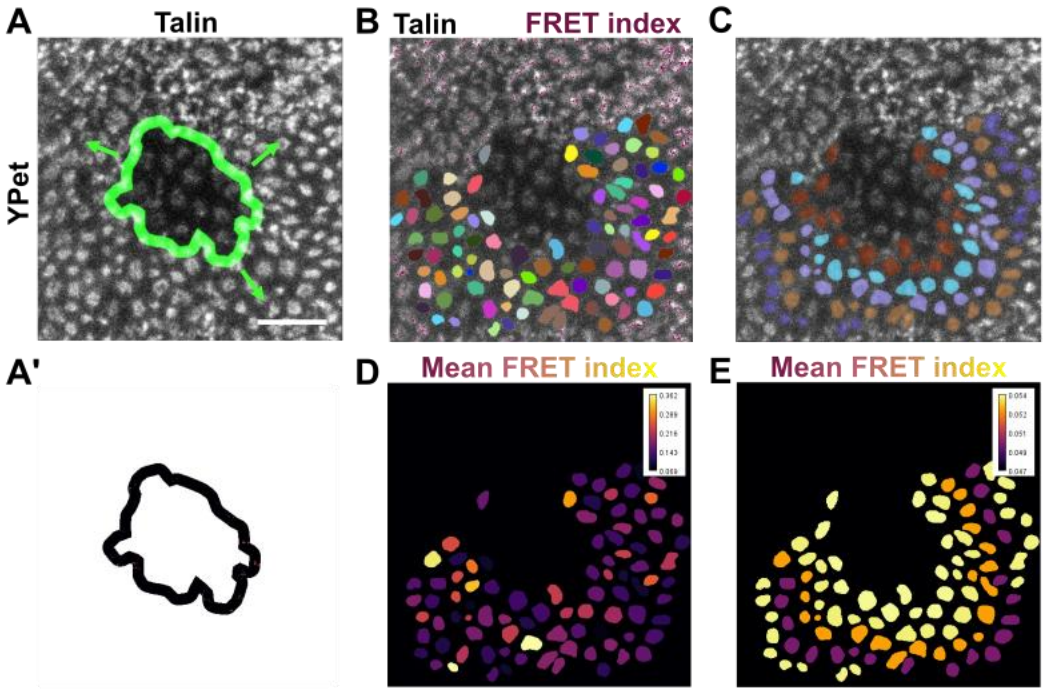

Figure 4.6: Examples of wound edge distance bands and puncta segmentation.

A-A') Example of wound edge mask. B) Example of segmented puncta. C) Segmented Talin puncta coloured by mean FRET index per puncta. D) Talin puncta labelled by row from the wound edge. E) Cell row Talin puncta coloured by mean FRET index per row. Scale bars are 5µm.

4.4 Preliminary force measurements in wounded wing discs are inconclusive

After binning in bands or cell rows as described in the previous section, the mean FRET index is plotted by distance from the wound edge (Figure 4.7.A & E) and cell row, respectively (Figure 4.7.C). To emphasise any spatial trends, the mean FRET index is also normalised to the mean FRET index of the band closest to the wound edge or cell row, respectively (Figure 4.7.B, D & F). Segmenting of Talin puncta is still ongoing, and only a subset of segmented 6-8pN TS and 6-8pN Cterm TS experiments are shown in Figure 4.7.C-D. 1-6pN TS wounds are presently being segmented.

Overall mean FRET index values are low, falling between 0.06 and 0.08 for all timepoints (Figure 4.7.A & E). This indicates that the Talin-TS in the wing disc are not experiencing significant levels of tension or stretching in the regions surrounding the wound. There was no significant correlation between mean FRET index and distance away from the wound edge (Figure 4.7.A-B) or between mean FRET index and cell row away from the wound edge (Figure 4.7.C-D) at any timepoint after wounding. This suggests that the Talin-TS are in similar conformations in the regions around the wound. Presently, these results are difficult to interpret without the inclusion of enough tension-insensitive Cterm controls (presently, n=2). These controls are needed to rule out other potential factors influencing the FRET index, which will be discussed in the next section.

There was a significantly negative correlation in mean FRET index as distance from the wound edge increased with the 1-6pN Talin-TS at 30 min (Figure 4.7.E & F). 60 min post-wounding, there was no significant correlation between mean FRET index and distance away from the wound edge (Figure 4.7.E) or cell row away from the wound edge (Figure 4.7.F). Again, tension-insensitive Cterm controls are needed to fully interpret the 1-6pN TS results. In this case, binning did not reveal trends that were not already apparent in the raw scatterplots.

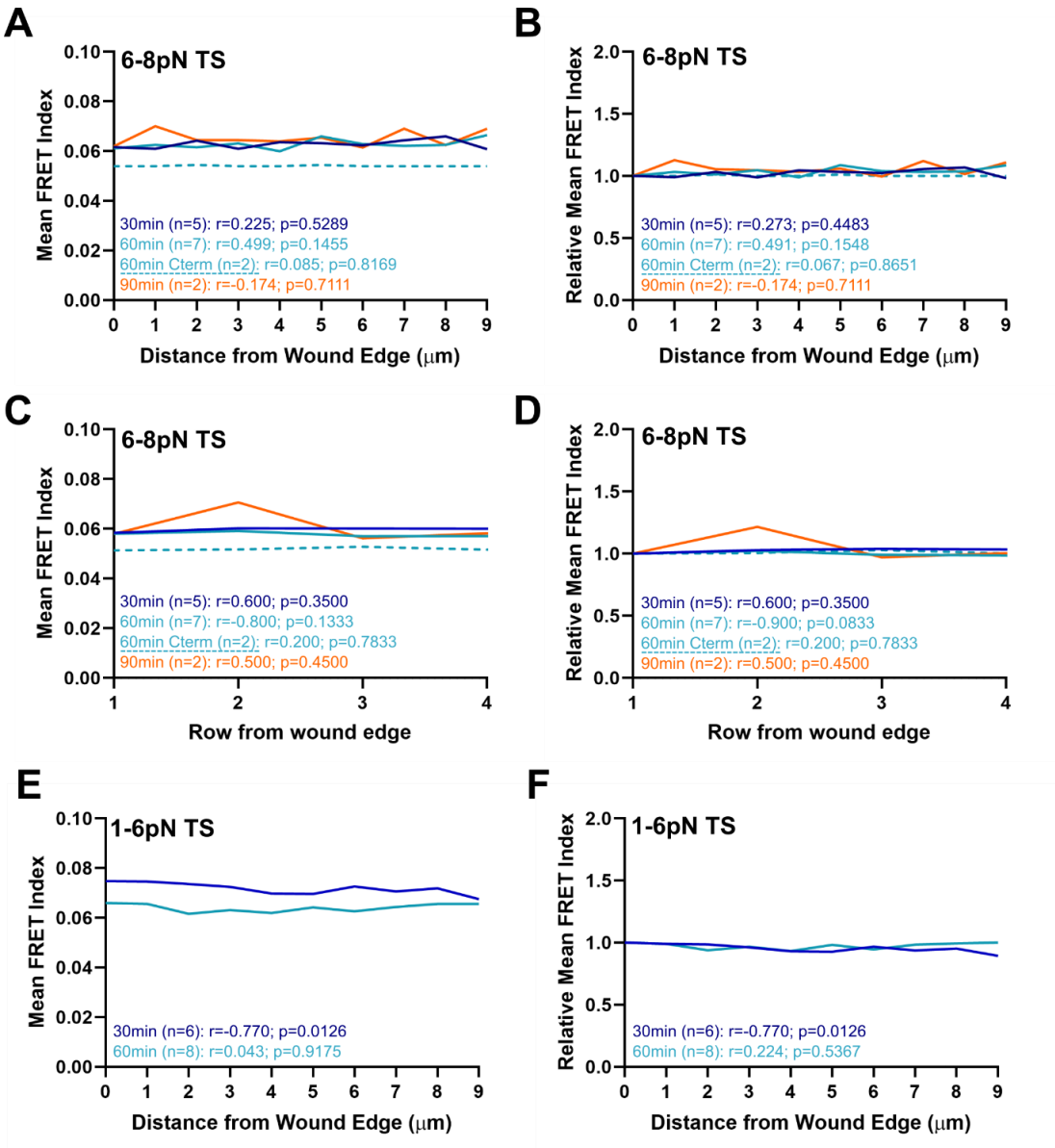

Figure 4.7: FRET index measurements in wounded wing discs.

A) Mean FRET index vs distance from the wound edge for wounded wing discs with the 6-8pN TS or 6-8pN Cterm TS. B) Relative Mean FRET index vs distance from the wound edge for wounded wing discs with the 6-8pN TS or 6-8pN Cterm TS. C) Mean FRET index vs cell row from the wound edge for wounded wing discs with the 6-8pN TS or 6-8pN Cterm TS. D) Relative Mean FRET index vs cell row from the wound edge for wounded wing disc with the 6-8pN TS or 6-8pN Cterm TS. E) Mean FRET index vs distance from the wound edge for wounded wing discs with the 1-6pN TS. B) Relative Mean FRET index vs distance from the wound edge for wounded wing discs with the 1-6pN TS. Error bars are not shown for clarity, and r values are

Spearman's rank-order correlation coefficients with respective p values. For A-D, dark blue lines, light blue lines, and orange lines correspond to 30 min, 60 min and 90 min post-wound timepoints, respectively. The coloured dotted line corresponds to the relevant Cterm control.

4.5 Discussion

In this chapter, I utilised two FRET-based Talin-TS to quantify forces exerted at the basal surface of the wing disc 30 min, 60 min and 90 min post-wounding. I hypothesised that the mean FRET index would increase as the distance from the wound edge increased, as Talin-TS at the wound edge would be stretched under tension exerted by the lateral cables, reducing the proportion of Talin-TS undergoing FRET. However, using a 6-8pN TS, I observed no significant correlation between mean FRET index and distance away from the wound edge when plotted as a scatterplot and calculated in distance bands or rows of segmented puncta. Since the FRET index values are roughly uniform across regions around the wound, this suggests that TS is in similar conformations regardless of position relative to the wound. Using a 1-6pN TS, there was a significant negative correlation between mean FRET index and distance from the wound edge 30 min post-wounding. This suggests that TS close to the wound are undergoing more FRET than TS away from the wound.

Despite these results, it is not possible to draw any biological or physical conclusions without adequate tension-insensitive Cterm TS controls for each TS, respectively. Previous E-cad TS studies in the wing disc indicated that experimental procedures can directly influence FRET index changes rather than solely reflecting mechanical tensions [244]. In this study, external mechanical perturbation using a tissue stretcher altered the FRET index of both tension-insensitive controls and tension-sensitive constructs to the same extent [244]. This demonstrates that FRET index values may be influenced by biological or sensor-specific factors rather than a mechanical process. To clarify if the TS constructs are sensing forces in the absence of wounding, these experiments should be repeated in unwounded discs.

Speculating on possible scenarios in these wounded wing discs, if Cterm controls exhibited higher FRET index values than my current results with tension-sensitive TS, this would suggest that a majority of TS in wounded wing discs are under tension, regardless of their relative position to the wound. Perhaps Talin is under tension over the whole basal surface. Klapholz et al. describe a mechanism in which Talin can adopt multiple orientations in a tissue-dependent manner and show that Talin is oriented parallel to the membrane in pupal wings, whereas Talin is oriented perpendicular to the membrane in muscles [246]. From my data, it is impossible to know in which direction the forces are experienced by Talin. I assume that forces due to the lateral cables would act perpendicularly to the basal cell membrane, forcing Talin to orient perpendicularly to the basal cell membrane, but, perhaps under unwounded circumstances, Talin could be under constant tension due to the basal actomyosin network. Although less dense than the apical actomyosin network, basal actomyosin has been suggested as the driver of wing disc curvature [149]. Talin is likely to be oriented in a mixture of perpendicular and parallel orientations (Chapter 3.5) [246]. Due to its multiple actin-binding sites, Talin can bind actin in a variety of ways [247]. Even if forces were detected by the Talin-TS, it would be challenging to identify the direction and source of the responsible actomyosin structures.

If tension-insensitive Cterm controls displayed similar mean FRET indices, this would suggest that the tension-sensitive TS are not experiencing any forces. Alternatively, forces could be bypassing the mechanosensitive linker in the inserted TS constructs entirely, resulting in similar FRET index values between tension and tension-insensitive controls, as the mechanosensitive linker in the tension-sensitive constructs is not engaged. The mechanosensitive linker is positioned between the head and tail domains of Talin, whereas actin binds to actin-binding sites in the tail domain. The tail domain contains 13 force-sensitive rod domains that unfold subject to forces between 5 – 20pN. Therefore, perhaps these rod domains must be fully unfolded before the mechanosensitive linker, positioned after the tail domain, can be extended. Furthermore, Owen et al, propose that under load,

monomeric Talin only binds transiently to actin and Talin dimerisation is required for stable actin binding [248]. Therefore, any forces exerted by actin would be shared between two Talin molecules, requiring even higher forces to induce stretches in the linker molecules. If the TS are not being stretched, this would explain why there is no difference in FRET index relative to the wound edge.

Even if a suitable TS was chosen that only unfolded due to the forces exerted by lateral cables, I could also be masking any subtle changes in FRET index by my binning techniques, as averaging values across spatial bands or cell rows may smooth out small but biologically relevant differences between individual Talin puncta or within puncta. Notably, the scatterplots of raw FRET index against distance from the wound edge revealed no clear trends, suggesting either that no strong pattern exists or that variability at the level of individual puncta is too high to detect changes in FRET index (Figure 4.5). This raises the possibility that only a small subset of Talin molecules may be under tension at any given time, making it challenging to detect differences using cell row binning. Variations in Talin activation may be highly varied within each pixel. Pixel size itself acts as an inherent binning of the FRET signal, and if the pixel size is too large relative to the subcellular features being measured, spatial averaging within each pixel could obscure fine-scale variations in FRET index, such as localised tension near lateral cables.

Lemke et al. found that less than 15% of Talin molecules were mechanically engaged in the pupal wing [225]. In the case of the lateral cables, only a small proportion of Talin would be engaged with the cables, and they would likely be located at the cell membrane closest to the wound. Therefore, smaller areas around the wound could be imaged. A higher magnification x100 objective could be used; however, its shorter working distance would likely be unfeasible due to the doming of the wing disc. During analysis, smaller band widths could be used, for example, 0.2 µm or 0.5 µm thick bands, or segmented puncta could be subdivided.

A limitation of sensitised emission is that it is impossible to determine whether a zero-signal pixel is zero because there are no talin tension sensors present, or if there is a fully stretched tension sensor undergoing 100% FRET efficiency. Additionally, Eder et al. found that the FRET index highly correlates with signal intensity (acceptor excitation) for *Drosophila* embryo border cells ($r = 0.43$) and wing imaginal discs ($r = 0.38$) [244]. Quantification of Talin intensity (Chapter 3) suggests that 30 min and 60 min post-wounding, Talin density increases with distance away from the wound.

Instead, Fluorescence Lifetime Imaging Microscopy can be used as the average lifetime of fluorophores within a pixel is measured. Lifetimes are measured using a pulsed femtosecond excitation laser and single-photon counting detectors. If FRET occurs, the donor fluorophore lifetime becomes shorter as energy is transferred to the acceptor fluorophore. Therefore, if there are no constructs present in a pixel, no lifetimes would be measured, whereas if constructs were undergoing no FRET, a longer lifetime would be measured instead. There are many other advantages to FLIM over intensity-based measurements as lifetimes are independent from fluorophore intensity, which is affected by many confounding factors such as laser power fluctuations, temperature, humidity, sample mounting and levels of fluorophore expression.

I performed pilot experiments using the FLIM-FRET module on a Leica STELLARIS 8 DIVE equipped with a pulsed tunable multiphoton (2P) laser (Coherent). These experiments revealed significant limitations with using a 2P laser in contrast to the pulsed visible (1P) laser utilised in the original study by Lemke et al. Firstly, imaging donor-only controls with 2P excitation before photobleaching was not feasible due to the longer acquisition times required to collect enough photon counts for lifetime measurement in FLIM. FLIM requires acquisition times in the order of minutes which would increase phototoxicity and photobleaching. A previous study has found that photobleaching is increased for some fluorophores under 2P excitation compared to 1P excitation [221,249]. Secondly, there is no characterisation of YPet excitation and emission spectra under 2P excitation, which are often more unpredictable than their 1P behaviour [221,222,249]. Lastly, some

common fluorophores used with 1P excitation are only weakly excited by 2P wavelengths provided by titanium-sapphire lasers.

These experiments are particularly laborious, not only in the number of controls required before any FRET measurements can be made but also in the need to wound and successfully locate the wound on the basal surface of the wing disc. As the wing disc is curved and continues to curl after it is removed from the larva, the curled edges can obstruct the basal surface of the wound. This renders any analysis of cells around the wound impossible. Additionally, the wound is difficult to locate basally as the signal from Talin puncta remains as autofluorescence even after wounding, albeit weaker. As a result, multiple wounds were discarded as wounds were not successfully located or were obscured.

These experiments highlight the complexities in using FRET-based TS in tissues as previously raised by Eder et al [244]. Specifically, the need for controls to ascertain the proper engagement of TS constructs. Imaging is further complicated by wounding and the previously discussed technical challenges of imaging the wing disc. The priority for future experiments is collecting tension-insensitive TS control images in wounded wing discs for both the 1 – 6pN and 6 – 8pN TS constructs. Then, the 9 – 11pN TS and its respective tension-insensitive Cterm TS control. These results could then be validated by a second method to measure FRET, such as acceptor photobleaching. Overall, due to the numerous controls required (three additional fly lines must be imaged per TS), poor imaging of the curved basal surface of wounded wing discs and lack of knowledge of the precise orientation of TS constructs in the tissue, FRET-based TS are impractical for measuring meaningful forces in wounded wing discs.

The role of Talin in lateral cable function or formation remains unknown. To identify if Talin is indispensable for cable formation and to identify other regulators of cable formation, I performed knockdown experiments on Talin and other proteins in wounded wing discs in the next chapter.

5 Investigating the molecular mechanisms behind lateral cable formation and regulation

5.1 Introduction

Currently, little is known about lateral actomyosin structures driving wound healing [117]. In morphogenesis, lateral actomyosin structures and their regulators are beginning to be identified. For instance, *Drosophila* leg disc folding is driven by apoptotic nuclei tethered to the apical surface by a lateral actomyosin cable and anchored to the basal surface by F-actin [123]. Targeting the basal F-actin anchor, RNAi knockdowns of Talin or nucleus tethering protein Klarsicht reduced or prevented folding [123]. In the absence of identifiable molecular regulators, biophysical tools can be used to manipulate myosin activity in specific locations in tissues. For example, optogenetic recruitment of RhoGEF2 to the lateral sides of the wing disc induces significant fold formation [250].

While many molecular players behind the assembly of the purse string and migratory protrusions during wound healing have been identified, including actin nucleators, anchoring proteins, GTPases and their upstream regulators [76,87,88,97,103,104,114,128,226,251–255], the precise spatiotemporal patterns of their recruitment during wound healing remain poorly understood. Partly due to the overlapping roles of these proteins within wound healing and other essential cellular processes such as division, morphogenesis or mechanosensing. This redundancy ensures that wound healing is highly robust, with cells coopting any available components to efficiently close wounds when normal healing pathways are perturbed [74,103,107]. For example, in *Drosophila* embryo wounds, the removal of branched actomyosin by Arp2/3 RNAi is compensated by linear actin filaments assembling in a chiral swirling mechanism to drive cells forward to close the wound [103]. As such, performing knockdown screens to systematically eliminate candidate proteins is challenging.

To understand the function of the lateral actomyosin cables in *Drosophila* wing disc wounds, I sought to perturb or abolish their assembly using genetic loss-of-function perturbations of possible regulatory proteins. If these cables are responsible for wound edge cell shortening, I hypothesised that their absence would decrease or prevent cell shortening and delay wound closure. I used GFP-tagged myosin II regulatory light chain (*spaghetti squash* or *sqh* in *Drosophila*) as a marker for lateral cables (LCs) and successful wound formation throughout these experiments. To assess the impact of any perturbations on wound healing, I quantified apical wound area, apical purse string (PS) myosin intensity, apical indentation, percentage of apical junctions at the wound, number of LCs and mean LC myosin intensity (see Chapter 2.8 for further detail). Due to imaging limitations discussed in Chapter 3.3, I relied on apical indentation as the primary indicator of cell shortening. It is important to consider that apical and basal surfaces indent at different times (Chapter 3.1), suggesting potentially distinct behaviours of LCs at these locations, which will be further discussed in Chapter 6.

In this chapter, I aim to identify key LC molecular regulators by performing loss-of-function experiments using temperature-sensitive alleles or RNAi knockdowns. I first focus on actomyosin regulators localised to possible LC anchor regions at cell adhesions at the apical or basal surfaces, then, key regulators of myosin phosphorylation, and lastly, I start to screen further upstream regulators of myosin, specifically RhoGEFs and GAPs.

5.2 Endocytosis is required for purse string assembly but not apical indentation or lateral cable formation.

Previous imaging by Dr Rob Tetley suggested that LCs are continuous with the apical purse string (Chapter 3.1). I sought to remove or reduce the strength of the apical purse string without affecting the LCs to determine whether the assembly and function of the LCs are dependent on the apical purse string. I hypothesised that if the LCs assembled with the apical purse

string, abolishing the apical purse string would also eliminate the LCs, resulting in negligible or reduced apical indentation at the wound.

To test this hypothesis, I utilised a temperature-sensitive shibire mutant (shi^{TS}) to disrupt the apical purse string formation. This mutant was utilised by Matsubayashi et al. to abolish the purse string in *Drosophila* embryo wounds [97]. Shibire encodes *Drosophila* Dynamin, a key endocytic regulator which has additional important roles in cytokinesis and cell migration [256,257]. Under shi^{TS}, the actin cable, actin protrusions and actin puncta at wounds were blocked, demonstrating that dynamin is essential for wound edge actin assembly. This assembly is disrupted as AJ remodelling via endocytosis is impaired. AJ remodelling is necessary to clear components such as E-cadherin and recruit key actin regulators, for example, Diaphanous, for purse string assembly [97]. As endocytosis is required for a vast majority of cellular processes, Shibire mutations are fatal. However, shi^{TS} flies show normal behaviour and viability at permissive temperatures whilst inducing paralysis and arrested endocytosis above 26°C. To ensure full expression of the mutant, I incubated dissected wing discs at 31°C for at least 60 min before imaging on the microscope stage (Chapter 2.6.1). After wounding, I imaged control and shi^{TS} for 60 min as we observed consistent apical indentation and LC formation within this period (Chapter 3.1).

These experiments revealed that shi^{TS} apical wound area closure is 2.5 times slower than the control, with mean closure rates of 0.017 ±0.005% min^{-1} and 0.007 ±0.003% min^{-1} for control and shi^{TS} wounds, respectively (Figure 5.1.B-B'). Notably, shi^{TS} wounds appeared to stall closure between 15-50 min (Figure 5.1.B). Apical purse string myosin intensity is reduced by approximately 40% in shi^{TS} wounds, with purse string myosin intensity plateaus reaching 2.212 ±0.428 fold and 1.323 ±0.141 fold for control and shi^{TS} wounds, respectively (Figure 5.1.C-C'). The effect of shi^{TS} on purse string formation is much weaker than previously found in the *Drosophila* embryo; nevertheless, closure is dramatically delayed [97]. The rate of apical indentation is not significantly different (p=0.222, Mann-Whitney) between the control and shi^{TS} wounds (Figure 5.1.D-D'). The mean apical indentation rates are 0.058 ±0.011μm min^{-1} and 0.069 ±0.030μm min^{-1} for control and

shi^{TS} wounds, respectively (Figure 5.1.D'). Additionally, the percentage of apical junctions throughout healing does not significantly differ (0.5476, Mann-Whitney) between control and shi^{TS} wounds (Figure 5.1.E-E'). As the number of cables between timepoints is paired data, Wilcoxon matched-pairs signed rank tests are used to calculate p-values. However, the smallest p-value that can be obtained for n=5 is 0.0625. Together with visual data inspection, I conclude that there is a significant difference between the number of cables between 9 min and 60 min in control wounds, which are 3 ±2 and 7 ±2 cables, respectively (Figure 5.1.F). At 60 min, there is a significant difference in the number of cables between control and shi^{TS} wounds (p=0.0079, Mann-Whitney), which are 7 ±2 cables and 3 ±1 cables, respectively. There are no significant differences in the mean LC myosin intensity per wound or per cable between timepoints or conditions.

These results demonstrate that shi^{TS} cause a decrease in the number of LCs as well as a 40% decrease in apical purse string myosin intensity. Despite this, the rate of apical indentation is not affected. This suggests that a minimum number of cables may be sufficient to drive apical indentation, even in shi^{TS} wounds. While overall myosin recruitment to LCs is not significantly altered, fewer LCs are formed. This indicates that the total myosin pool remains available, but its organisation and stabilisation may require endocytic processes. It is unclear how the wound edge cells conserve their volume if they shorten without decreasing the wound area. Further experiments are needed to quantify how the wound edge cells change shape under PS myosin reduction, for example, imaging wounds with dextran to visualise the basal surface.

The specific role of LCs remains unclear as both apical and lateral structures coexist in this experiment, and I cannot decouple their roles in the context of wound closure and apical indentation. In the next section, I continue to search for key regulators of the LCs. I examine integrin adhesion complexes as possible basal anchor points for the LCs.

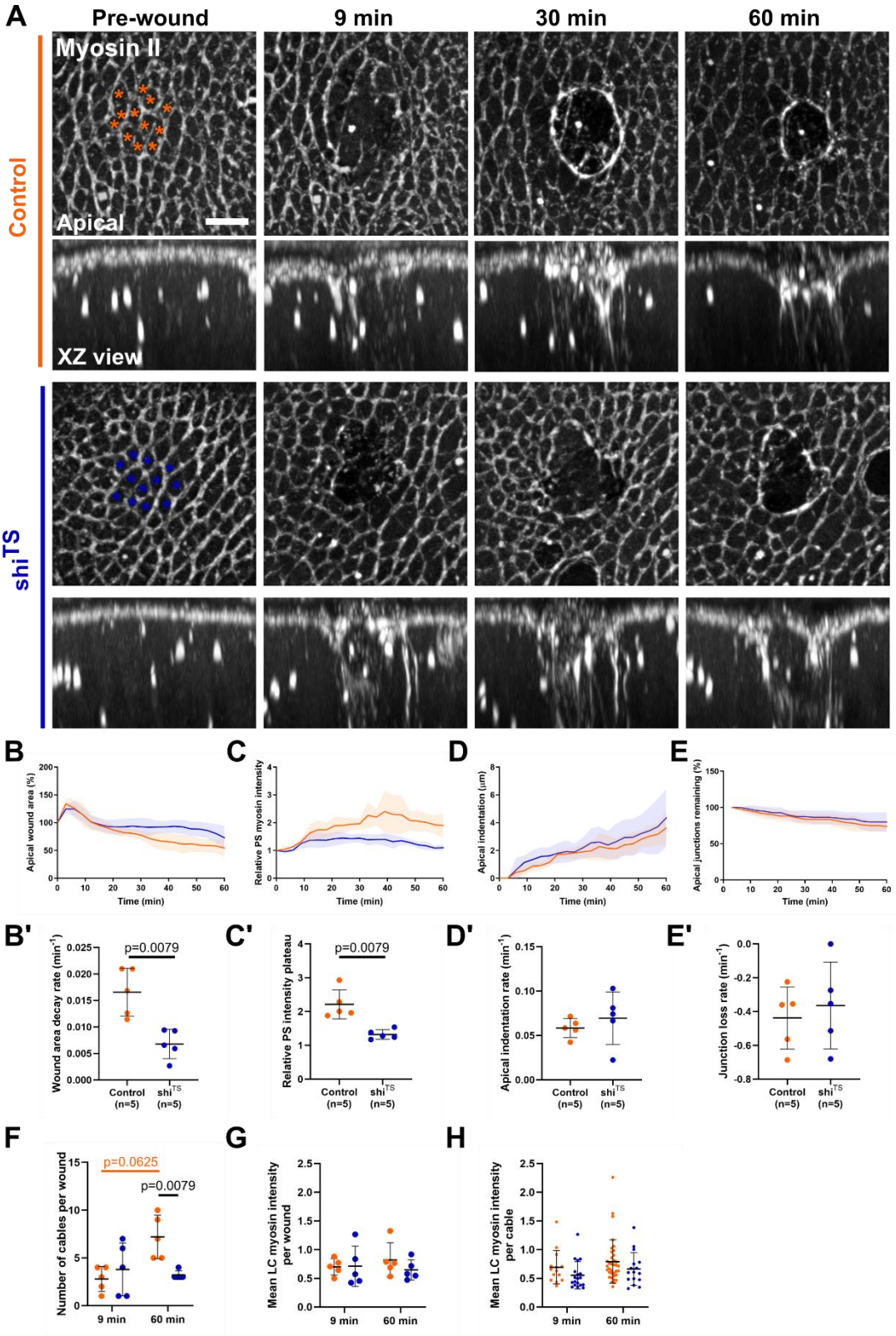

Figure 5.1: Endocytosis is required for purse string assembly but not apical indentation or lateral cable formation.

A) Timelapse images for wounded control discs with genotype yw/Y; sqhGFP/+; (orange, n=5) and wounded shi^{TS} discs with genotype shi^{TS}/Y;

sqhGFP/+; (blue, n=5) expressing myosin-GFP. Asterisks indicate dead cells. B) Apical wound area. B') Wound area decay rates from fitting one-phase decay curves of individual replicates from B. C) Relative PS myosin intensity. C') Relative PS myosin intensity plateaus from fitting one phase associations of individual replicates from C. D) Apical indentation. D') Apical indentation rates from fitting straight lines of individual replicates from D. E) Apical junctions remaining as cells are eliminated from the wound edge. E') Junction lost rates from fitting straight lines of individual replicates from E. F) Number of cables per wound 10 min and 60 min after wounding. G) Mean lateral cable (LC) myosin intensity per wound 10 min and 60 min after wounding. H) Mean LC myosin intensity per cable 10 min and 60 min after wounding. For B-E, shaded areas represent the SD. For B'-E' and F-H, plots show individual data points with the mean (horizontal line), SD (bars) and p values from two-tailed Mann Whitney tests. For F, p-values between different timepoints were calculated using Wilcoxon matched-pairs signed rank tests. Scale bars are 5 μm.

5.3 Talin knockdown does not affect apical wound healing

Talin (*rhea* in *Drosophila*) is essential for clustering integrin into focal adhesion-like basal structures or integrin adhesion complexes (IACs) in *Drosophila* wing discs [199]. It is a mechanosensitive protein that links the actin cytoskeleton to integrin and its extracellular ligands, playing key roles in both 'inside-out' and 'outside-in' signalling [197]. Disruption of Talin function has significant consequences; for example, blocking Talin autoinhibition in mouse embryonic fibroblasts results in a loss of interdependence between actin organisation and focal adhesion organisation [258] while in *Drosophila* embryos, dorsal closure is delayed [259]. Conversely, loss of Talin can cause wing blisters in adult *Drosophila* and lead to failures in embryonic processes like germband retraction and muscle attachment [29,197,199].

Previous imaging showed that LCs colocalise with Talin at IACs (Chapter 3.4). Additionally, the knockdown of Talin in the *Drosophila* leg disc prevented deformation of the apical surface [123]. In wounded Drosophila embryonic

epidermis, Talin has been shown to accumulate at the wound edge [129,260], though this has not been observed in wing disc cells, which are 4-5 times taller than squamous embryonic epidermic cells (data not shown).

I hypothesised that Talin knockdown in *Drosophila* wing disc wound healing would prevent basal cable anchoring and apical indentation, resulting in delayed wound healing. To test this, I used two RNAi lines from the Bloomington *Drosophila* Stock Center (BDSC 33913) and the Vienna *Drosophila* Resource Center (VDRC 40399), which were both previously reported to give similar results in the *Drosophila* leg disc [123]. Expression of RNAi was driven specifically in the pouch region using *nubbin-GAL4* (*nubGAL4*).

I confirmed knockdown efficacy through immunostaining (Figure 5.2.A). Despite careful mounting of wing discs with coverslips, most Talin RNAi discs adopted a curved position. Talin levels are greatly reduced in the pouch regions of both RNAi lines compared to controls (Figure 5.2.A). Side views reveal that most remaining Talin belonged to overlying peripodial cells. I also imaged live myosin-GFP discs as PFA fixation alters wing disc morphology (Figure 5.2.B). Control and VDRC-derived Talin RNAi wing discs appeared similar, whereas Bloomington-derived Talin RNAi wing discs exhibited a distinctive bowl-shaped morphology. This bowl-shaped morphology may reflect an intermediate morphology before the extra fold formation observed in integrin mutant discs (Chapter 6). Adult wings from both Talin RNAi lines display defects, including smaller crumpled wings with blisters (Figure 5.2.C). Furthermore, many flies from both Talin RNAi lines failed to emerge from pupation.

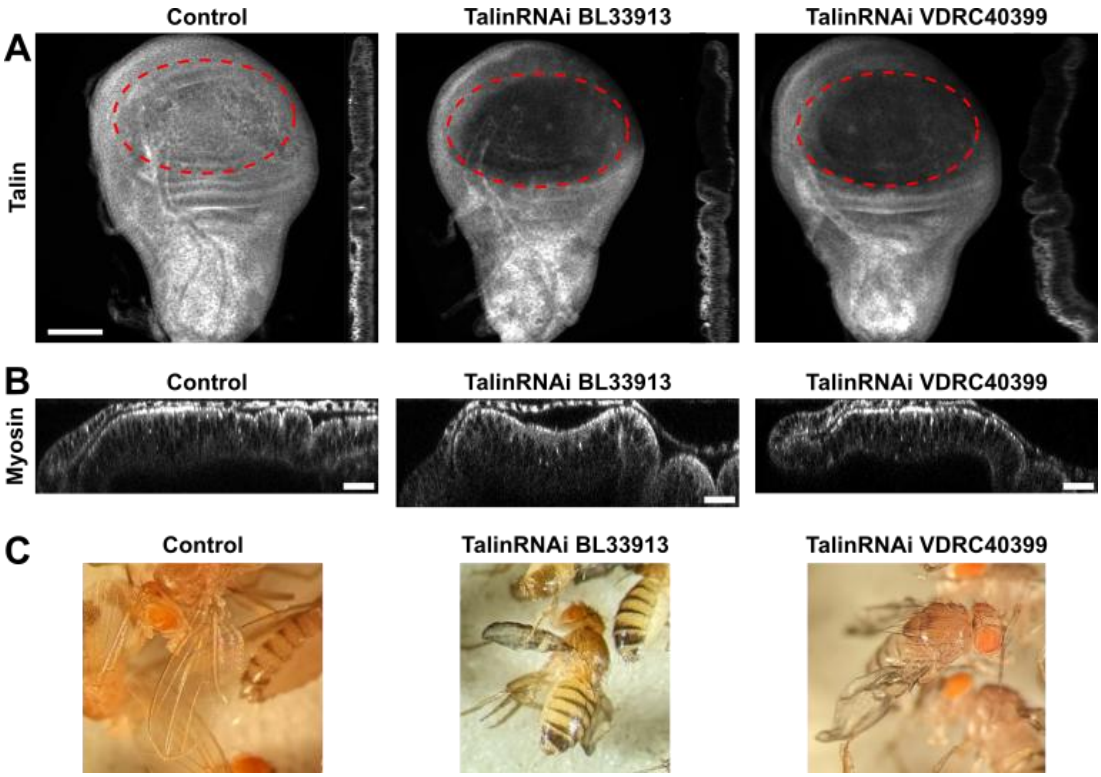

Figure 5.2: Reduced Talin levels lead to bowl-shaped wing discs and defective adult wing phenotypes.

Images from flies of genotypes *sqhAX3/Y; sqhGFP, nubGAL4/+; +/+* (control), *sqhAX3/Y; sqhGFP, nubGAL4/+; UAS-Talin RNAi/+* (BL33913) and *sqhAX3/Y; sqhGFP, nubGAL4/+; UAS-rheaRNAi/+* (VDRC 40399). A) Immunostaining of Talin. The red dotted line indicates the pouch region. Side views are slices taken from the centre of the wing disc. Scale bars are 50 µm. B) Side views through the centre of live images of myosin-GFP tagged wing discs. Scale bars are 20 µm. C) Adult wing phenotypes.

For wounding experiments, I imaged wounds for 120 min as basal deformation typically begins after 60 min (Chapter 3). To reduce phototoxicity, I decreased the imaging frequency from every 3 min to every 5 min.

There are no significant differences in apical wound area, apical PS myosin intensity, apical indentation, apical junctions, number of LCs, or mean LC myosin intensity per wound between control and either Talin RNAi line wounds (Figure 5.3.A-G). There are no significant differences in the wound

healing behaviours between the VDRC 40399 Talin RNAi line and the BDSC 33913 Talin RNAi line.

There is a significant increase in the mean LC myosin intensity per cable from 0.673 ±0.259 at 10 min to 0.823 ±0.283 at 60 min in control wounds, while there is no such significant increase in either Talin RNAi line wounds (Figure 5.3.H, p=0.0010, Mann-Whitney). At 60 min, there is a significant decrease in mean LC myosin intensity per cable between the control at 0.823 ±0.283 and both Talin RNAi lines at 0.701 ±0.237 for VDRC 40399 and 0.673 ±0.209 for BDSC 33913 (Figure 5.3.H). While Talin may not be required for the initial wound response, its absence could affect myosin stability at later timepoints. IACs or focal adhesions typically remodel in the timescales of minutes to hours [261,262]. This may lead to the delayed difference in myosin intensity in the LCs. Overall, both RNAi lines showed similar wound healing behaviour, and these results indicate that Talin knockdown has little effect on wound healing.

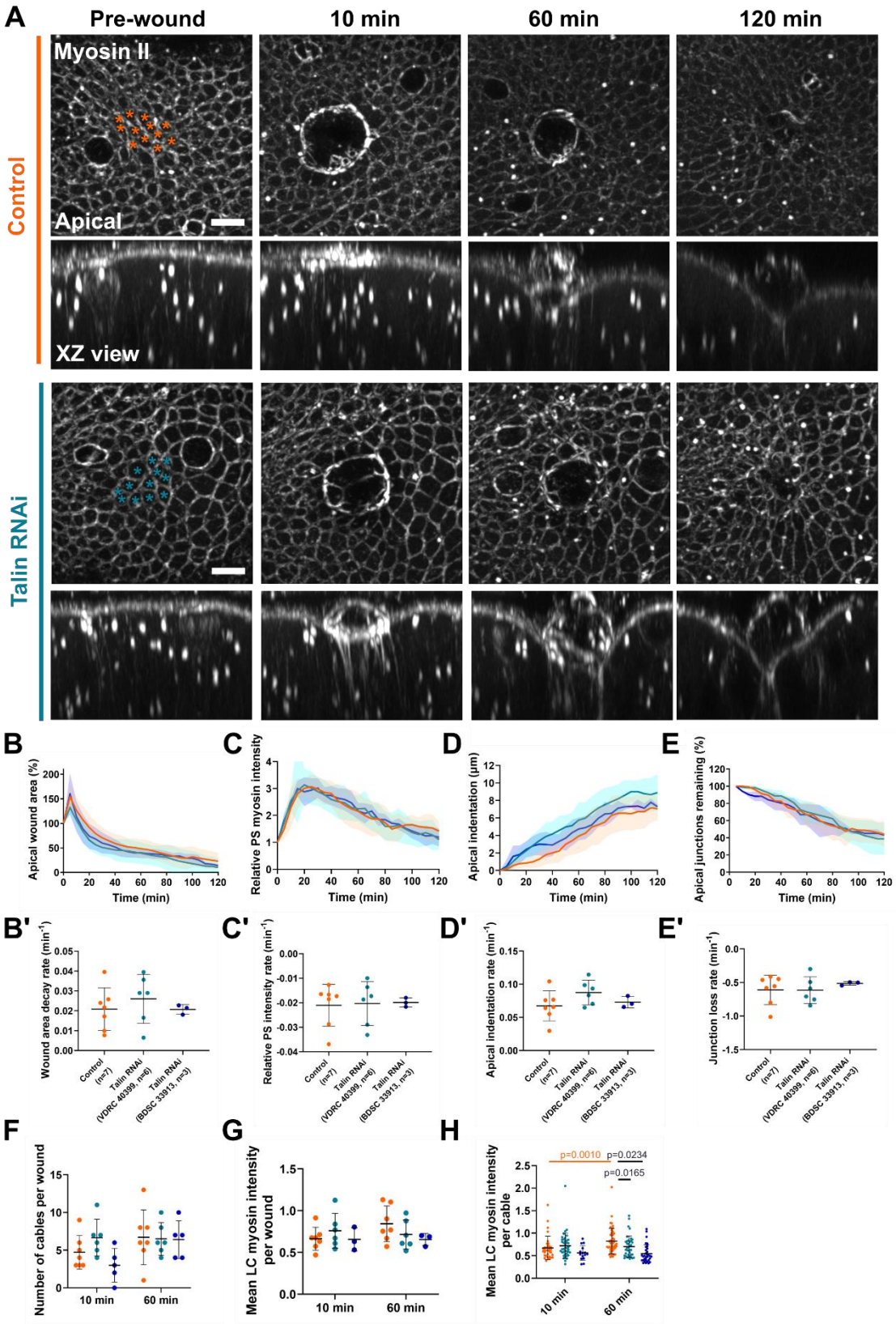

Figure 5.3: Talin knockdown does not affect wound healing at the apical surface.

A) Timelapse images for wounded control discs with genotype *sqhAX3/Y; sqhGFP, nubGAL4/+;* (orange, n=7) and wounded Talin RNAi discs with genotype *sqhAX3/Y; sqhGFP, nubGAL4/+; UAS-rheaRNAi/+* (blue) expressing myosin-GFP. Asterisks indicate dead cells. Light blue indicates discs from crosses with the VDRC 40399 Talin RNAi line (n=6) and dark blue indicates discs from crosses with the BDSC 33913 Talin RNAi line (n=3). B) Apical wound area. B') Wound area decay rates from fitting one-phase decay curves of individual replicates from B. C) Relative PS myosin intensity. C') Relative PS myosin intensity reduction rates from fitting straight lines of individual replicates from C. D) Apical indentation. D') Apical indentation rates from fitting straight lines of individual replicates from D. E) Apical junctions remaining as cells are eliminated from the wound edge. E') Junction lost rates from fitting straight lines of individual replicates from E. F) Number of cables per wound 10 min and 60 min after wounding. G) Mean lateral cable (LC) myosin intensity per wound 10 min and 60 min after wounding. H) Mean LC myosin intensity per cable 10 min and 60 min after wounding. For B-E, shaded areas represent the SD. For B'-E' and F-H, plots show individual data points with the mean (horizontal line), SD (bars), and p-values from two-tailed Mann-Whitney tests. For F, p-values between different timepoints were calculated using Wilcoxon matched-pairs signed rank tests. Scale bars are 5 μm.

5.4 Perturbing myosin phosphorylation

Myosin regulation involves a complex interconnected network of proteins. For myosin to power the contraction of actin filaments, it must be phosphorylated by kinases such as myosin light chain kinase (MLCK) and Rho-associated protein kinase (ROCK or Rok in *Drosophila*) [17–19]. Perturbing these kinases has widespread effects on myosin regulation. Conversely, myosin light chain phosphatase inactivates myosin by dephosphorylating its regulatory light chain.

Previous experiments in the lab have shown that Rok knockdown via Rok-RNAi reduces phosphorylated myosin, and as a result, tension in the wing disc causes wounds to close faster than normal [104]. Although initially

closing wounds slower than wildtype wounds, presumably due to a weaker purse string, these softer cells can more easily intercalate away from the wound edge in later stages of healing. In contrast, expressing an RNAi targeting the myosin binding subunit (Mbs) of myosin phosphatase increases phosphorylated myosin and tension in the wing disc, causing wounds to fail closure [104]. These stiffer cells cannot intercalate, causing wound edge cells to become jammed at the wound edge, preventing wound closure entirely.

I used the same RNAi lines for Rok RNAi and Mbs RNAi and assessed the efficacy of the knockdowns by observing adult wing phenotypes. Rok RNAi wings exhibit phenotypes ranging in severity from blistered, crumpled wings to small notch defects, whilst Mbs RNAi wings exhibit eclosion defects with small black wings (Figure 5.4). Additional live imaging of myosin-GFP tagged wing discs will be conducted to examine the homeostatic tissue morphology under both Rok RNAi and Mbs RNAi conditions.

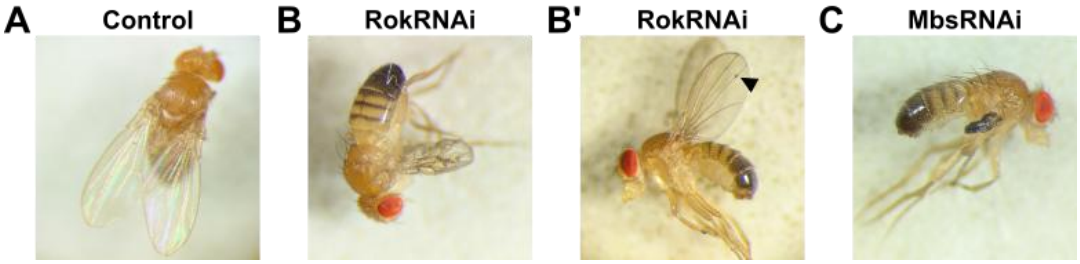

Figure 5.4: Disrupting myosin activity leads to wing defects in adult male *Drosophila*.
A) *sqhAX3/Y; sqhGFP, nubGAL4/+* (control). B) *sqhAX3/Y; sqhGFP, nubGAL4/UAS-RokRNAi.* B') *sqhAX3/Y; sqhGFP, nubGAL4/UAS-RokRNAi.* The black arrow indicates a notch defect. C) *sqhAX3/Y; sqhGFP, nubGAL4/UAS-MbsRNAi* adults.

There are no significant differences in apical wound area, apical indentation, apical junctions, number of LCs, or mean LC myosin intensity per wound between control and Rok RNAi wounds (Figure 5.5.A-G). There is a significant difference in the apical PS intensity. PS intensity peaks at 2.2-fold the resting apical myosin intensity, whereas control wounds peak at 3-fold (Figure 5.5.C). This aligns with decreased myosin activity caused by Rok

RNAi, which leads to reduced myosin phosphorylation. Consequently, there is a lower relative fold change upon wounding as there is weaker overall myosin activity. Relative PS intensity decreases at almost half the rate of control discs at -0.0211 ±0.0211% min^{-1} and -0.0123 ±0.0067% min^{-1} (Figure 5.5.C', p=0.0175, Mann-Whitney). There is also a significant difference in mean LC myosin intensity per cable at 60 min between control and Rok RNAi wounds at 0.823 ±0.283 and 0.693 ±0.296, respectively (Figure 5.5.H, p=0.0198, Man-Whitney). Overall, these results indicate that Rok knockdown has little effect on wound healing.

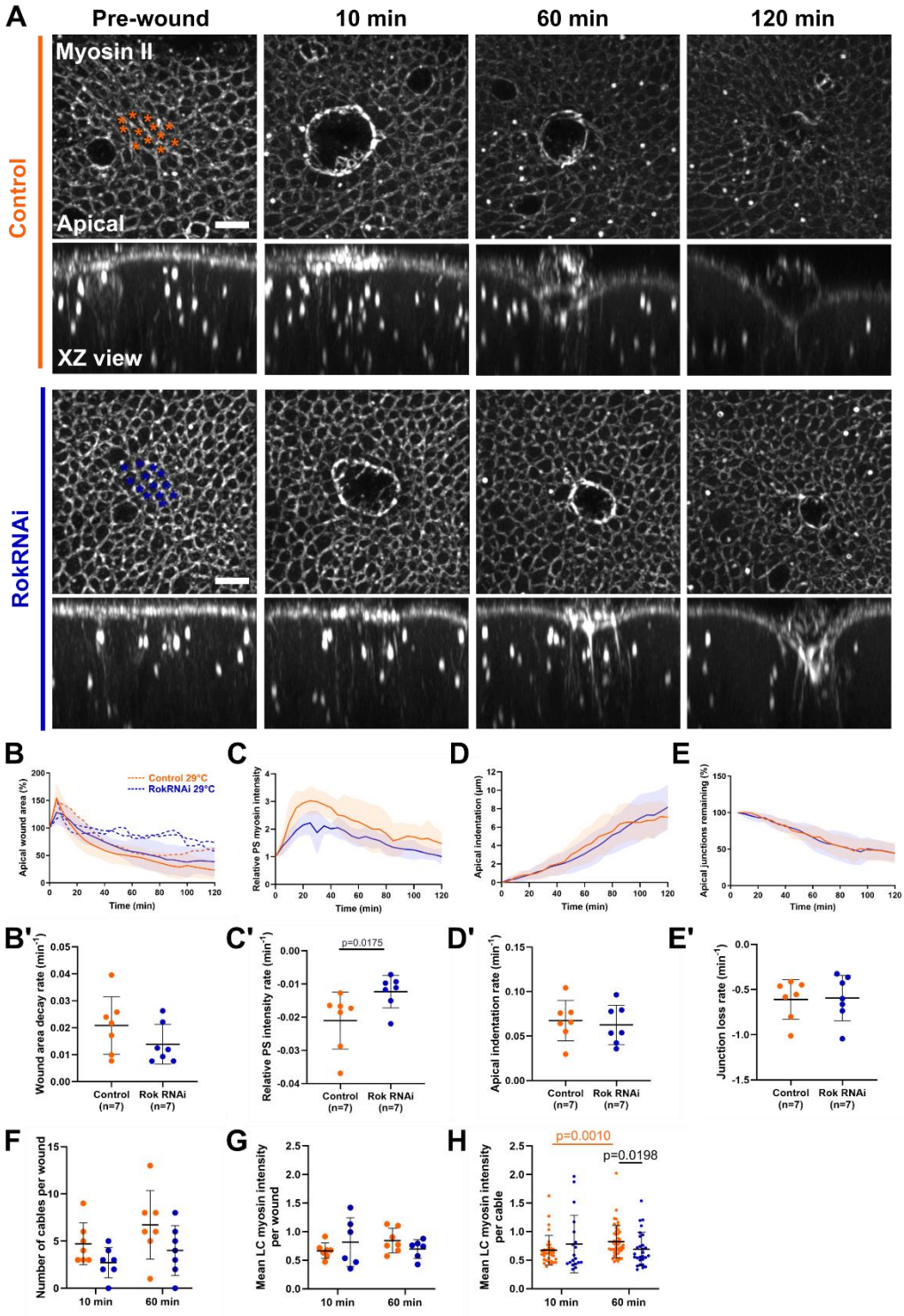

Figure 5.5: *UAS-RokRNAi* driven by *nubGAL4* has a negligible wound healing phenotype.

A) Timelapse images for wounded control discs with genotype *sqhAX3/Y; sqhGFP, nubGAL4/+;* (orange, n=7) and wounded Rok RNAi discs with genotype *sqhAX3/Y; sqhGFP, nubGAL4/UAS-RokRNAi* (blue, n=7) expressing myosin-GFP. Asterisks indicate dead cells. B) Apical wound area.

Dotted lines indicate individual replicates of wounded control (orange, n=1) and RokRNAi (blue, n=2) discs raised at 29°C. B') Wound area decay rates from fitting one-phase decay curves of individual replicates from B. C) Relative PS myosin intensity. C') Relative PS myosin intensity reduction rates from fitting straight lines of individual replicates from C. D) Apical indentation. D') Apical indentation rates from fitting straight lines of individual replicates from D. E) Apical junctions remaining as cells are eliminated from the wound edge. E') Junction lost rates from fitting straight lines of individual replicates from E. F) Number of cables per wound 10 min and 60 min after wounding. G) Mean lateral cable (LC) myosin intensity per wound 10 min and 60 min after wounding. H) Mean LC myosin intensity per cable 10 min and 60 min after wounding. For B-E, shaded areas represent the SD. For B'-E' and F-H, plots show individual data points with the mean (horizontal line), SD (bars), and p values from two-tailed Mann-Whitney tests. For F, p-values between different timepoints were calculated using Wilcoxon matched-pairs signed rank tests. Scale bars are 5 μm.

This was surprising as previous experiments using the same RNAi line in the lab show a significant acceleration in wound healing. However, an important difference is that the *rotund-GAL4* (*rn-GAL4*) was used, which has a slightly different expression pattern and strength from *nubGAL4* [263]. Theory has shown that the precise level of Rok activity and Myosin II contractile strength is important for closure dynamics [104]. To attempt to increase the expression of RNAi in these crosses, I tested raising the larvae at an elevated temperature of 29°C [264]. This appeared to yield even further delayed wound healing in both the control and the Rok RNAi wounds (Figure 5.6.A, dotted lines). Therefore, these wounds are not further analysed.

Even before wounding, there are noticeable differences in myosin localisation in the apical cortex of MbsRNAi discs compared to controls (Figure 5.6.A). MbsRNAi discs exhibit a thicker belt of myosin around the apical cortex. There are significant differences in almost all wound healing measures in Mbs RNAi wounds compared to control wounds (Figure 5.6). Wound area decay rate is almost 2.7 times slower at 0.0209 ±0.0107% min^{-1} and 0.0078 ±0.0054% $min^{-1,}$ respectively (p=0.0041, Mann-Whitney). At

120min, Mbs RNAi wounds are about 65% closed, whereas control wounds are about 25% closed (Figure 5.6.B). PS intensity peaks in Mbs RNAi wounds at 2-fold the resting apical myosin intensity, whereas control wounds peak at 3-fold. (Figure 5.6.C). This aligns with the increased myosin activity caused by Mbs RNAi due to reduced myosin phosphatase function. Consequently, there is a lower relative fold change upon wounding, as there is already excessive myosin. Relative PS intensity decreases at a rate that is almost 4 times slower than control discs at -0.0211 ±0.0086% min^{-1} and -0.0054 ±0.0067% min^{-1} (Figure 5.6.C', p=0.0006, Mann-Whitney). This suggests that the myosin turnover at the PS is reduced in Mbs RNAi wounds compared to control wounds. This may be because myosin is in a more stable, "activated" form for longer periods when myosin phosphatase is inhibited, contributing to persistent contractility and longer-lived myosin filaments.

The apical indentation rate in Mbs RNAi wounds is 3.2 times slower than in control wounds at 0.0208 ±0.0204μm min^{-1} and 0.0674 ±0.0227μm $min^{-1,}$ respectively (Figure 5.6.D-D', p=0.0041, Mann-Whitney). The percentage of apical junctions in Mbs RNAi wounds decreases at less than half the rate observed in control wounds at -0.3644 ±0.1275% min^{-1} and -0.6103 ±0.2195% $min^{-1,}$ respectively (Figure 5.6.E-E', p=0.0111, Mann-Whitney).

The number of cables per wound does not significantly differ; however, the mean LC myosin intensity per wound in Mbs RNAi wounds decreases significantly from 0.740 ±0.106 at 10min to 0.572 ±0.125 at 60min (Figure 5.6.G, p=0.0350, Mann-Whitney). At 60 min this intensity is also significantly lower than in control wounds, where the intensity per wound remains higher at 0.844 ±0.213 (Figure 5.6.G, p=0.0111, Mann-Whitney).

This trend is even more pronounced in the mean LC intensity per cable, which declines from 0.743 ±0.272 at 10min to 0.576 ±0.255 at 60min in Mbs RNAi wounds (Figure 5.6.H, p=0.0004, Mann-Whitney). Similarly, at 60min, the mean LC myosin intensity per cable in control wounds remains significantly higher at 0.823 ±0.283 (Figure 5.6.G, p<0.0001, Mann-Whitney).

When the purse string forms and begins contracting, the apical surface at the wound edge experiences multiple forces. These are: inward forces pulling toward the wound, outward forces due to membrane and cortical tension resisting deformation, and downward forces toward the basal surface, driven by volume conservation, which may be facilitated by the LCs as the apical surface constricts.

Previous junctional recoil experiments show that under Mbs RNAi, the effective tension is similar in the unwounded tissue and at the wound (Figure 5h in [104]). Therefore, in Mbs RNAi wounds, the contraction of the purse string is balanced by the cortical tension of the tissue. This is maintained over the course of the experiment with little myosin turnover. As the wound does not decrease in size, there is no violation of volume conservation, so no cell shape changes, such as indentation, are needed. This reduces the need for the LC, particularly at later timepoints, as the wound is still almost 100% open. Furthermore, since the total myosin pool is depleted, less new myosin is recruited into filaments as existing LCs are too stable. As such, these persistent myosin-GFP molecules may be photobleached, leading to a reduction in mean LC myosin intensity.

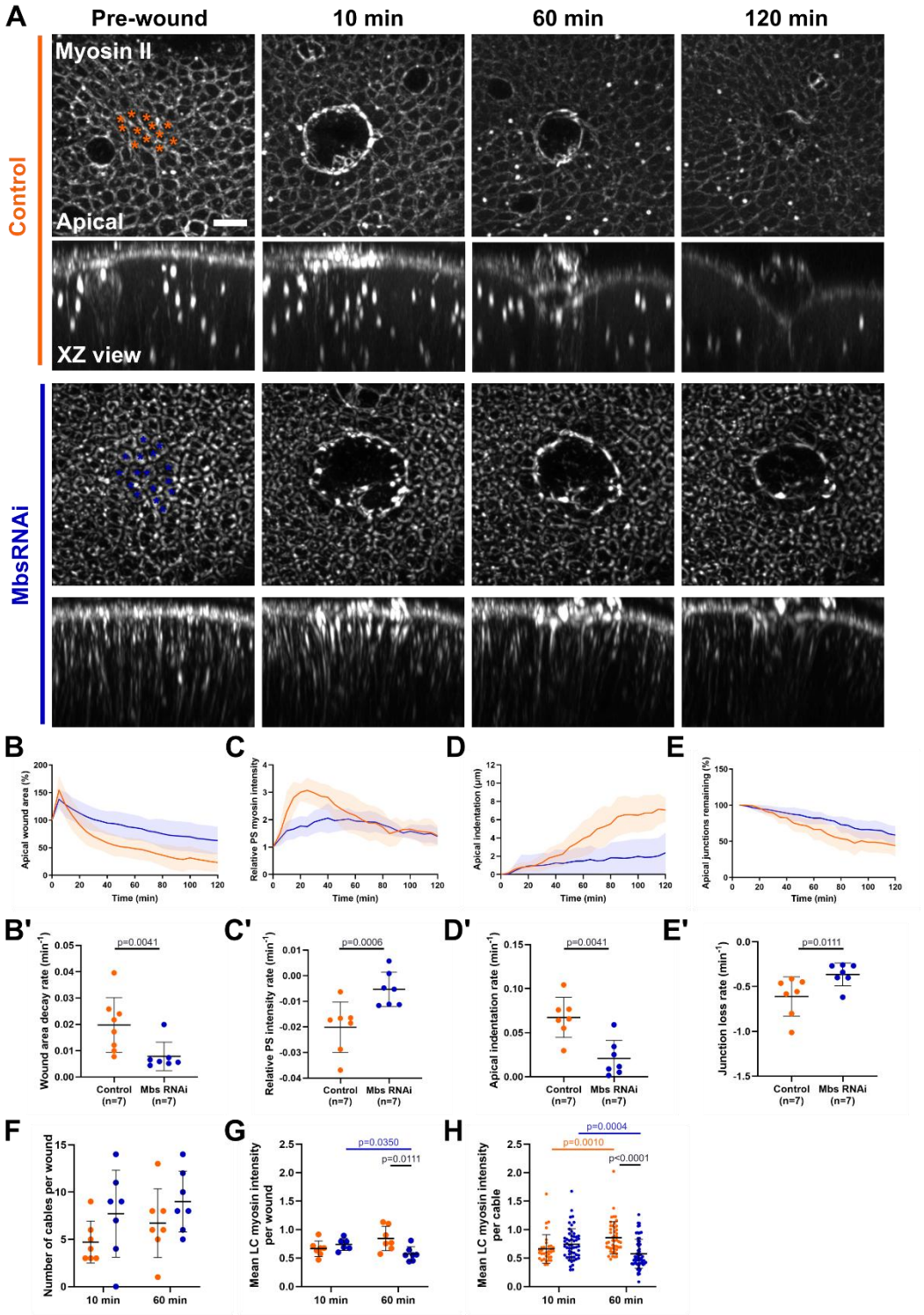

Figure 5.6: Myosin activation delays wound healing.

A) Timelapse images for wounded control discs with genotype *sqhAX3/Y; sqhGFP, nubGAL4/+;* (orange, n=7) and wounded Rok RNAi discs with genotype *sqhAX3/Y; sqhGFP, nubGAL4/UAS-MbsRNAi* (blue, n=7) expressing myosin-GFP. Asterisks indicate dead cells. B) Apical wound area. B') Wound area decay rates from fitting one-phase decay curves of individual

replicates from B. C) Relative PS myosin intensity. C') Relative PS myosin intensity reduction rates from fitting straight lines of individual replicates from C. D) Apical indentation. D') Apical indentation rates from fitting straight lines of individual replicates from D. E) Apical junctions remaining as cells are eliminated from the wound edge. E') Junction lost rates from fitting straight lines of individual replicates from E. F) Number of cables per wound 10 min and 60 min after wounding. G) Mean lateral cable (LC) myosin intensity per wound 10 min and 60 min after wounding. H) Mean LC myosin intensity per cable 10 min and 60 min after wounding. For B-E, shaded areas represent the SD. For B'-E' and F-H, plots show individual data points with the mean (horizontal line), SD (bars), and p-values from two-tailed Mann-Whitney tests. For F, p-values between different timepoints were calculated using Wilcoxon matched-pairs signed rank tests. Scale bars are 5 μm.

5.5 Screening for molecular regulators of lateral cable formation

Upstream of Rok are a family of small G proteins called RhoGTPases, which play key roles in actin cytoskeleton assembly as well as cell polarity, gene transcription, cell cycle progression, microtubule dynamics, vesicular transport and enzymatic activities [22,23]. The three most common members of the RhoGTPase family are Cdc42, Rac1 and RhoA (or Rho1 in *Drosophila*), and all three are required for wound repair [265,266].

Two protein families control Rho GTPase signalling: Rho guanine exchange factors (RhoGEFs) and Rho GTPase activating proteins (RhoGAPs). RhoGEFs inactivate the GTPase activity of Rho, converting Rho into its active form. In turn, Rho activates Rok to increase phosphorylated myosin. On the other hand, RhoGAPs promote the GTPase activity of Rho, converting Rho into an inactive form that decreases Rok activity and phosphorylated myosin. In *Drosophila*, there are 48 RhoGEFs and GAPs that have different spatiotemporal roles in development and homeostasis [267]. Similarly to their downstream targets, RhoGEFs form distinct dynamic spatial and temporal patterns surrounding the wound [107].

RhoGEFs activate Rok which would increase myosin phosphorylation and contractile activity. Although RhoGAPs would deactivate Rok, they may act on other pathways that may result in myosin phosphorylation. I started to perform a screen targeting RhoGEFs and RhoGAPs. To direct my screening, I prioritised RhoGEFS and RhoGAPs with any lateral or basal localisations identified by Bellaiche et al. Bellaiche et al. performed a systematic analysis on the location of all 48 RhoGEFs and RhoGAPs during epithelial cell division [267]. Additionally, I plan to include other actomyosin regulators of interest, as summarised in Table 8.

The screen comprises the following steps:

1. Characterising the localisation of candidates in the wing disc.
2. Characterising the localisation of candidates in wounded wing discs.
3. Wounding RNAi mutant wing discs of candidate proteins and quantifying wound healing behaviour. RNAi expression is driven in the wing disc using *nubGAL4* in *sqhAX3; sqhGFP, nubGAL4;* flies.

Protein	**Type**	**Location**
Cdep	RhoGEF	Interphase (notum): Basolateral, lateral TCJ. Cell division (notum): Underneath the contractile ring, underneath midbody. Interphase (FE): Apicomedial cortex, basolateral, TCJ. Cell division (FE): underneath the contractile ring, underneath midbody along whole apical-basal axis. [267]
RhoGEF2	RhoGEF	Interphase (notum): Apical junctions, apicomedial. Interphase (FE): Apicomedial cortex. [250,267]
Ziz	RhoGEF	Interphase (notum): Apical junctions. Interphase (FE): Apical junctions and lateral. [267]
Pbl	RhoGEF	Interphase (notum): Nuclear. Interphase (FE): Nuclear, Apical junctions. [267] Wound healing. [107]
rtGEF	RhoGEF	Interphase (notum): Apical junctions, apicomedial (weak). Interphase (FE): Basal (planar polarized), apicomedial cortex (low levels). Cell division (FE): Daughter cell interface (below the ring and basal level). [267]

Cysts (CG10188)	RhoGEF	Interphase (notum): Apical junctions. Cell division (notum): Rim of contractile ring, new AJ. Interphase (FE): Apical junctions. Cell division (FE): Rim of contractile ring, new AJ. [267]
RhoGAP19D	RhoGAP	Interphase (notum): Apical junctions, lateral domain. Interphase (FE): Apical junctions, lateral domain. Cell division (FE): Cytoplasmic accumulation. [267]
RhoGAP5A	RhoGAP	Interphase (notum): apical TCJ, elongating apical junctions. Interphase (FE): Basal (planar polarized). [267]
RhoGAP15B	RhoGAP	Interphase (notum): Apical junctions. Interphase (FE): Apicomedial cortex, basal puncta. Cell division (FE): Enrichment near midbody, apical daughter cell interface, basal puncta disappear during mitosis. [267]
RhoGAP1A	RhoGAP	Interphase (notum): Apical junctions, apical medial. Cell division (notum): Basolateral metaphase cortex, mitotic spindle, underneath contractile ring, rim of contractile ring. Interphase (FE): Apical junctions, apicomedial cortex. Cell division (FE): Basolateral metaphase cortex, midbody and apical daughter cell interface. [267]
cdGAPr	RhoGAP	Interphase (notum): Apical junctions, medio-apicomedial cortex, nucleus. Cell division (notum): Basolateral metaphase cortex, contractile ring, rim of contractile ring, daughter cell interface. Interphase (FE): Apicomedial cortex. Cell division (FE): Basolateral metaphase cortex, contractile ring, apical daughter cell interface. [267]
Fascin	Actin crosslinker	Apical and lateral cytoplasm in the wing disc and basal cytoplasm after wounding (Dr Rob Tetley, unpublished).
Warts	Basal spot junctions	Basal surface adjacent to IACs and colocalised with E-cad, α-catenin and Jub [198].
Rac1	GTPase	Basal actin cortex assembly dependent on integrin-binding to extracellular collagen [139].

Table 5.1: Table of candidate proteins for lateral cable assembly screen. Abbreviations: follicular epithelium (FE) and tricellular junctions (TCJ).

As many of the proposed candidate proteins have not been characterised in the wing disc, I first imaged endogenously expressed GFP-tagged candidates in unwounded wing discs (Figure 5.6.A-D). CellMask was used to mark cell membranes so that apical, lateral and basal domains of each cell could be identified as well as any dividing cells.

5.5.1 Localisation of RhoGEFs and RhoGAPs in the wing disc

Example localisation snapshot images of Cdep-GFP are shown in Figure 5.7. Figure 5.7.A shows that Cdep localises dispersedly in the apical cytoplasm. 4.2μm beneath the apical surface, Cdep localises to bright puncta close to the lateral membranes (Figure 5.7.B). Particularly bright puncta belong to long cables running parallel to the lateral membranes, as highlighted in Figure 5.7.C-D. These cables presumably belong to filamentous structures basal to the cytokinetic ring in dividing cells, as described in the *Drosophila* embryo notum by Pietro et al. [267]. To confirm this, timelapse imaging of cell division in unwounded discs will be performed in future experiments. These snapshots show that Cdep is expressed in the wing disc during normal homeostasis.

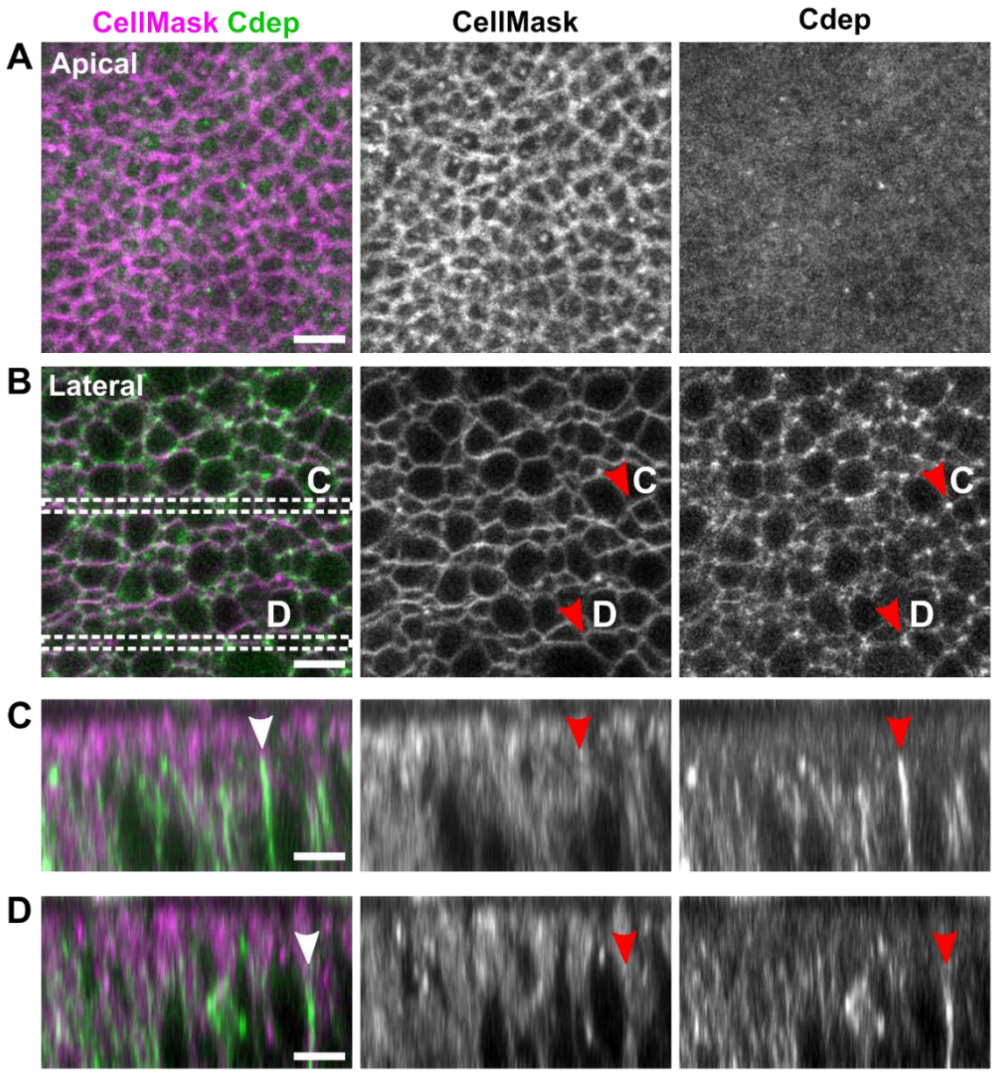

Figure 5.7: Cdep-GFP is localised to cable-like structures in the lateral domain of wing disc cells.

A) The apical surface of an early third instar wing disc pouch region with cell membranes marked with CellMask Deep Red and endogenously expressed Cdep-GFP. B) The lateral surface of the wing disc, 4.2µm beneath the apical surface. White and red annotations indicate examples of cable-like structures. Cross-sectional (XZ) views are shown respectively in C-D. C-D) Max projections of white dotted boxes in B. Scale bars are 5 µm.

5.5.2 Characterising CellMask as a wound marker

Next, I sought to wound GFP-tagged candidate protein discs. To verify successful wound formation, a clear marker is required. Actomyosin-related markers are typically used as they mark apical cell borders and the formation

of the purse string. Alternatively, AJ markers such as E-cadherin also mark clear cell boundaries at a suitable plane of ablation and it is possible to observe cell recoil immediately after ablation, an indication of successful cutting of cell membranes due to release of tension. To quickly stain cell membranes in live discs without needing to cross flies, I used Cell Mask Deep Red.

No published studies in the wing disc have used a cell membrane marker during wound healing. To determine the correct z plane for ablation and key indicators of successful wound formation, I performed timelapse imaging of wounded sqhAX3; sqhGFP; wing discs with CellMask. For successful ablations, I wound at the plane just below the AJs, which is approximately 1µm basal to the strongest myosin signal (blue dotted line, Figure 5.8.A). Comparing the location of the myosin and cell membrane signals in Figure 5.8.A I found that this plane was approximately 3µm below the initial apical CellMask signal. For future imaging with the RhoGEFs and RhoGAPs, I will use this measurement to make wounds in the absence of myosin-GFP.

After ablation, successful wounds recoil towards surrounding cells and form a purse string within 5 min after wounding (Figure 5.8.A). Unlike myosin, utrophin, or E-cad, which are mainly cleared from the wound gap, CellMask accumulates in the wound after initial photobleaching. Successful wounds are obvious 21 min after wounding, where CellMask signal fills the wound and wound edge cells elongate towards the wound gap (Figure 5.8.B). In unsuccessful wounds, after 11 min, instead of the signal becoming more diffuse as seen in later timepoints in Figure 5.6.B, the cell membrane signal is restored to its appearance before wounding. Here, the cells have only been bleached, and the CellMask diffuses back into the healthy cells.

There are limitations to characterising the appearance of GFP-tagged candidate proteins during wound healing. As discussed in Chapter 3, fast imaging of the wound's lateral domain is limited by the wing disc's fluorescence attenuation. Adding the CellMask channel further reduces temporal resolution, preventing capture of the first 3 minutes of wound

healing, when LC formation is likely initiated.

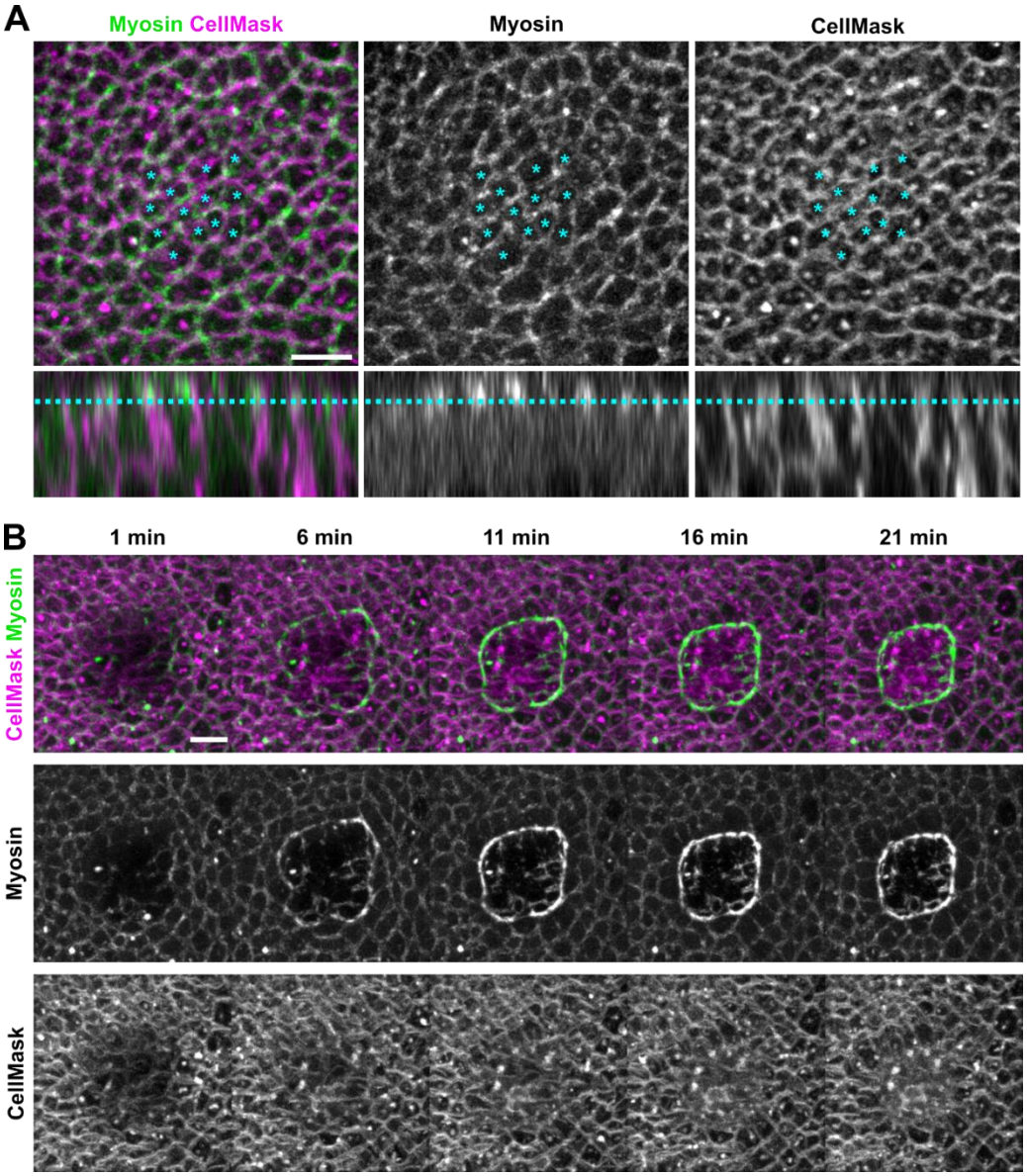

Figure 5.8: CellMask as a wound marker.

A) Maximum projections of the apical surface of an unwounded sqhAX3; sqhGFP; wing disc expressing myosin-GFP and cell membrane stained with CellMask Deep Red. Blue asterisks denote future ablated cells, and the blue dotted line denotes the plane of ablation. B) Timelapse imaging of the wing disc in A. Scale bars are 5μm.

5.5.3 Cdep knockdown does not affect apical wound healing

RNAi knockdown experiments are effective in determining whether a candidate protein is involved in wound healing. In the last part of the screen, I hypothesised that if a candidate protein involved in LC formation is knocked down by RNAi, the LCs should fail to form, and apical indentation will be decreased or negligible. I started this RNAi screen with Cdep RNAi wounds due to its role in forming LC-like structures in cell division.

There are no significant differences in apical wound area, apical PS intensity, apical indentation, apical junctions, number of LCs, or mean LC myosin intensity per wound between control and Cdep RNAi wounds (Figure 5.9.A-G). There is a significant decrease in mean LC myosin intensity per cable from 0.823 ±0.283 in control wounds to 0.615 ±0.111 in Cdep RNAi wounds at 60 min(Figure 5.9.H, p=0.0008, Man-Whitney). Overall, these experiments demonstrate that RhoGEF Cdep is unlikely to be responsible for LC formation.

To accelerate the screening process in future experiments, I aim to image only the first 20 min of wound healing. The experiments shown in Chapter 3 and earlier in this chapter show that LCs are distinguishable as early as 10 min after wounding.

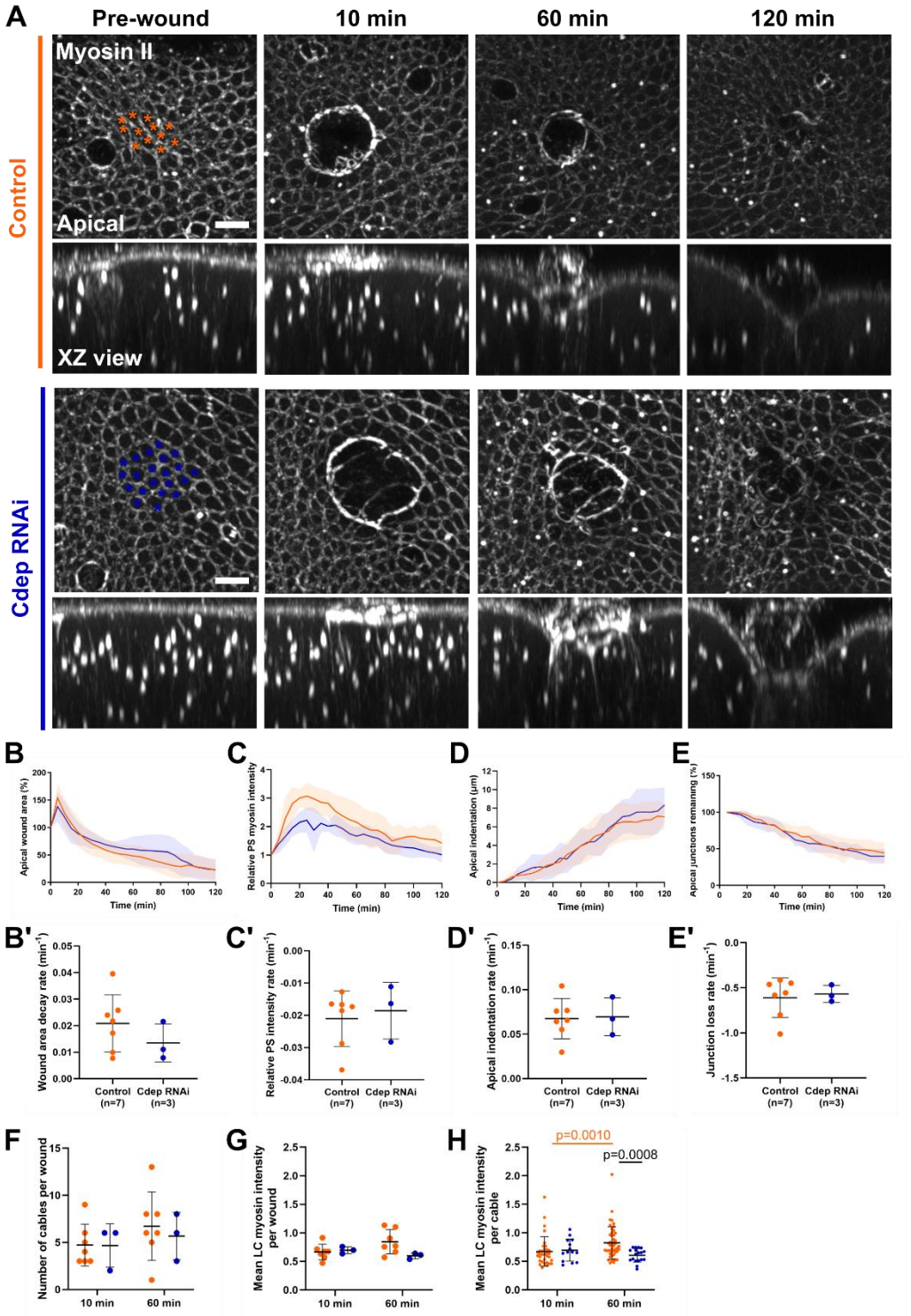

Figure 5.9: Cdep knockdown does not affect apical wound healing A) Timelapse images for wounded control disc with genotype *sqhAX3/Y; sqhGFP, nubGAL4/+;* (orange, n=7) and wounded Cdep RNAi discs with genotype *sqhAX3/Y; sqhGFP, nubGAL4/+; UAS-CdepRNAi/+* (blue, n=3) expressing myosin-GFP. Asterisks indicate dead cells. B) Apical wound area. B') Wound area decay rates from fitting one-phase decay curves of individual

replicates from B. C) Relative PS myosin intensity. C') Relative PS myosin intensity reduction rates from fitting straight lines of individual replicates from C. D) Apical indentation. D') Apical indentation rates from fitting straight lines of individual replicates from D. E) Apical junctions remaining as cells are eliminated from the wound edge. E') Junction lost rates from fitting straight lines of individual replicates from E. F) Number of cables per wound 10 min and 60 min after wounding. G) Mean lateral cable (LC) myosin intensity per wound 10 min and 60 min after wounding. H) Mean LC myosin intensity per cable 10 min and 60 min after wounding. For B-E, shaded areas represent the SD. For B'-E' and F-H, plots show individual data points with the mean (horizontal line), SD (bars), and p-values from two-tailed Mann-Whitney tests. For F, p-values between different timepoints were calculated using Wilcoxon matched-pairs signed rank tests. Scale bars are 5μm.

5.6 Discussion

In this chapter, I perturbed various actomyosin-associated regulators across apical, lateral and basal regions to assess their impact on wound healing and specifically LC formation. These experiments demonstrate the robustness of wound healing in the wing disc and suggest that LCs are also highly robust.

I developed quantitative methods to compare LC formation despite the challenges posed by the 3D nature of the cables, multiple timepoints and difficulties in imaging their full apicobasal length. Since capturing complete apicobasal cables without damaging the tissue or oversaturating the apical surface through high excitation laser powers was not possible, I focused on the apical surface of the wound where the LC signal was least attenuated. Even then, it is difficult to threshold or segment the cables in 3D and requires significant manual input due to the presence of debris signal and remnant cytokinetic myosin, mentioned briefly in Chapter 3. To address this, I used maximum projections of manually selected XZ or YZ slice ranges for each cable, which helped resolve curved cables. While this underestimates LC myosin intensity and requires subjective judgement of cable location, it adequately represents intensity changes in these structures. This approach

balances technical limitations with the need for reproducible quantitative comparison.

Reducing the PS by 40% led to a 2.5-fold slower wound closure rate; however, apical indentation and LC formation still occur, albeit with fewer cables. For these 10-15 cell wounds, approximately 3 cables at 60 min may be enough to successfully coordinate apical indentation. Alternatively, even with 40% less myosin, the contraction of the apical purse string may be enough to cause apical indentation. Furthermore, the effects of shi^{TS} are likely widespread, affecting more than just AJ remodelling in the context of wound healing. Additional shibire genotypes are required to validate these results, for example, shi^{ts1}, which may cause even further reduction of the PS.

The number of cables appeared to significantly increase in temperature-shifted control wounds with genotype *yw*/Y; *sqhGFP*/+; (Figure 5.1.H), but this increase was not seen in *sqhAX3*/Y; *sqhGFP, nubGAL4/+;* wounds at room temperature (Figures 5.3.H, 5.5.H, 5.6.H, 5.9.H). In hemizygous males with the genotype yw/Y; *sqhGFP*/+, *sqhGFP* is expressed alongside wildtype *sqh;* therefore, only a fraction of myosin will be tagged with GFP. In contrast, hemizygous males with the genotype *sqhAX3*/Y; *sqhGFP*, *nubGAL4/+;* will have all myosin molecules tagged with GFP due to the *sqhAX3* null background. Therefore, in experiments with *yw*/Y; *sqhGFP*/+, the quantified myosin intensity may not be representative of the real myosin quantity, as there may be untagged myosin molecules present. Additionally, the abnormally high temperature of these experiments may affect myosin behaviour. Alternatively, Rab5DN could be used to abolish endocytosis without the need for temperature shifting. Matsubayashi et al. found that Rab5DN blocked the formation of actin cables similarly to shi^{2} [97].

Talin knockdown surprisingly did not affect LC formation or wound healing in general. Both lines used in this chapter were used in previous studies in the *Drosophila* pupal wing and larval leg disc. In the pupal wing, Talin was knocked down by 50% [225] and was greatly reduced in the leg disc, although some small spots were still visible in confocal images [123]. From

wing disc immunostaining, there is a substantial Talin reduction in both lines (Figure 5.2.A). This shows that there are differences in knockdown expression depending on tissue type.

Perhaps, similarly to the function of Talin in the pupal wing disc, only a small number of Talin molecules are required for actin binding in the larval wing disc. Even if the knockdown is highly expressed, some wildtype Talin will remain. At developing muscle attachments in the *Drosophila* pupal wing, less than 15% of Talin molecules experience forces higher than 6-8pN [225]. Here, a large pool of Talin prevents mechanical failure by sharing the mechanical load. A sudden increase in tissue tension can be rapidly buffered by engaging additional molecules already present. This provides mechanical robustness to the tissue, which is critical for survival and development. Furthermore, Talin has multiple actin-binding sites, which may offer functional robustness when normal Talin function is perturbed [247]. It would be interesting to wound discs with Talin or Integrin overexpression since these mutations have also been shown to cause developmental defects.

Talin RNAi disc morphology is perturbed, displaying a bowl shape. This shape may arise from the shortening of cells, reminiscent of integrin mutants [146]. Talin knockdown reduces actin linkage to integrin adhesions. Kroeger et al. show that Talin knockdown altered basal actomyosin organisation from doughnut-like with filamentous projections to astral formations distributed across a larger basal-medial cell surface area [198]. Similar myosin patterns were observed in the previously discussed Talin immunostainings (Appendix 8.1). Perhaps these basal actomyosin rearrangements alter basal and basolateral tissue tension, affecting overall tissue and cell shape. Future experiments will image the complete tissue height to include the basal surface in the analysis.

In the same study, Kroeger et al. identified structures termed basal spot junctions, AJ-like complexes adjacent to IACs on the basal surface of wing disc cells [198]. These structures are distributed between basal actomyosin bundles and contain many of the same proteins as AJs. They may be more suitable candidates for basal anchor points of the LCs as they are localised

at the edge of basal cell boundaries and, therefore, closer to the wound edge. Due to their similarity to AJs, they may also undergo endocytosis-mediated remodelling during wound healing. It is currently unknown how the basal junctions of wing disc cells rearrange in response to wound healing. This may explain why shi^{TS} wounds form fewer cables, as myosin turnover may also be reduced at these basal spot junctions. The study faces similar limitations to those discussed in this chapter; it is currently not possible to selectively modulate basal spot junctions without affecting apical pools of constituent proteins.

Vinculin is another component of the IAC that binds to actin and Talin. However, previous literature reports that loss of vinculin produces minor phenotypes, if any, whereas vinculin overactivation can cause lethality [268,269]. Previous experiments by Dr Rob Tetley showed negligible effects of *rotundGAL4-driven* vinc-RNAi on wound closure (unpublished). Maartens et al. found that the constitutively open form of vinculin (vinc-CO) bypasses integrins to form cytoplasmic aggregates with closed talin, which do not link the membrane to actin [268]. It would be interesting to observe the effects of vinc-CO in the wing disc. Additionally, when the actin-binding domain of Talin was deleted, vinculin binding compensates [246]. Therefore, wound healing may be delayed by the co-expression of both Talin and Vinculin RNAi.

Although *nubGAL4*-driven Rok RNAi wounds showed no significant defects, changes in apical purse-string myosin intensity suggest some RNAi expression. A possible compensatory mechanism involves Drak, which may help maintain actomyosin activity in the absence of Rok [270]. Previous experiments in the lab showed accelerated wound healing using the same Rok RNAi lines driven by rotund-GAL4 [104]. Both *nubbin* (*nub*) and *rotund* (*rn*) are expressed in the wing disc pouch, but the *rn* expressing domain is several cell rows smaller than the *nub*-expressing region [165,263]. Despite its small expression domain, *rnGAL4* may lead to stronger RNAi effects than *nubGAL4* due to higher GAL4 expression levels per cell, more efficient RNAi processing, or tissue-specific sensitivity to the specific driver and RNAi line.

However, *rnGAL4* was not used in this experiment due to previous inconsistencies in wound healing when combined with sqhGFP, leading to delayed and inconsistent closure (unpublished). Additionally, maintaining stable homozygous *rnGAL4* fly stocks has proven to be inviable in our lab, whereas homozygous *nubGAL4* stocks remain viable, making them the more practical choice for these experiments.

These experiments provide a 3D perspective to Mbs knockdown in wound healing. As the purse string forms and contracts, the wound edge experiences inward forces pulling toward the wound, outward forces from membrane and cortical tension, and downward forces due to volume conservation, potentially aided by lateral cables (LCs). In Mbs RNAi wounds, since the wound remains almost fully open, volume conservation is not disrupted, reducing the need for apical indentation or LC engagement. Additionally, myosin depletion limits the recruitment of new filaments, while persistent, stable LCs may undergo photobleaching, contributing to the observed decline in mean LC myosin intensity over time. This also suggests that cell shortening may facilitate intercalation, as reducing cell height increases lateral surface area, enabling neighbouring cells to slide past one another more easily. In contrast, tall, narrow cells may have limited space for rearrangement, hindering efficient intercalation and wound closure. Both Rok and myosin phosphatase have broad roles in many cellular processes, and it is difficult to distinguish their roles in LC formation. Changes in tissue tension likely affect overall wing disc height.

Fascin, an actin crosslinker, may be another candidate for regulating actin cable length. A unique property of the LCs in the wing disc compared to other actomyosin structures is their 40μm length span when the wound initially forms. The persistence length of actin filaments has been measured to be 15 μm in vitro but can be increased by the addition of Fascin to 10-150 μm [271]. Fascin has roles in bundling actin in protrusions for cell migration, so perhaps it has a role in maintaining the mechanical integrity of the LCs [272].

Alternatively, if a specific molecular regulator of the LCs cannot be identified because these effects are rescued by the presence of compensatory

regulators, myosin activity in the lateral sides of the wing disc could be decreased using optogenetics. Guo et al utilised optogenetic-mediated acute inhibition of actomyosin via the recruitment of Rho1DN in *Drosophila* embryos to cause tissue relaxation and subsequently prevent mesoderm invagination [273]. Another study developed optoGEF and optoGAP to control Rho1 signalling and disrupt myosin during *Drosophila* germband extension [274]. These tools could be used in wounded wing discs to disrupt actomyosin contractility in at least part of the cable.

In conclusion, I have demonstrated that LCs are robust structures that persist through perturbations related to endocytosis, IACs, and myosin regulation. I have established a pipeline and a list of candidate proteins to continue screening for a molecular regulator that controls LC formation. While none of the perturbations performed abolished LC formation, I have identified and prepared many other possible candidates to screen, which is currently ongoing. It is also important to characterise the cell and tissue shape as a result of these perturbations. These experiments highlight the need to consider the basal side of the wound during closure analysis. Furthermore, previous imaging shows that the basal surface does not indent at the same time as the apical surface. In contrast to the apical surface, cells are linked to the BM by IACs. IACs mechanically and biochemically link cells to the BM [126]. The role of the BM itself in wound healing is poorly understood, and I set out to investigate this in my next chapter.

6 Role of the basement membrane in wound repair

6.1 Introduction

Previous imaging and quantification by Dr Rob Tetley showed that the basement membrane (BM) deforms as the overlying wound edge cells shorten (Chapter 3.1). Unlike the apical cell surface, which begins deforming within 10 min of wounding, the BM shows no visible deformation until 40 to 60 min later. While the role of the BM is well-established in tissue morphogenesis and cell migration, its role in *in vivo* wound healing is poorly understood [36,117,126].

In *Drosophila*, the BM is composed primarily of Collagen IV, Laminin, Perlecan and Nidogen. It serves as a structural and signalling platform, influencing cell behaviour, differentiation, and migration [11,139]. The BM connects to the cells via integrin adhesion complexes (IACs), where Talin links integrins to the actomyosin cytoskeleton. In *Drosophila* imaginal discs, localisation and clustering of Talin and Integrin at the basal surface are interdependent [199]. During *Drosophila* embryonic wound healing, Talin and Integrin are both shown to localise in cells at the wound edge [129,260]. Integrin mutations can cause detachment from the BM, resulting in severe morphogenetic abnormalities or lethality [275,276]. For instance, in *Drosophila* wing morphogenesis, integrin loss-of-function mutations cause blister defects as the ventral and dorsal sides of the developing wing cannot properly appose [277–279]. Gain-of-function mutations in Talin and Integrin also cause similar defects in morphogenesis [259,280,281]. In the *Drosophila* embryo, dorsal closure is delayed by the impairment of Talin autoinhibition [259]. Here, Talin turnover is reduced, which increases integrin activation and prevents migrating cells from reorganising their adhesions to move forward.

Similarly, in mouse embryonic fibroblasts, increased integrin activation via blocked talin autoinhibition resulted in the formation of more mature, stable focal adhesions and, consequently, mutant cells attach more strongly to the underlying ECM. At the same time, actin becomes more dynamic and less organised inside mutant cells, reducing traction forces and enabling cell

migration during wound closure. Collectively, these changes in cell behaviour cause delayed wound closure in wounded mice *in vivo* [258].

Loss of integrin leads to increased skin blisters along with BM defects in mice [130], whilst activating JNK signalling and multinucleate syncytium formation in *Drosophila* epidermis [131]. In wounded *Drosophila* embryonic epidermis, Integrin knockdown and inhibition delayed wound closure and altered actin organisation at the wound edge [129]. These studies show the strong interdependence between the BM, integrin, talin and actomyosin in wound healing.

Changes in BM composition can change its mechanical properties, such as stiffness and ultimate tensile strength [126]. For example, elongation in the *Drosophila* egg chamber is driven by the alignment of Laminin fibrils and f-actin to generate a corset that mechanically constrains the egg [143]. Removing the egg BM with collagenase results in rounding. In the developing wing disc, the BM constricts cell shape, contributing to the emergence of tall scutoid cells [145,174]. Atomic force microscopy revealed that BM stiffness mainly depends on Collagen IV [282].

Furthermore, *collagen IV* knockdown or using collagenase and matrix metalloproteinases (MMPs) to remove the BM in the wing disc induces ectopic folds and cell height reduction [144–146]. Changes in individual BM components can change tissue shape; for instance, in the wing disc, *perlecan* knockdown increases cell height and apical surface area, whilst *perlecan* overexpression decreases cell height and wing disc surface area [144,145]. Perturbing cell-BM adhesions can reproduce similar phenotypes; for example, cells lacking the βPS Integrin subunit have a reduced height compared to their wildtype neighbours in models across *Drosophila* and zebrafish [146,283,284]. Removal of the BM leads to altered wound repair mechanisms, as demonstrated by the preference for purse string-driven repair over lamellipodial-driven repair in *in vivo Clytia* wounds upon BM damage at the wound [74].

In this chapter, I aimed to determine the role of the BM in wing disc wound healing by altering IACs and removing the BM at the wound site. Firstly, I use

the wound healing quantifications established in Chapter 5 to assess the impact of dominant negative (DN) Integrin on wound healing. As outlined in the previous chapter, imaging of the full wound in the wing disc is technically challenging. This difficulty is particularly pronounced by BM perturbations as they often lead to excessive folding and dramatic shape changes, complicating the identification of a flat group of cells to wound and image. These experiments indicated the need to develop other imaging protocols to image the whole wound. I used 10kDa dextran to mark media within the wound site and surrounding the tissue surfaces. Secondly, I sought ways to acutely and locally alter BM through laser ablation to avoid genetically disrupting the whole pouch region and maintain the overall wing disc morphology.

6.2 Dominant negative integrin decreases apical indentation and intercalation rates

Drosophila integrins are composed of an alpha subunit and a beta subunit. There are 5 different alpha subunits, αPS1-5 and 2 beta subunits, βPS and βv. In the wing disc, αPS1βPS is expressed dorsally, and αPS2βPS is expressed ventrally. Both integrins commonly share the βPS subunit, also known as myospheroid (*mys*) in *Drosophila*. To disrupt the BM binding function of Integrin, I used a dominant negative (DN) form of Integrin (referred to as Integrin DN). In this mutant, the βPS cytoplasmic domain is fused with an extracellular reporter domain; however, it can still recruit Talin [146,178]. This mutant causes wing disc cells to become cuboidal instead of columnar. It replicates similar phenotypes seen by either genetically removing all βPS integrin subunits or overexpressing MMP2, suggesting that BM adhesion is perturbed in this DN mutant [146].

I hypothesise that if mechanical adhesion to the BM is disrupted via Integrin DN, although the lateral cables may form, cell shortening will be increased as cells will face less resistance from the BM. Here, the BM provides mechanical resistance to cell shortening by exerting a tensile force perpendicular to the basal surface. I further hypothesise that this force

triggers an outside-in signalling cascade, which helps unfold talin and promotes further IAC clustering on the basal surface.

To confirm the expression of these loss-of-function mutants driven by *nubGAL4*, I imaged whole pouch regions of unwounded discs and observed adult wing phenotypes. Unwounded wing discs displayed similar cell shape changes as previously reported in literature, including drastically shorter cells (Figure 6.1.A-B) [146]. Adult wings exhibited the blistered bubble phenotypes as previously reported (Figure 6.1.A'-B') [146].

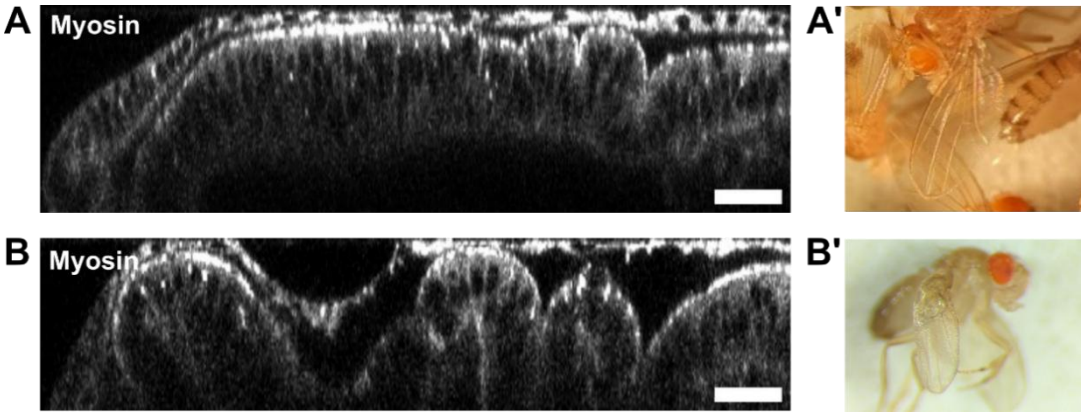

Figure 6.1: Integrin DN induces cell shape changes in wing discs and blistering in adult wings.
Images from flies of genotypes *sqhAX3/Y; sqhGFP, nubGAL4/+; +/+* (control) and *sqhAX3/Y; sqhGFP, nubGAL4/+; UAS-mysDN/+.* A) Side views through the centre of live myosin-GFP tagged wing discs. C) Adult wing phenotypes. Scale bars are 20μm.

There is no significant difference in apical wound area closure between control and Integrin DN wounds (Figure 6.2.B-B'). However, apical PS myosin intensity differs significantly between the two conditions ($p = 0.0480$, Mann-Whitney, Figure 6.2.C-C'). Mean PS myosin intensity peaks at approximately 3-fold in control wounds, whereas in Integrin DN wounds, it peaks at around 2.5-fold (Figure 6.2.C). The mean rate of PS myosin intensity decline is also slower in Integrin DN wounds at -0.0107 ± 0.0052 min^{-1} compared to control wounds at -0.0211 ± 0.0086 min^{-1} (Figure 6.2.C'). These findings are surprising as Ly et al. previously reported that Integrin knockdown in *Drosophila* embryo wounds delayed wound closure by up to

54%, yet myosin accumulation remained unaffected [129]. These differences may be due to the dramatic differences in *Drosophila* embryo and wing disc cell shape. Embryonic cells are also at an earlier developmental stage than L3 wing disc cells, so they may display greater regenerative ability. Furthermore, while Integrin DN reproduces the cell shape and BM defects seen in Integrin knockdown, it retains certain signalling functions, such as Talin binding, which may help regulate myosin dynamics at the wound site.

The rate of apical indentation in Integrin DN wounds is significantly lower than in control wounds (p=0.0303, Mann-Whitney, Figure 6.2.D-D'). Control wounds exhibit a mean apical indentation rate of 0.0674 ±0.0227μm min^{-1} while Integrin DN wounds show a reduced rate of 0.0406 ±0.0175μm min^{-1} (Figure 6.2.D'). By 120 min, control wounds reach an apical indentation of 7.695 ±1.660μm, whilst Integrin DN reach 5.119 ±1.531μm. Using approximate wing disc cell height values (Figure 6.1.A-B), this corresponds to a reduction in overall cell height of 19% in control wounds and 26% in Integrin DN wounds.

The percentage of apical junctions in Integrin DN wounds decreases at a significantly slower rate than observed in control wounds at -0.3810 ±0.1158% min^{-1} and -0.6103 ±0.2195% $min^{-1,}$ respectively (p=0.0303, Mann-Whitney, Figure 6.2.E-E').

No significant differences are observed in the number of LCs or mean LC myosin intensity per wound (Figure 6.2.F-G). At 60 min, there is a significant decrease in mean LC myosin intensity per cable between control and Integrin wounds at 0.823 ±0.283 and 0.545 ±0.199, respectively (Figure 6.2.H, p=0.0001, Mann-Whitney). This decrease was also measured in Talin, Rok, Mbs and Cdep knockdown experiments in Chapter 5. Similarly, the effects of Integrin perturbation may be delayed as IACs remodel, affecting myosin stability at later timepoints [261,262].

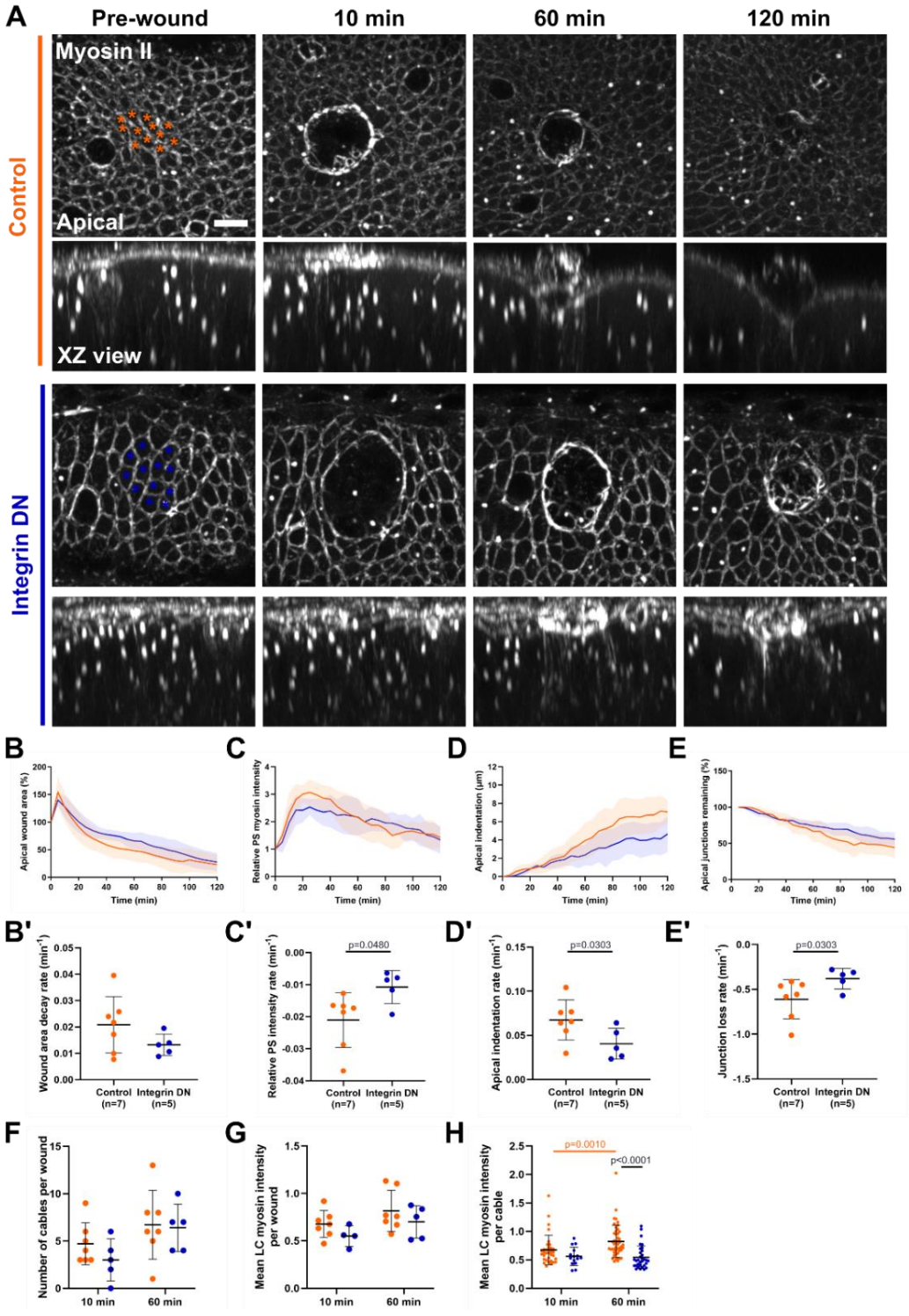

Figure 6.2: Dominant negative Integrin reduces apical indentation but does not affect wound closure.

A) Timelapse images for wounded control discs with genotype *sqhAX3/Y; sqhGFP, nubGAL4/+;* (orange, n=7) and wounded Integrin DN discs with genotype *sqhAX3/Y; sqhGFP, nubGAL4/+; UAS-mysDN/+* (blue, n=5) expressing myosin-GFP. Asterisks indicate dead cells. B) Apical wound area.

B’) Wound area decay rates from fitting one-phase decay curves of individual replicates from B. C) Relative PS myosin intensity. C’) Relative PS myosin intensity reduction rates from fitting straight lines of individual replicates from C. D) Apical indentation. D’) Apical indentation rates from fitting straight lines of individual replicates from D. E) Apical junctions remaining as cells are eliminated from the wound edge. E’) Junction lost rates from fitting straight lines of individual replicates from E. F) Number of cables per wound 10 min and 60 min after wounding. G) Mean lateral cable (LC) myosin intensity per wound 10 min and 60 min after wounding. H) Mean LC myosin intensity per cable 10 min and 60 min after wounding. For B-E, shaded areas represent the SD. For B’-E’ and F-H, plots show individual data points with the mean (horizontal line), SD (bars) and p-values from two-tailed Mann-Whitney tests. For F, p-values between different timepoints were calculated using Wilcoxon matched-pairs signed rank tests. Scale bars are 5μm.

These results show that LCs can assemble under Integrin DN where adhesion to the BM is reduced. Although it appears that apical indentation rate is reduced, when considering the reduced cell height under Integrin DN this indentation is similar to or even greater than the control wounds. Furthermore, Integrin DN wounds can heal as quickly as controls despite reduced intercalation. Normally, stiffer tissue tension delays closure by limiting apical intercalation [104]. However, reduced BM adhesion and shorter cell height under Integrin DN may facilitate cell shape changes, lessening the mechanical need for extensive apical rearrangement. With less resistance from the BM, cells may instead deform or move more easily through their basolateral domains, compensating for reduced apical intercalation and enabling efficient wound healing. In the control situation, wound edge cells are anchored basally to the BM, forcing them to rearrange apically to relieve tissue tension generated by the contracting purse string. When BM adhesion is weakened, as in Integrin DN tissues, basolateral domains become freer to move and accommodate shape changes. Additionally, Integrin DN may perturb the basal actomyosin network by competing with wild-type Integrin for Talin binding [146], potentially reducing basal tissue tension and further facilitating wound closure.

The previous findings highlight the need to observe basolateral dynamics during wound closure and, indeed, the cell and tissue shape as a whole. Due to the altered cell height of Integrin DN cells before wounding (Figure 6.1.A-B), I sought to optimise imaging protocols to quantify the complete wound edge cell height with my current experimental crosses using *sqhAX3; sqhGFP,nubGAL4;* flies. Dextran is a hydrophilic polysaccharide that can be conjugated with various fluorescent dyes and is available in molecular weights from 3 kDa to 2000 kDa. It is commonly used as a tracer for permeability, cell lineage and cell-cell communication. I selected Alexa Fluor 647-conjugated dextran to minimise spectral overlap with myosin-GFP. Additionally, 10 kDa dextran was the optimal choice for marking the extracellular space, as it is small enough to diffuse freely but unlikely to enter intact cells. I am currently optimising these experiments and will outline an example analysis in this subsection.

Preliminary cell height measurements from these single discs were obtained by taking the mean ± SD of 3 separate cell height measurements on the pre-wound image. Control wing disc cell height is 25.2μm ± 3.9μm, and Integrin DN wing disc height is 25.8μm ± 0.4μm. Although crosses for both control and Integrin discs are staged at the same time, there can be differences in development time. I have selected a control disc that is of similar height to Integrin DN. While it is likely that the control disc is slightly younger and may heal faster, the similarity in their starting geometries allows for a more comparable analysis of cell shape changes.

From these initial images, I can quantify the cell height before wounding, but after ablation, the basal boundary of the wound is not as obviously marked as with Collagen IV in previous imaging (Chapter 3.1). As such, it is difficult to measure the basal indentation accurately without a BM marker. I quantified the average curvature and curvature variance σ^2 with the Kappa Fiji plugin to analyse differences in basal deformation at 60 min and 120 min after wounding.

Average curvature of the basal surface changes negligibly between time points for control and Integrin DN discs (Figure 6.3.C). The mean average

curvature of the control basal surface is 0.0704 μm^{-1} at 60 min and 0.0660 μm^{-1} at 120 min. The mean average curvature of the Integrin DN basal surface is 0.0348μm^{-1} at 60 min and 0.0294μm^{-1} at 120 min. The control basal surface is overall more convex than the Integrin DN basal surface. These values indicate that the control basal surface is more convex compared to the Integrin DN basal surface. Curvature variance indicates how uniform the curve is. The basal surface behaviour within a single control is variable (Figure 6.3.D, orange), whilst Integrin DN basal surfaces become more uniform between 60 min to 120 min (Figure 6.3.D, blue). These findings suggest that control wound edge cells maintain their height, possibly due to strong lateral tension keeping the wound edges straight. In contrast, Integrin DN wound edge cells shorten, creating a more gradual curve on the basal edge. This may be due to the overall shorter cell shape but also, reduced adhesion to the underlying BM. There are likely other effects on the organisation actomyosin cytoskeleton that affect overall tissue tension.

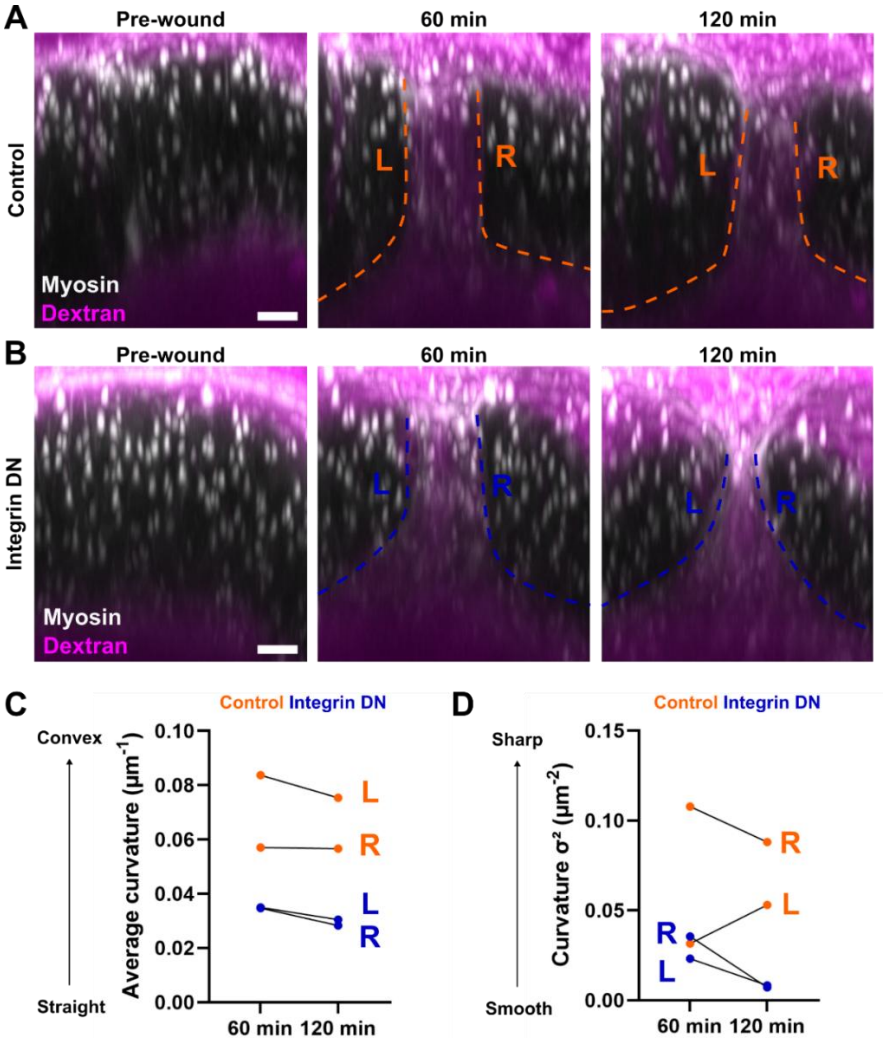

Figure 6.3: Basal surface curvature is more gradual and uniform in Integrin DN wounds compared to control.

A) Timelapse images of control discs with genotype *sqhAX3/Y; sqhGFP, nubGAL4/+;* and B) Integrin DN discs with genotype *sqhAX3/Y; sqhGFP, nubGAL4/+; UAS-mysDN/+* expressing myosin-GFP (white) with media mixed with Dextran Alexa Fluor 647 (magenta). C) Average curvature (n=1 for control and Integrin DN). D) Curvature variance σ^2 (n=1 for control and Integrin DN). L and R denote measurements from the left and right sides of the wound, respectively. Orange and blue denote control and Integrin DN disc, respectively. Scale bars are 5 μm.

It is difficult to disentangle the effects of cell shape on wound healing in Integrin DN discs and other BM perturbations. In the next section, I use laser ablation to acutely remove the BM to preserve the surrounding wing disc morphology.

6.3 Removing the BM from the wound by laser ablation

There are several ways to remove the basement membrane from the wound, summarised in Table 6.1. Drug or enzymatic treatments, such as collagenase, can degrade the BM from dissected wing discs. The duration and concentration of treatment can alter the severity of BM removal. Genetic methods such as RNAi can be used to knock down the expression of genes encoding Collagen IV, Laminin, Perlecan, or Nidogen. Tissue-specific drivers or mosaic clones can target these genetic manipulations to specific cell types or regions within the wing disc. However, genetic perturbations introduced during development may lead to adaptive changes in gene expression, making it challenging to isolate the direct effects of BM perturbation. Laser ablation offers several advantages over these methods, including precise and localized targeting of the BM and the ability to be performed simultaneously with cell ablation, minimizing off-target effects.

Method	Type	Timescale	Spatial precision
Laser	Physical	Immediate	Local
MMP overexpression	Genetic	Hours (throughout development)	Locally, via mosaic clones, tissue-specific drivers, or the whole wing disc
Collagenase	Chemical	Immediate (after dissection)	Tissue wide

Table 6.1: Summary of methods to ablate the BM.

To examine the role of the BM locally at the wound site, I used laser ablation to damage the BM and reduce cell-BM adhesion at target cells. In these preliminary experiments, I drew a single circle ROI of approximately 15 µm in diameter. Then, I laser ablated the apical surface of the target cells to create a wound. The wing discs are mounted in the coverslip sandwich, allowing me to alternate between the apical and basal sides of the wing disc for ablations. I used GFP-CAAX to mark cell membranes and *UAS-vkg-mScarlet* driven in fat body cells, to mark the BM. These wounds are referred to as cell and BM ablations or complete ablations, whereas controls will be referred to as cell ablations.

The diameter of the BM gap appears to decrease slightly 100 min after BM ablation (Fig 6.1.A). Figure 6.1.B shows example images of wounds after 100 minutes for both cell-only ablation and combined cell and BM ablation, including corresponding XZ views. In these images, debris is seen ballooning above the apical surface into the lumen. I was unable to accurately quantify the wound area using GFP-CAAX as a marker because it is difficult to clearly distinguish the debris from the actual wound edge. Similarly, the lateral boundaries of the wound are also obscured by debris, making it challenging to analyse tissue height and curvature as described in the previous section. To more precisely define "final closure" in future experiments, I plan to use a cytoskeletal dye such as SiR-actin to label the actin purse string, which would provide a clear and continuous edge to track wound closure over time. In this approach, "final closure" would be defined as when the labelled actin purse string completely seals the wound area, with no detectable gap.

Alternatively, adding dextran as mentioned in Fig 6.3 to mark the wound gap could also help visualise the wound edge and allow closure to be defined as the complete exclusion of dextran from the wound site.

By visual inspection, the wound edge cells appear elongated towards the wound in the control cell-only ablation wound (Figure 6.4.B, top). In contrast, the wound edge cells appear rounder and more homogenous in shape in the cell and BM ablation wound (Figure 6.4.B, bottom). This supports the hypothesis that the BM indirectly affects actomyosin dynamics and, in turn, cell shape. It is also consistent with the findings that partial loss of substrate adhesion triggers actomyosin remodelling, facilitating further adhesion loss and cell rounding in HeLa cells [285].

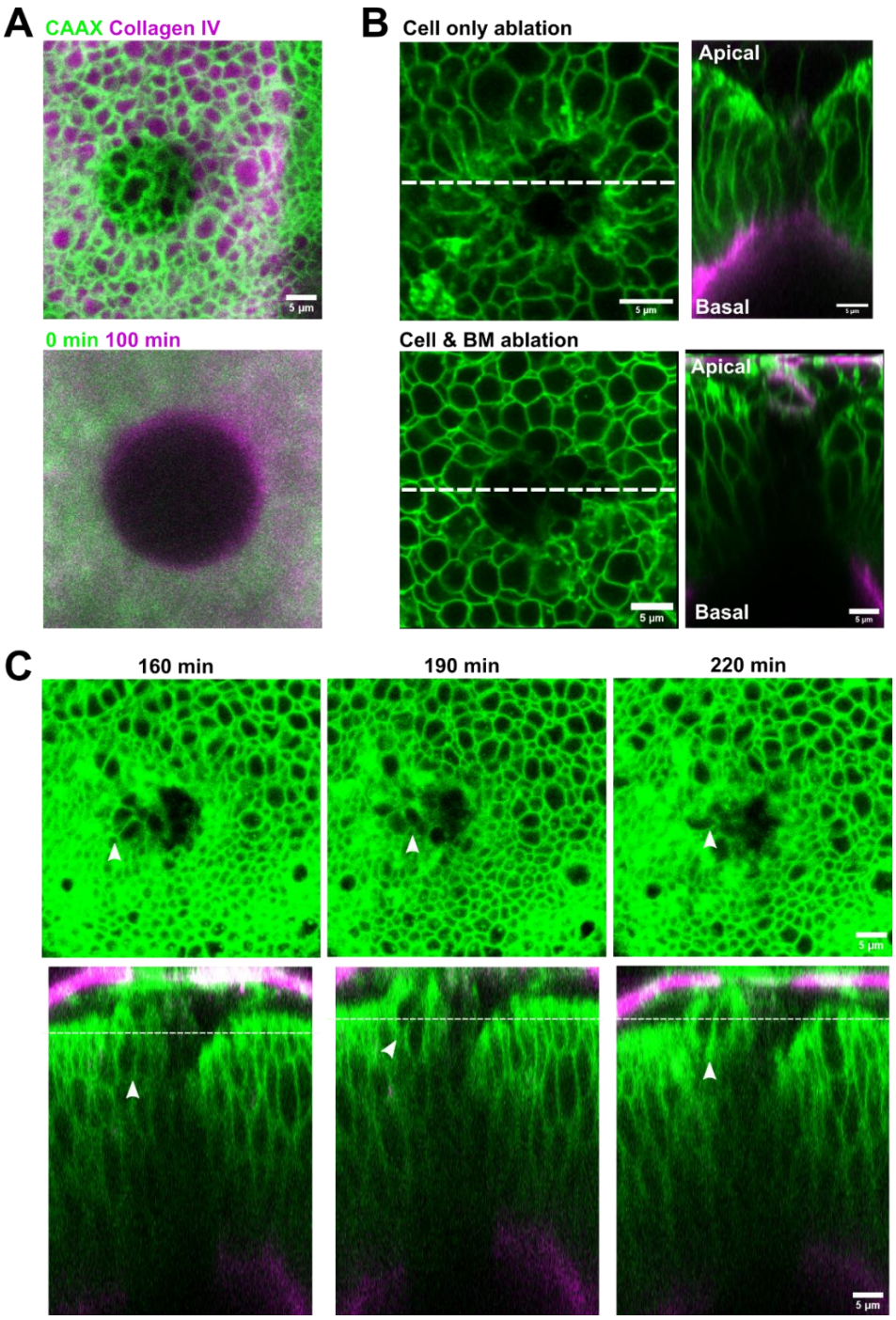

Figure 6.4: BM ablation at the wound site causes cell rounding.

A) BM ablations before cell ablation is performed (top). Comparison of the BM ablation gap 5 min post-ablation (green) and 100 min post-ablation (pink). B) Cell-only ablation 120 min post-wounding and XZ view (top) and a cell and BM ablation 120 min post-wounding and XZ view (bottom). C) Another example of a cell and BM ablation and respective XZ views 160 min, 190 min, and 220 min after cell ablation. A white arrow indicates a dividing cell. Scale bars are 5 µm.

Interestingly, there appears to be a dividing cell that moves above the apical surface of the columnar epithelium (Figure 6.4.C). In pseudostratified epithelia, nuclei migrate towards the apical surface before rounding up and dividing in plane in a process known as interkinetic nuclear migration [286]. These dividing cells remain attached to the BM via an actin-rich basal process [287]. The aberrant division observed in BM-ablated wounds is unusual and has implications in tissue disorganization, loss of polarity, EMT, and tumour initiation. To confirm that this is a proliferating cell rather than debris, I will use Hoechst to identify dead cells and mitotic markers to identify proliferating cells in wounded epithelia. I could also use a polarity marker to determine whether the loss of the BM disturbs cell polarity. Furthermore, I could perform bigger ablations to increase the likelihood of proliferation events at the wound edge.

6.4 Discussion

It is crucial to consider the whole 3D shape of the cells in these experiments. Integrin DN causes wing disc cells to become cuboidal instead of columnar [146]. Consequently, although apical indentation in Integrin DN discs appears to have decreased, this represents a larger change in indentation when accounting for full cell height. Accurate quantification of cell shortening requires measuring cell height both before and after wounding. Additionally, imaging should extend beyond 120 min, continuing until wound closure, as there may be differences in final closure that current experiments are missing.

To address the challenge of imaging the full cell height, I used dextran to visualise the media surrounding the tissue; however, as wounding progressed, the basal surface started to curve, and it was difficult to distinguish the bottom of the tissue without a BM marker. Instead, curvature analysis shows that the basal surfaces of Integrin DN wounds have more rounded edges, whereas control wounds have more convex, sharper edges. These shape changes allude to the role of the BM in cell shape. Wound healing delays may arise from the need to remodel IACs, a process that takes minutes to hours [261,262]. These results suggest that BM adhesion is

not essential for wound closure but altered cell shape could result in different closure mechanisms. One such way is through its interactions with the actomyosin cytoskeleton. To investigate this further, junctional recoil experiments of apical junctions in unwounded discs and the purse string will be performed to assess measure tissue tension in Integrin DN discs before wounding and during closure. Secondly, lateral ablations of the LCs to quantify if there are changes in the contractility of the LCs.

Other integrin perturbation experiments could be performed to verify these results, for example, Integrin knockdowns or RGDS (Arg-Gly-Asp-Ser) treatment to chemically block integrin-BM interactions. Since Integrin loss-of-function perturbations heavily impact wing disc tissue integrity, Integrin overexpression or Talin autoinhibition mutants may be investigated to alter wound healing [259]. These mutations have been shown to cause more stable IACs, which reduce cell mobility and rearrangement, ultimately delaying wound closure.

Another way the BM may regulate cell shape is by confining cells to specific morphologies. In the wing disc, cells assume their long apicobasal elongated shape as the BM limits available planar space [144,145,149]. In agreement with this, BM degradation and *perlecan* knockdown lead to opposite changes in the apical cell area [145]. Similarly, *laminin* depletion in *Drosophila* embryonic tracheal tubes caused the apical and basal surfaces of tracheal tubes to enlarge compared to controls [288].

To investigate if the BM itself has a role in wound healing, particularly in cell shortening at the wound edge, I sought to remove the BM by laser ablation and observe the effects on wound closure. If LCs require BM attachment to generate tension, I expected to observe no tissue indentation at the wound edge and delayed wound closure. Conversely, the BM could hinder BM shortening by resisting the forces generated by the lateral cables. In this case, removal of the BM from the wound site and wound edge cells could accelerate wound healing. Without the BM, the cells are free to shorten, which has been demonstrated during wing disc morphogenesis [121].

Alternatively, wound closure may be completely unaffected by BM removal as the BM does not have a contributing role.

Tissue height is decreased at the wound edge as well as several rows of cells away in both the cell-only ablation and complete ablation. The rate of tissue indentation is similar in both discs; however, longer timelapses of over 4 hours is needed to determine if this trend continues after 120 min as well as if these wounds fully close and if the tissue recovers its original height. Quantifications, such as those made in Chapter 5, are needed to assess wound healing under BM ablation. However, using a cell membrane marker, as previously discussed in Chapter 5.5.2, has limitations in defining the wound area and tissue height. In future experiments, dextran dye could be used to mark basal cell edges and indicate full wound closure, allowing more accurate quantifications of wound area, cell height, and tissue height.

It was challenging to align the BM and cell ablations due to the curved shape of the wing disc pouch. As a result, the wound gap is often tilted so that the BM directly beneath the apical signal may not be underneath the basal surfaces of the same cells. It is also likely that in these first qualitative trial experiments, I did not damage the BM enough for cell-BM attachments to be sufficiently reduced. In successful BM ablations, I expected to observe cell debris leaking from the BM gap, as observed in other BM ablations performed by Dr Nargess Khalilgharibi in the lab. I aim to repeat these BM ablations with higher laser powers to ensure that the BM is properly damaged. Furthermore, draw bigger ROIs to ensure damage to the BM beneath future wound edge cells.

Despite the previously mentioned caveats with these BM ablation experiments, cell shape appears to be perturbed in the complete ablation (Figure 6.4.B). Instead of the elongated shape observed in wound edge cells in cell-only ablations, wound edge cells appear more rounded in the BM and cell-ablated wounds. This suggests that the actomyosin purse string may be perturbed or perhaps more intercalations are occurring. To investigate this, I aim to image actomyosin proteins such as myosin II, especially apical and

lateral to the wound edge in wounds with BM ablation. 3D segmentation of wound edge cells is required.

I am currently developing a pipeline to quantify cell shape in wound-edge cells. I carried out a preliminary analysis using Cellpose 1.0 to segment confocal images of the wound with membranes marked with CAAX-GFP (Figure 6.5.A-D) [189]. Future iterations of this analysis will be performed using the most recent Cellpose 3.0 release [289]. These masks will be manually corrected to remove masks in the wound gap and correct any incomplete or over-segmented cells. Then, cell shape measurements, such as roundness and aspect ratio, will be measured to provide insights into cell mechanics [290].

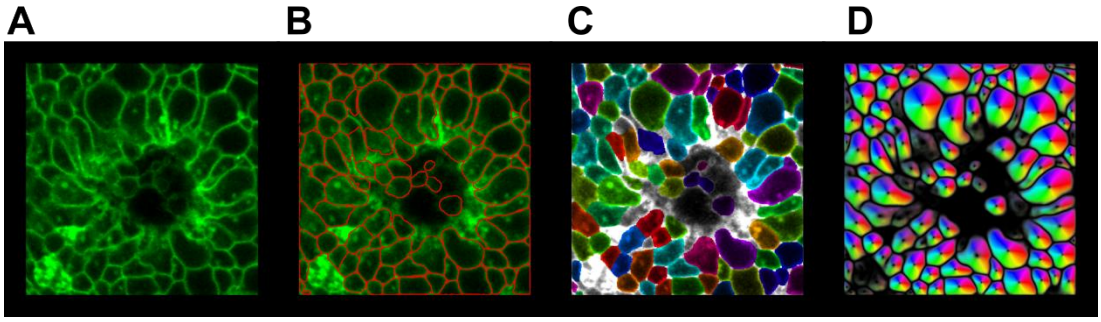

Figure 6.5: Cellpose pipeline to quantify cell shape properties.
A) Confocal image with GFP-CAAX in green from Figure 6.4.B (top). B) Predicted outlines. C) Predicted masks. D) Predicted cell pose. This is a representation of the spatial arrangement and shape of detected cells [189].

As outlined in Table 6.1, there are multiple ways to perturb the BM, and future experiments could employ these methods to better understand the role of the BM in wound healing. For example, using collagenase or MMP overexpression to acutely remove BM from the wing disc. I will also alter Collagen IV, Laminin and Perlecan levels with RNAi or overexpression mutants, and quantify the effects on wound healing by measuring the rate of wound area closure, tissue and cell height, and intercalation rate. Alternatively, mosaic clones could be used to remove the BM with cell-specific precision. These clones would be the target cells for ablation. As the BM perturbations themselves could affect wound healing, I could

mechanically stretch or compress the wing disc to change cell shape, using the stretcher developed in the lab [187].

Distinguishing the BM's role in cell shape from its role in wound healing remains challenging. Models where BM removal has a less pronounced effect than in the wing disc may provide better clarity, such as squamous cell models like *Clytia hemisphaerica* or cuboidal *Drosophila* tissues like the leg disc or pupal epidermis.

In light of these experiments, I conclude it is unlikely that the BM causes the delays in basal deformation by providing lateral resistance to the LCs. Instead, given that the BM is relatively thin compared to disc proper cells (ranging from 100 nm to 1 μm), its primary forces are likely exerted in the planar direction. The BM likely affects tissue tension in its overlying cells by its indirect interactions with the actomyosin cytoskeleton, which allows cell shape change. Furthermore, given that the wound exposes the underlying basement membrane (BM), it is likely that these basal networks undergo significant remodelling to cover the exposed BM in later stages of healing.

Overall, the role of the BM remains unclear during *Drosophila* wing disc wound healing. Initial observations of cell shape suggest that 3D cell shape is perturbed by BM removal. It would be interesting to investigate how these rounded wound-edge cells adapt their wound healing mechanisms to heal the wound. These experiments raise further questions about the basolateral dynamics of wound closure. Alternatively, the BM may act as a structural "memory," helping preserve tissue shape rather than actively generating it. If so, small wounds might not be sufficient to disrupt this memory, and delays in healing could be attributed to actomyosin cortex and IAC remodelling at the basal surface. I am currently performing more BM ablation experiments, particularly with a focus on imaging and quantifying cell and tissue shape at the basal surface over longer periods until wound closure.

7 Conclusions and Outlook

This thesis aimed to investigate 3D cell shape changes in wound repair and identify the mechanisms responsible for these 3D changes. Preliminary experiments performed by Dr Rob Tetley demonstrated that upon wounding, cells at the wound edge shortened and the underlying BM deformed with the shortening cells. A possible mechanism for this shortening was lateral actomyosin cables that appeared to be under tension at the wound edge. I built on this previous work by further characterising wound edge cell behaviour and exploring ways to image the lateral cables with higher spatial resolution (Chapter 3). Then, I examined the use of FRET-based tension sensors in ex vivo wounded wing discs (Chapter 4). Afterwards, I genetically perturbed potential lateral cable regulators (Chapter 5) and genetically perturbed cell-BM adhesions and physically perturbed the BM at the wound site (Chapter 6). Under these perturbations, I quantified wound healing dynamics, including developing new methods to identify lateral myosin intensity from 3D images. In this final chapter, I summarise my results and discuss the future directions of this project.

7.1 Visualising 3D cell behaviour in the wing disc

In Chapter 3, I first quantified the volume and cell height of wound-edge cells together with Martin Zhang. We found that wound edge cells conserve their volume but decrease in height by approximately 40% during wound closure. These results build on preliminary experiments from a previous postdoctoral researcher in the lab, Dr Rob Tetley, and validate a key assumption to our cell shortening hypothesis. Since cell volume is conserved, this forces cells to expand and flatten into the wound gap.

However, the behaviour of other wound edge cells remains unknown and will require full segmentation, which is challenging due to dead cell debris when using cell membrane markers. Future experiments could use dextran to mark the wound gap for better segmentation.

I further examined LCs and showed that they colocalise with actin along the whole apicobasal axis of the wound. These cables are difficult to segment

and require substantial manual correction. LCs also colocalise with Talin at the basal surface. I quantified Talin intensity in regions around the wound and found that, surprisingly, Talin intensity increases with distance from the wound edge. These results need to be verified using another microscopy technique. Additionally, the shape and size of these Talin puncta will be analysed.

I explored the feasibility of using ExM in imaging wing discs to expand wounded wing discs to more closely examine how the lateral cables are anchored basally, possibly to IACs. It would also be interesting to quantify the presence of other cell-BM adhesion proteins, such as Integrin.

7.2 Measuring forces in *ex vivo* wing discs

Since there must be mechanical forces driving the cell shortening quantified in wound-edge cells, I sought to measure such forces. I explored the feasibility of using FRET-based TS to measure forces around the wound in wounded *ex vivo* wing discs. These experiments highlight key considerations when designing and optimising tension sensor experiments in 3D tissues.

Firstly, the need to acquire controls in unwounded conditions, particularly as there are no published results utilising these TS constructs in larval wing discs. This would ascertain whether these constructs are sensitive to pre-existing active forces maintaining the homeostatic cell shape, particularly as several studies show that apical and basal actomyosin contractility are key to creating and maintaining wing disc shape [60,149,174].

Secondly, it is important to ensure that the sensor is measuring forces in the correct orientation. Forces due to lateral cables could act perpendicularly to the basal membrane, leading to Talin's perpendicular orientation. However, it is difficult to determine the exact direction and source of forces, as Talin's binding sites allow for multiple orientations and interactions.

Thirdly, the ability to acquire enough signal from the fluorophores in FRET-TS constructs to obtain meaningful and robust FRET measurements. Due to the geometry and size of the wing disc, it is difficult to mount the wing disc on the coverslip without introducing mechanical perturbations that may influence

TS measurements. As such, the intensities measured previously are very low, barely above background signals, as discs are suspended in media away from the coverslip.

In conclusion, without further time-consuming controls and prior knowledge on the spatial arrangement of force-contributing structures bound to Talin at the basal surface, FRET-based TS are unsuitable for the measurement of forces in wounded wing discs. To attempt to optimise the FRET-TS in the future, FRET measurements should first be taken in unwounded discs.

7.3 The molecular mechanisms behind lateral cable formation

As it is difficult to measure forces without knowing where and how the forces are being generated, I searched for key regulators of the lateral cables. To evaluate the formation and function of the LCs, I quantified wound area, apical purse string intensity, apical indentation, and lateral myosin intensity. Under loss-of-function perturbations of key actomyosin-related regulators, I expected the LCs to fail to form and, subsequently, apical indentation and wound area closure to decrease.

I first focused on how the cables might attach to the apical and basal cell surfaces. Apical purse string assembly is coordinated at AJs at the wound edge, so they are possible sites of lateral cable nucleation. Under perturbed endocytosis via a temperature-sensitive *shibire* mutant, the apical purse string myosin intensity is reduced but does not prevent apical indentation or LC formation. Talin knockdown alters tissue morphology but does not impair wound closure or LC formation. Mbs knockdown caused delayed wound closure, apical indentation, and intercalation. Furthermore, reduced LC myosin intensity after 60 min. These impairments in repair are likely due to defective myosin turnover and stiffer tissue tension in this mutant.

Next, I started screening upstream regulators of myosin phosphorylation, RhoGEFs and RhoGAPs. Knockdown of Cdep, a RhoGEF that localises to the lateral membrane in rounding cells undergoing division, does not appear to affect wound healing. These experiments laid the groundwork for an

ongoing screening pipeline to identify actomyosin-regulators in LC formation and wound healing in general. Other cytoskeletal filaments, specifically microtubules may also play a role in maintaining cell shape during wound healing [291].

7.4 The role of the BM in wound healing

To explore the role of the BM in wound healing, I perturbed the adhesion functions of IACs on the basal surface using a dominant negative form of Integrin. Integrin DN alters wing disc cells from columnar to cuboidal, meaning that despite reduced apical indentation, the overall change in cell height is greater, and the overall wound closure rate was unaffected. These experiments, together with those in Chapter 5, demonstrate that the full cell height should be considered in these experiments. To visualise cell height, dextran was used, but proved insufficient as basal surfaces curved during wounding, making a BM marker necessary. Curvature analysis revealed rounded basal edges in Integrin DN wounds, suggesting that BM influences cell shape. While BM adhesion is not essential for closure, altered cell shape may affect actomyosin interactions. Junctional recoil and lateral ablations would be useful in the future to assess tissue tension and LC contractility. Further perturbation experiments targeting cell adhesion to the BM, for example, Integrin knockdowns, RGDS treatment or Talin autoinhibition mutants, may clarify how IAC stability affects wound healing.

I explored the role of the basement membrane in wound healing by physically removing the BM from the wound site by laser ablation. While quantification of cell shape in additional BM-ablated wounded wing discs is necessary, I observed that healing cells were more rounded in BM-ablated wounds, alluding to the BM's possible roles in maintaining tension in wing disc cells. It would also be interesting to perturb the BM genetically or chemically and examine if this changes 3D cell shape during wound healing in other ways. With genetic perturbations, cells have more time to adapt to their perturbed BM and may adapt wound healing mechanisms accordingly. While using chemical treatments to remove the BM would be more acute.

7.5 Outlook

Talin knockdown and Integrin DN did not significantly affect wound closure rate, suggesting that the requirement for Talin and Integrin is less in these tall cells than shown in other *Drosophila* tissues [129,258,259]. While most wounds eventually close, how they close may differ depending on their mechanical properties and initial cell geometry. Furthermore, imaging should extend beyond 120 min to capture late-stage differences in wound closure.

Overall, the perturbations presented in this thesis are complex to interpret, as myosin, the key driver of cell contractility and cell shape change, functions across all cell domains, making it difficult to isolate specific effects when perturbed (Figure 7.1.A). Additionally, wound quantifications are interdependent, and genetic perturbations often affect multiple metrics simultaneously, complicating analysis (Figure 7.1.B). To fully address the questions posed in this thesis, further analysis of basolateral dynamics is required. Key next steps include direct investigation of basal actomyosin network dynamics during wound healing and comprehensive characterisation of full apicobasal cell shape, including basal domains (Figure 7.1.C-F).

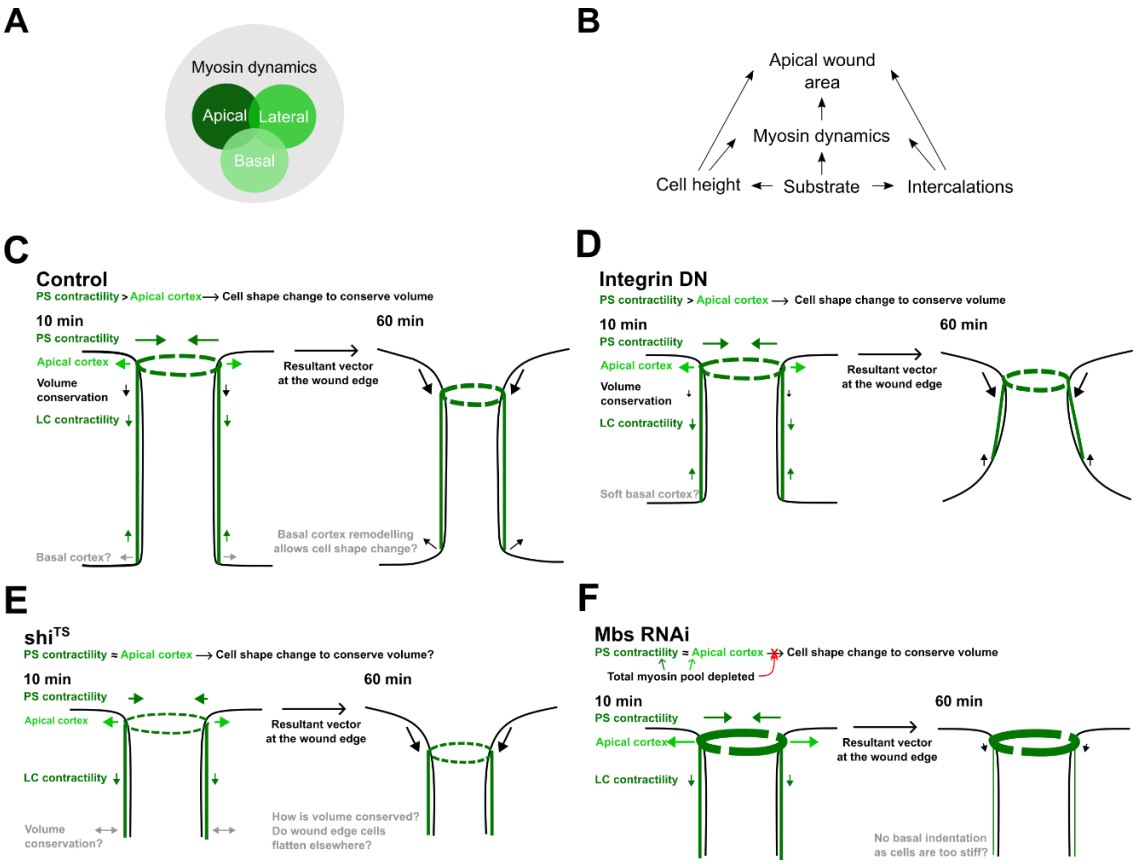

Figure 7.1: Summary of wound healing mechanisms in control and perturbed wounds.

A) Apical, lateral, and basal actomyosin networks derive from the same myosin pool in the cell. B) Wound quantifications are interdependent, and often, genetic perturbations affect more than one metric concurrently. Summaries of 3D wound healing mechanisms using data from this thesis: C) Control, D) Integrin DN, E) *shi*^{TS}, F) Mbs RNAi. Grey text indicates ongoing questions for future investigation.

Alternatively, to explain the delay in basal deformation, LC myosin intensity may increase in basolateral regions as healing progresses (Figure 7.2). Current imaging only quantifies the first 10 µm of the cable. Further experiments quantifying cable homogeneity in control wounds will be carried out. Laser parameters will be optimised to capture the full apicobasal cable, but to avoid oversaturation of the myosin-GFP signal due to the purse string, the apical surface of the wound will be cropped and excluded for cable analysis. Furthermore, these intensity measurements will be normalised for fluorescence attenuation by co-imaging a cell membrane marker simultaneously. This membrane marker will act as a reference to calculate a light attenuation factor with z-depth.

These myosin intensity measurements will indicate whether there is a higher proportion of active LC filaments in any regions of the cable. However, instead, myosin intensity could be homogenous along the cable, but myosin turnover could be modulated. Delayed basal deformation could be due to a change in myosin turnover at the basolateral regions of the cable. Fluorescence Recovery After Photobleaching could be used to investigate myosin turnover in the lateral domains of the wing disc during wound healing.

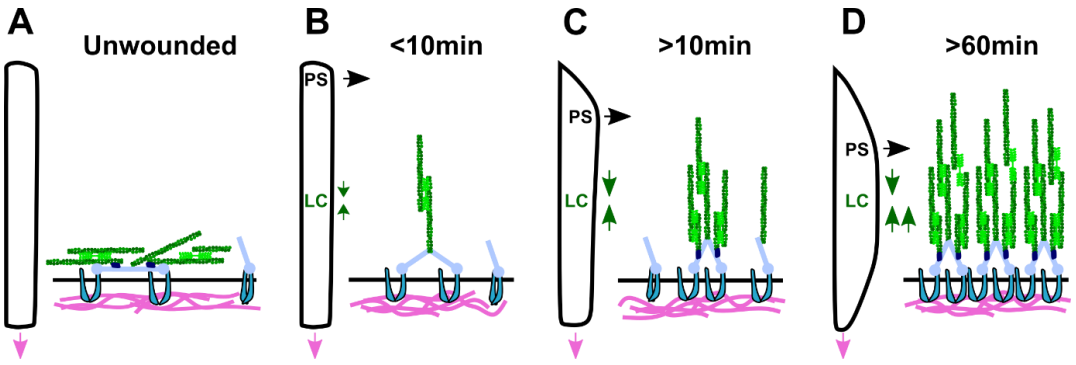

Figure 7.2: Proposed alternative mechanism of lateral cable regulation from IACs on the basal surface.

Forces outside of the LCs and BM, for example, maintaining cortical tension, are not shown for clarity. A) Unwounded cell (left) and section of the basal membrane and IACs (right). Some IACs maintain the basal tension with the BM and basal actomyosin cortex, and some IACs may be unbound to the actomyosin cytoskeleton. Talin is parallel to the cell membrane. B) Wound edge cell shape in the first 10 min of wounding (left), the PS forms exerting a pulling force towards the wound gap, and the lateral cables start to form (right). Talin is pulled into a perpendicular but the assembling lateral cables. C) 10 min post-wounding, the apical surface of the wound-edge cell has noticeable indentation (left), and stable lateral cables have formed (right). D) 60 min post-wounding, the apical surface of the wound edge cell has reached maximum indentation that the apical cell membrane will allow (left). The basal surface starts to indent as the lateral cables pull on the apical surface (right). There are now enough IACs bound to the BM and lateral cables to generate enough tension to overcome resistance from the BM. Green represents myosin filaments, dark blue for vinculin, pastel blue for talin, blue for Integrin, and pink for the BM.

While conclusive outcomes for the aims posed in Chapter 1.5 are ongoing, the work so far has made considerable progress in the exploration of 3D cell shape behaviour during wound healing and key developments into a novel lateral actomyosin cable structure discovered by Dr Rob Tetley in the lab. It has paved the way for future experiments by optimising experimental techniques and analysis methods. The next step, which is currently in progress, is the continuation of the LC regulator screening. Identifying a molecular regulator or an alternative method to abolish lateral cable formation is essential for testing the proposed cell shortening hypothesis.

Despite advances in live imaging allowing long-term timelapses of wound healing to be acquired, the next bottleneck is efficiently analysing this 4D data. A major challenge is bridging the scales between subcellular cytoskeletal structures and tissue-level 3D deformations during healing. Segmentation of complete cells in wounded wing discs was a major

bottleneck in the analysis. Furthermore, this work has highlighted the need for timelapse imaging of the basal surface during wound closure. The apical and basal domains of cells must be considered together in 3D cell shape analysis. Developments in AI-driven segmentation are promising solutions to this bottleneck, including the recently released Cellpose 3.0 [289]. The current ongoing experiments to quantify cell height and basal deformation are being performed. Additionally, imaging of the basal actomyosin networks in unwounded, wounded, and perturbed wing discs will be performed.

Regarding the role of the BM in wound healing, physical laser ablation experiments are being optimised. Furthermore, fly lines have been generated to facilitate the expression of BM or MMP perturbations in mosaic clones. Together with the previously discussed improvements in imaging the basal surface of wounds, these experiments will reveal new insights into the role of the BM in wound healing. *Drosophila* wing discs are powerful models for this research, bridging well-studied cell-culture systems and 3D wound repair *in vivo*.

Researching the mechanical forces driving wound healing is likely to lead to the development of novel methods to improve impaired wound healing or advance post-surgery recovery. Furthermore, we can gain valuable insights into the complex interplay between tissue mechanics and cancer progression. This includes ways to edit the physical properties of cells or BM and design scaffolds or targeted treatments, such as dressings or sutures.

8 Appendices

8.1 Basal surface of Talin immunostainings

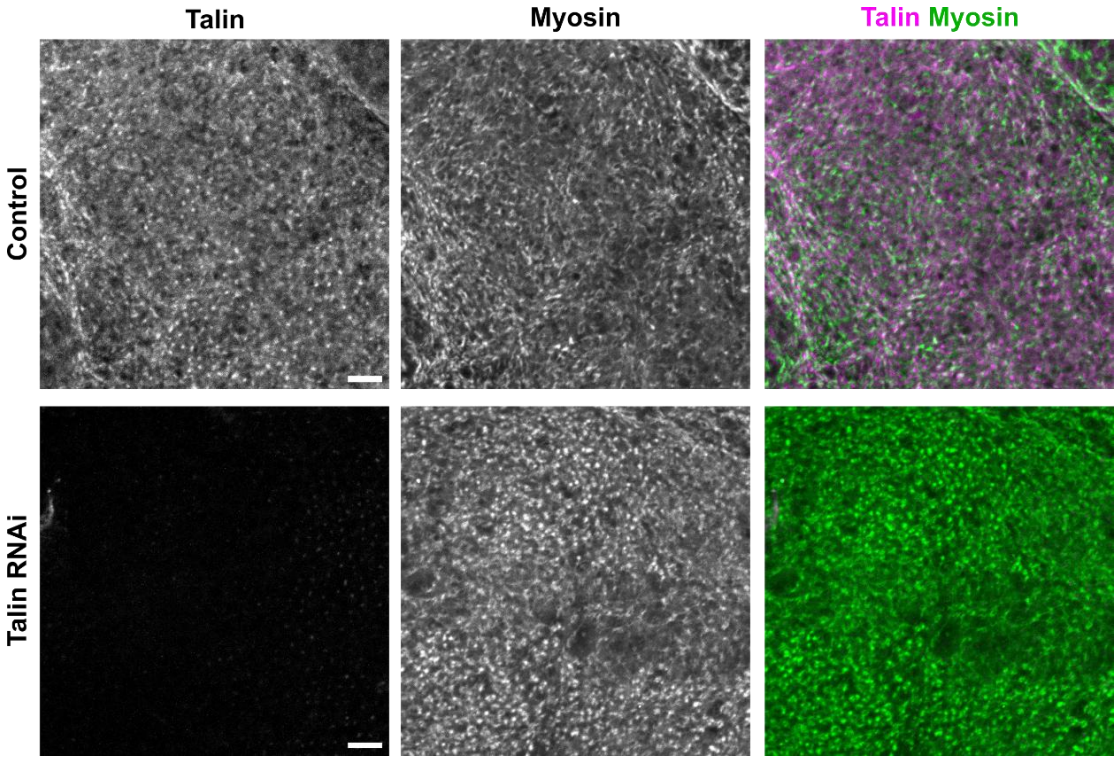

Figure 8.1: Maximum projection of the basal surface of control and Talin RNAi immunostained wing discs.

Talin puncta appear as doughnut-shaped puncta with radial astral projections in the control. Some Talin puncta in the Talin RNAi disc appear similar to the control, but there are also round, filled circular puncta.

8.2 Individual curve fits

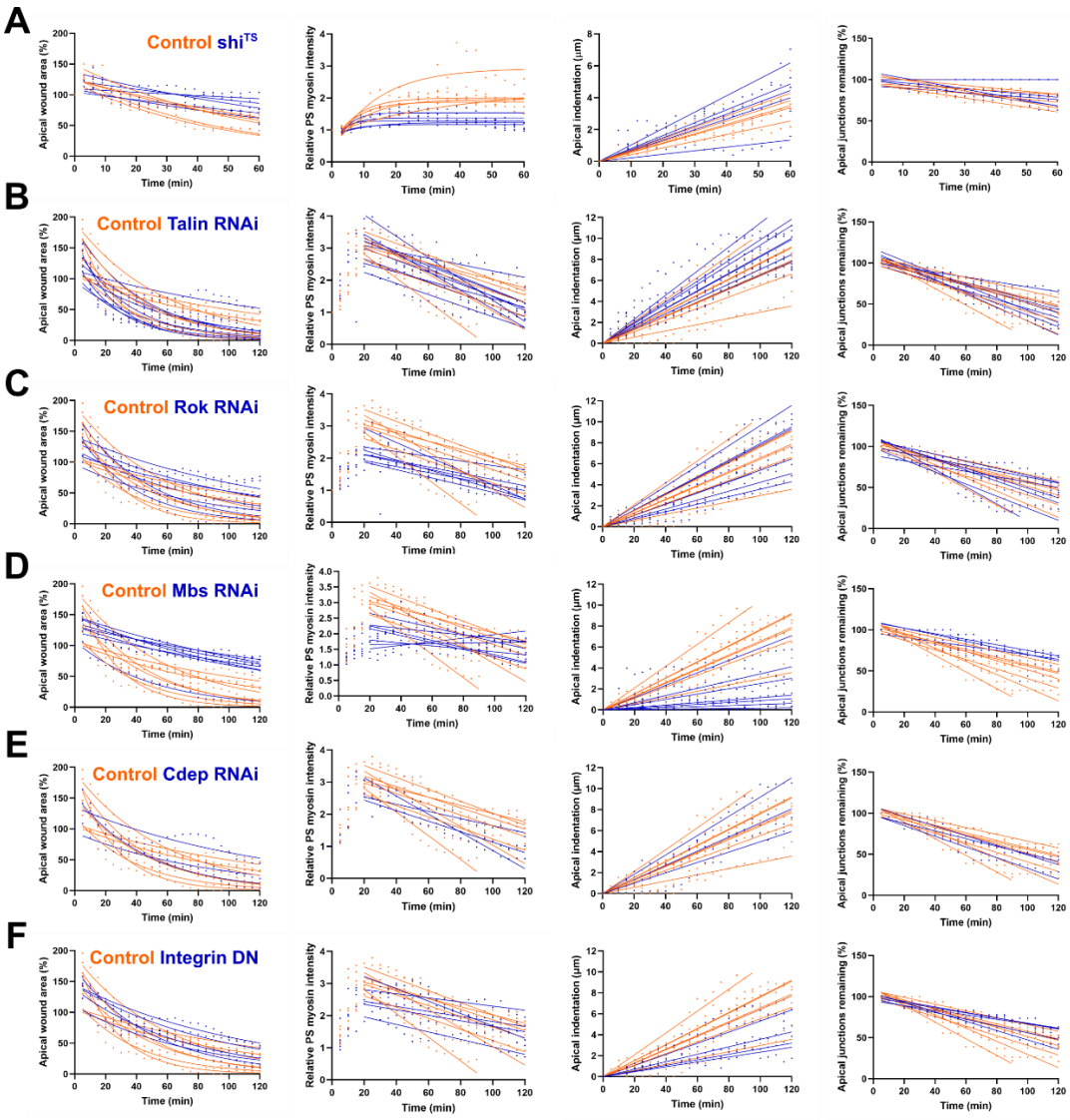

Figure 8.2: Individual non-linear curve fits.

From left to right: wound area (one-phase decay, Equation 1), relative mean PS myosin intensity (A: one-phase association, Equation 2 and straight-line, Equation 3 for others), apical indentation (straight-line, Equation 3), and junctions remaining (straight-line, Equation 3) over time for: A) Temperature shifted control (n=5, orange) and shi^{TS} (n=5, blue) wounds; B) Control (n=7, orange) and Talin RNAi (n=9, blue); C) Control (n=7, orange) and Rok RNAi (n=7, blue); D) Control (n=7, orange) and Mbs RNAi (n=7, blue); E) Control (n=7, orange) and Cdep RNAi (n=3, blue); F) Control (n=7, orange) and Integrin DN (n=5, blue).

References

1. Guest JF, Fuller GW, Vowden P: Cohort study evaluating the burden of wounds to the UK's National Health Service in 2017/2018: Update from 2012/2013. *BMJ Open* 2020, 10.

2. Vrana NE, Lavalle P, Dokmeci MR, Dehghani F, Ghaemmaghami AM, Khademhosseini A: Engineering functional epithelium for regenerative medicine and in vitro organ models: A review. *Tissue Eng Part B Rev* 2013, 19:529–543.

3. Lemke SB, Nelson CM: Dynamic changes in epithelial cell packing during tissue morphogenesis. *Current Biology* 2021, 31:R1098–R1110.

4. Mandriota N, Friedsam C, Jones-Molina JA, Tatem K V, Ingber DE, Sahin O: Cellular nanoscale stiffness patterns governed by intracellular forces. *Nat Mater* 2019, 18:1071–1077.

5. Bergert M, Erzberger A, Desai RA, Aspalter IM, Oates AC, Charras G, Salbreux G, Paluch EK: Force transmission during adhesion-independent migration. *Nat Cell Biol* 2015, 17:524–529.

6. Mason FM, Tworoger M, Martin AC: Apical domain polarization localizes actin–myosin activity to drive ratchet-like apical constriction. *Nat Cell Biol* 2013, 15:926–936.

7. Chugh P, Paluch EK: The actin cortex at a glance. *J Cell Sci* 2018, 131:jcs186254.

8. Jiang H, Sun SX: Cellular Pressure and Volume Regulation and Implications for Cell Mechanics. *Biophys J* 2013, 105:609–619.

9. Wu Y, Sun SX: Mechanics of cell-cell junctions. *Biophys J* 2023, 122:3354–3368.

10. Niessen CM: Tight junctions/adherens junctions: Basic structure and function. *Journal of Investigative Dermatology* 2007, 127:2525–2532.

11. Kechagia JZ, Ivaska J, Roca-Cusachs P: Integrins as biomechanical sensors of the microenvironment. *Nat Rev Mol Cell Biol* 2019, 20:457–473.

12. Murrell M, Oakes PW, Lenz M, Gardel ML: Forcing cells into shape: The mechanics of actomyosin contractility. *Nat Rev Mol Cell Biol* 2015, 16:486–498.

13. Dominguez R, Holmes KC: Actin structure and function. *Annu Rev Biophys* 2011, 40:169–186.

14. Newell-Litwa KA, Horwitz R, Lamers ML: Non-Muscle myosin II in disease: Mechanisms and therapeutic opportunities. *DMM Disease Models and Mechanisms* 2015, 8:1495–1515.

15. Tyska MJ, Warshaw DM: The Myosin Power Stroke. 2002, doi:10.1002/cmc.10014.

16. Freeman M, Vasquez CG, Heissler SM, Billington N, Sellers JR, Martin AC: Drosophila non-muscle myosin II motor activity determines the rate of tissue folding. 2016, doi:10.7554/eLife.20828.001.

17. Amano M, Ito M, Kimura K, Fukata Y, Chihara K, Nakano T, Matsuura Y, Kaibuchi K: Phosphorylation and activation of myosin by Rho-associated kinase (Rho- kinase). *Journal of Biological Chemistry* 1996, 271:20246–20249.

18. Kishi Hiroko and Ye L-H and NA and OT and IA and TT and KK: Structure and Function of Smooth Muscle Myosin Light Chain Kinase. In *Mechanisms of Work Production and Work Absorption in Muscle*. Edited by Sugi Haruo and Pollack GH. Springer US; 1998:229–234.

19. Champagne MB, Edwards KA, Erickson HP, Kiehart DP: Drosophila stretchin-MLCK is a novel member of the Titin/Myosin light chain kinase family. *J Mol Biol* 2000, 300:759–777.

20. Hartshorne DJ: Myosin phosphatase: subunits and interactions. *Acta Physiol Scand* 1998, 164:483–493.

21. Chetty AK, Ha BH, Boggon TJ: Rho family GTPase signaling through type II p21-activated kinases. *Cellular and Molecular Life Sciences* 2022, 79.

22. Etienne-Manneville S, Hall A: *Rho GTPases in cell biology*. 2002.

23. Hall A: Rho GTPases and the Actin Cytoskeleton. *Science (1979)* 1998, 279:509–514.

24. Kühn S, Geyer M: Formins as effector proteins of rho GTPases. *Small GTPases* 2014, 5.

25. Lessey LR, Robinson SC, Chaudhary R, Daniel JM: Adherens junction proteins on the move—From the membrane to the nucleus in intestinal diseases. *Front Cell Dev Biol* 2022, 10.

26. Johnson MS, Lu N, Denessiouk K, Heino J, Gullberg D: Integrins during evolution: Evolutionary trees and model organisms. *Biochim Biophys Acta Biomembr* 2009, 1788:779–789.

27. Nishida N, Xie C, Shimaoka M, Cheng Y, Walz T, Springer TA: Activation of Leukocyte β2 Integrins by Conversion from Bent to Extended Conformations. *Immunity* 2006, 25:583–594.

28. Luo B-H, Springer TA: Integrin structures and conformational signaling. *Curr Opin Cell Biol* 2006, 18:579–586.

29. Klapholz B, Brown NH: Talin - The master of integrin adhesions. *J Cell Sci* 2017, 130:2435–2446.

30. Hemmings L, Rees DJG, Ohanian V, Bolton SJ, Gilmore AP, Patel B, Priddle H, Trevithick JE, Hynes RO, Critchley DR: Talin contains three actin-binding sites each of which is adjacent to a vinculin-binding site. *J Cell Sci* 1996, 109:2715–2726.

31. Goult BT, Xu XP, Gingras AR, Swift M, Patel B, Bate N, Kopp PM, Barsukov IL, Critchley DR, Volkmann N, et al.: Structural studies on full-length talin1 reveal a compact auto-inhibited dimer: Implications for talin activation. *J Struct Biol* 2013, 184:21–32.

32. Bromberger T, Zhu L, Klapproth S, Qin J, Moser M: Rap1 and membrane lipids cooperatively recruit talin to trigger integrin activation. *J Cell Sci* 2019, 132.

33. Ye X, McLean MA, Sligar SG: Conformational equilibrium of talin is regulated by anionic lipids. *Biochim Biophys Acta Biomembr* 2016, 1858:1833–1840.

34. Yao M, Goult BT, Klapholz B, Hu X, Toseland CP, Guo Y, Cong P, Sheetz MP, Yan J: The mechanical response of talin. *Nat Commun* 2016, 7.

35. Fischer LS, Klingner C, Schlichthaerle T, Strauss MT, Böttcher R, Fässler R, Jungmann R, Grashoff C: Quantitative single-protein imaging reveals molecular complex formation of integrin, talin, and kindlin during cell adhesion. *Nat Commun* 2021, 12.

36. Fidler AL, Darris CE, Chetyrkin S V., Pedchenko VK, Boudko SP, Brown KL, Gray Jerome W, Hudson JK, Rokas A, Hudson BG: Collagen iv and basement membrane at the evolutionary dawn of metazoan tissues. *Elife* 2017, 6.

37. Yurchenco PD: Basement membranes: Cell scaffoldings and signaling platforms. *Cold Spring Harb Perspect Biol* 2011, 3:1–27.

38. Töpfer U: Basement membrane dynamics and mechanics in tissue morphogenesis. *Biol Open* 2023, 12.

39. Hynes RO: The evolution of metazoan extracellular matrix. *Journal of Cell Biology* 2012, 196:671–679.

40. Nagase H, Visse R, Murphy G: Structure and function of matrix metalloproteinases and TIMPs. *Cardiovasc Res* 2006, 69:562–573.

41. Cabral-Pacheco GA, Garza-Veloz I, Rosa CCD La, Ramirez-Acuña JM, Perez-Romero BA, Guerrero-Rodriguez JF, Martinez-Avila N, Martinez-Fierro ML: The roles of matrix metalloproteinases and their inhibitors in human diseases. *Int J Mol Sci* 2020, 21:1–53.

42. Ding X, Kakanj P, Leptin M, Eming SA: Regulation of the Wound Healing Response during Aging. *Journal of Investigative Dermatology* 2021, 141:1063–1070.

43. Gould L, Abadir P, Brem H, Carter M, Conner-Kerr T, Davidson J, Dipietro L, Falanga V, Fife C, Gardner S, et al.: Chronic wound repair and healing in older adults: Current status and future research. *J Am Geriatr Soc* 2015, 63:427–438.

44. Falanga V, Isseroff RR, Soulika AM, Romanelli M, Margolis D, Kapp S, Granick M, Harding K: Chronic wounds. *Nat Rev Dis Primers* 2022, 8.

45. Xue M, Jackson CJ: Extracellular Matrix Reorganization During Wound Healing and Its Impact on Abnormal Scarring. *Adv Wound Care (New Rochelle)* 2015, 4:119–136.

46. Sidgwick GP, Bayat A: Extracellular matrix molecules implicated in hypertrophic and keloid scarring. *Journal of the European Academy of Dermatology and Venereology* 2012, 26:141–152.

47. Derkacz A, Olczyk P, Olczyk K, Komosinska-Vassev K: The role of extracellular matrix components in inflammatory bowel diseases. *J Clin Med* 2021, 10:1–15.

48. Herrera J, Henke CA, Bitterman PB: Extracellular matrix as a driver of progressive fibrosis. *Journal of Clinical Investigation* 2018, 128:45–53.

49. Iredale JP, Thompson A, Henderson NC: Extracellular matrix degradation in liver fibrosis: Biochemistry and regulation. *Biochim Biophys Acta Mol Basis Dis* 2013, 1832:876–883.

50. Hsu CK, Lin HH, Harn HI, Ogawa R, Wang YK, Ho YT, Chen WR, Lee YC, Lee JYY, Shieh SJ, et al.: Caveolin-1 Controls Hyperresponsiveness to Mechanical Stimuli and Fibrogenesis-Associated RUNX2 Activation in Keloid Fibroblasts. *Journal of Investigative Dermatology* 2018, 138:208–218.

51. Larson BJ, Longaker MT, Lorenz HP: Scarless fetal wound healing: A basic science review. *Plast Reconstr Surg* 2010, 126:1172–1180.

52. Rowlatt U: *A rhiv A Intrauterine Wound Healing in a 20 Week Human Fetus*. 1979.

53. Frazier Frantz BW, Bettinger DA, Haynes JH, Johnson DE, Harvey KM, Dalton HP, Yager DR, Diegelmann RF, Kelman Cohen Richmond I: *Biology of Fetal Repair: The Presence of Bacteria in Fetal Wounds Induces an Adult-Like Healing Response*. 1993.

54. Rogers KW, Schier AF: Morphogen gradients: From generation to interpretation. *Annu Rev Cell Dev Biol* 2011, 27:377–407.

55. Gurdon JB, Bourillot P-Y: *Morphogen gradient interpretation*. 2001.

56. Zallen JA: Planar Polarity and Tissue Morphogenesis. *Cell* 2007, 129:1051–1063.

57. Bailles A, Collinet C, Philippe JM, Lenne PF, Munro E, Lecuit T: Genetic induction and mechanochemical propagation of a morphogenetic wave. *Nature* 2019, 572:467–473.

58. Lecuit T, Lenne PF, Munro E: Force generation, transmission, and integration during cell and tissue morphogenesis. *Annu Rev Cell Dev Biol* 2011, 27:157–184.

59. Mao Y, Tournier AL, Hoppe A, Kester L, Thompson BJ, Tapon N: Differential proliferation rates generate patterns of mechanical tension that orient tissue growth. *EMBO Journal* 2013, 32:2790–2803.

60. LeGoff L, Rouault H, Lecuit T: A global pattern of mechanical stress polarizes cell divisions and cell shape in the growing Drosophila wing disc. *Development (Cambridge)* 2013, 140:4051–4059.

61. Guo S, DiPietro LA: Critical review in oral biology & medicine: Factors affecting wound healing. *J Dent Res* 2010, 89:219–229.

62. Wilkinson HN, Hardman MJ: Wound healing: cellular mechanisms and pathological outcomes: Cellular Mechanisms of Wound Repair. *Open Biol* 2020, 10.

63. Velnar T, Bailey T, Smrkolj V: *The Wound Healing Process: an Overview of the Cellular and Molecular Mechanisms*. 2009.

64. Brugués A, Anon E, Conte V, Veldhuis JH, Gupta M, Colombelli J, Muñoz JJ, Brodland GW, Ladoux B, Trepat X: Forces driving epithelial wound healing. *Nat Phys* 2014, 10:683–690.

65. Suraneni P, Rubinstein B, Unruh JR, Durnin M, Hanein D, Li R: The Arp2/3 complex is required for lamellipodia extension and directional fibroblast cell migration. *Journal of Cell Biology* 2012, 197:239–251.

66. Anon E, Serra-Picamal X, Hersen P, Gauthier NC, Sheetz MP, Trepat X, Ladoux B: Cell crawling mediates collective cell migration to close undamaged epithelial gaps. *Proc Natl Acad Sci U S A* 2012, 109:10891–10896.

67. Farooqui R, Fenteany G: Multiple rows of cells behind an epithelial wound edge extend cryptic lamellipodia to collectively drive cell-sheet movement. *J Cell Sci* 2005, 118:51–63.

68. Matsubayashi Y, Razzell W, Martin P: “White wave” analysis of epithelial scratch wound healing reveals how cells mobilise back from the leading edge in a myosin-II-dependent fashion. *J Cell Sci* 2011, 124:1017–1021.

69. Lee C, Hong SN, Kim ER, Chang DK, Kim YH: Epithelial regeneration ability of crohn’s disease assessed using patient-derived intestinal organoids. *Int J Mol Sci* 2021, 22.

70. Kong J, Wen S, Cao W, Yue P, Xu X, Zhang Y, Luo L, Chen T, Li L, Wang F, et al.: Lung organoids, useful tools for investigating epithelial repair after lung injury. *Stem Cell Res Ther* 2021, 12.

71. Montenegro-Miranda PS, van der Meer JHM, Jones C, Meisner S, Vermeulen JLM, Koster J, Wildenberg ME, Heijmans J, Boudreau F, Ribeiro A, et al.: A Novel Organoid Model of Damage and Repair Identifies HNF4α as a Critical Regulator of Intestinal Epithelial Regeneration. *CMGH* 2020, 10:209–223.

72. Castro N, Gillespie SR, Bernstein AM: Ex Vivo Corneal Organ Culture Model for Wound Healing Studies. *Journal of Visualized Experiments* 2019, doi:10.3791/58562.

73. Richardson R, Metzger M, Knyphausen P, Ramezani T, Slanchev K, Kraus C, Schmelzer E, Hammerschmidt M: Re-epithelialization of cutaneous wounds in adult zebrafish combines mechanisms of wound closure in embryonic and adult mammals. *Development (Cambridge)* 2016, 143:2077–2088.

74. Kamran Z, Zellner K, Kyriazes H, Kraus CM, Reynier JB, Malamy JE: In vivo imaging of epithelial wound healing in the cnidarian Clytia hemisphaerica demonstrates early evolution of purse string and cell crawling closure mechanisms. *BMC Dev Biol* 2017, 17.

75. Tsai CR, Wang Y, Galko MJ: Crawling wounded: Molecular genetic insights into wound healing from drosophila larvae. *International Journal of Developmental Biology* 2018, 62:479–489.

76. Brock J, Midwinter K, Lewis J, Martin P: Healing of Incisional Wounds in the Embryonic Chick Wing Bud: Characterization of the Actin Purse-String and Demonstration of a Requirement for Rho Activation. *J Cell Biol* 1996, 135:1097–1107.

77. Davidson LA, Ezin AM, Keller R: Embryonic wound healing by apical contraction and ingression in Xenopus laevis. *Cell Motil Cytoskeleton* 2002, 53:163–176.

78. Clark AG, Miller AL, Vaughan E, Yu HYE, Penkert R, Bement WM: Integration of Single and Multicellular Wound Responses. *Current Biology* 2009, 19:1389–1395.

79. O'Connor J, Akbar FB, Hutson MS, Page-McCaw A: Zones of cellular damage around pulsed-laser wounds. *PLoS One* 2021, 16.

80. Begnaud S, Chen T, Delacour D, Mège RM, Ladoux B: Mechanics of epithelial tissues during gap closure. *Curr Opin Cell Biol* 2016, 42:52–62.

81. Enyedi B, Niethammer P: Mechanisms of epithelial wound detection. *Trends Cell Biol* 2015, 25:398–407.

82. Naomi Handly L, Wollman R: Wound-induced Ca2+ wave propagates through a simple release and diffusion mechanism. *Mol Biol Cell* 2017, 28:1457–1466.

83. Xu S, Chisholm AD: A Gαq-Ca2+ signaling pathway promotes actin-mediated epidermal wound closure in C. elegans. *Current Biology* 2011, 21:1960–1967.

84. Han I, Hua J, White JS, O'connor JT, Nassar LS, Tro KJ, Page-Mccaw A, Hutson MS: After wounding, a G-protein coupled receptor promotes the restoration of tension in epithelial cells. *bioRxiv* 2024, doi:10.1101/2023.05.31.543122.

85. Restrepo S, Basler K: Drosophila wing imaginal discs respond to mechanical injury via slow InsP 3 R-mediated intercellular calcium waves. *Nat Commun* 2016, 7.

86. Russo JM, Florian P, Shen LE, Vallen Graham W, Tretiakova MS, Gitter AH, Mrsny ¶ RJ, Turner JR: Distinct Temporal-Spatial Roles for Rho Kinase and Myosin Light Chain Kinase in Epithelial Purse-String Wound Closure. *Gastroenterology* 2005, 128:987–1001.

87. Abreu-Blanco MT, Verboon JM, Liu R, Watts JJ, Parkhurst SM: Drosophila embryos close epithelial wounds using a combination of cellular protrusions and an actomyosin purse string. *J Cell Sci* 2012, 125:5984–5997.

88. Wood W, Jacinto A, Grose R, Woolner S, Gale J, Wilson C, Martin P: Wound healing recapitulates morphogenesis in Drosophila embryos. *Nat Cell Biol* 2002, 4:907–912.

89. Bement WM, Mandato CA, Kirsch MN: Wound-induced assembly and closure of an actomyosin purse string in Xenopus oocytes. *Current Biology* 1999, 9:579–587.

90. Becker KA, Hart NH: Reorganization of filamentous actin and myosin-II in zebrafish eggs correlates temporally and spatially with cortical granule exocytosis. *J Cell Sci* 1999, 112:97–110.

91. Gault WJ, Enyedi B, Niethammer P: Osmotic surveillance mediates rapid wound closure through nucleotide release. *Journal of Cell Biology* 2014, 207:767–782.

92. Danjo Y, Gipson IK: Actin 'purse string' filaments are anchored by E-cadherin-mediated adherens junctions at the leading edge of the epithelial wound, providing coordinated cell movement. *J Cell Sci* 1998, 111:3323–3332.

93. Zulueta-Coarasa T, Fernandez-Gonzalez R: Tension (re)builds: Biophysical mechanisms of embryonic wound repair. *Mech Dev* 2017, 144:43–52.

94. Kobb AB, Zulueta-Coarasa T, Fernandez-Gonzalez R: Tension regulates myosin dynamics during Drosophila embryonic wound repair. *J Cell Sci* 2017, 130:689–696.

95. Xu H, Huo Y, Zhou Q, Wang LA, Cai P, Doss B, Huang C, Hsia KJ: Geometry-mediated bridging drives nonadhesive stripe wound healing. *Proc Natl Acad Sci U S A* 2023, 120.

96. Gov NS: Guided by curvature: Shaping cells by coupling curved membrane proteins and cytoskeletal forces. *Philosophical Transactions of the Royal Society B: Biological Sciences* 2018, 373.

97. Matsubayashi Y, Coulson-Gilmer C, Millard TH: Endocytosis-dependent coordination of multiple actin regulators is required for wound healing. *Journal of Cell Biology* 2015, 210:419–433.

98. Stjepić V, Nakamura M, Hui J, Parkhurst SM: Two Septin complexes mediate actin dynamics during cell wound repair. *Cell Rep* 2024, 43.

99. Danjo Y, Gipson IK: Actin 'purse string' filaments are anchored by E-cadherin-mediated adherens junctions at the leading edge of the

epithelial wound, providing coordinated cell movement. *J Cell Sci* 1998, 111:3323–3332.

100. Magie CR, Pinto-Santini D, Parkhurst SM: Rho1 interacts with p120ctn and α-catenin, and regulates cadherin-based adherens junction components in Drosophila. *Development* 2002, 129:3771–3782.

101. Martin E, Suzanne M: Functions of Arp2/3 Complex in the Dynamics of Epithelial Tissues. *Front Cell Dev Biol* 2022, 10.

102. Ashour DJ, Durney CH, Planelles-Herrero VJ, Stevens TJ, Feng JJ, Röper K: *Zasp52 strengthens whole embryo tissue integrity through supracellular actomyosin networks*. 2023.

103. Hui J, Nakamura M, Dubrulle J, Parkhurst SM: Coordinated efforts of different actin filament populations are needed for optimal cell wound repair. *Mol Biol Cell* 2023, 34:ar15.

104. Tetley RJ, Staddon MF, Heller D, Hoppe A, Banerjee S, Mao Y: Tissue fluidity promotes epithelial wound healing. *Nat Phys* 2019, 15:1195–1203.

105. Razzell W, Wood W, Martin P: Recapitulation of morphogenetic cell shape changes enables wound re-epithelialisation. *Development (Cambridge)* 2014, 141:1814–1820.

106. Symons M, Settleman J: Rho family GTPases: more than simple switches. *Trends Cell Biol* 2000, 10:415–419.

107. Nakamura M, Verboon JM, Parkhurst SM: Prepatterning by RhoGEFs governs Rho GTPase spatiotemporal dynamics during wound repair. *Journal of Cell Biology* 2017, 216:3959–3969.

108. Losick VP, Duhaime LG: The endocycle restores tissue tension in the Drosophila abdomen post wound repair. *Cell Rep* 2021, 37:109827.

109. Losick VP, Fox DT, Spradling AC: Polyploidization and cell fusion contribute to wound healing in the adult Drosophila epithelium. *Curr Biol* 2013, 23:2224–2232.

110. Scepanovic G, Hunter MV, Kafri R, Fernandez-Gonzalez R: p38-mediated cell growth and survival drive rapid embryonic wound repair. *Cell Rep* 2021, 37:109874.

111. White JS, Su JJ, Ruark EM, Hua J, Hutson MS, Page-McCaw A: Wound-Induced Syncytia Outpace Mononucleate Neighbors during Drosophila Wound Repair. *bioRxiv* 2023, doi:10.1101/2023.06.25.546442.

112. Losick VP, Jun AS, Spradling AC: Wound-Induced Polyploidization: Regulation by Hippo and JNK Signaling and Conservation in Mammals. *PLoS One* 2016, 11:e0151251.

113. Besen-McNally R, Gjelsvik KJ, Losick VP: Wound-induced polyploidization is dependent on Integrin-Yki signaling. *Biol Open* 2021, 10.

114. White JS, Su JJ, Ruark EM, Hua J, Hutson MS, Page-McCaw A: Wound-Induced Syncytia Outpace Mononucleate Neighbors during Drosophila Wound Repair. *bioRxiv* 2023, doi:10.1101/2023.06.25.546442.

115. Dalton S: Linking the Cell Cycle to Cell Fate Decisions. *Trends Cell Biol* 2015, 25:592–600.

116. Zatulovskiy E, Skotheim JM: On the Molecular Mechanisms Regulating Animal Cell Size Homeostasis. *Trends in Genetics* 2020, 36:360–372.

117. Lim SE, Vicente-Munuera P, Mao Y: Forced back into shape: Mechanics of epithelial wound repair. *Curr Opin Cell Biol* 2024, 87.

118. Tamada M, Perez TD, Nelson WJ, Sheetz MP: Two distinct modes of myosin assembly and dynamics during epithelial wound closure. *Journal of Cell Biology* 2007, 176:27–33.

119. Ioannou F, Dawi MA, Tetley RJ, Mao Y, Muñoz JJ: Development of a New 3D Hybrid Model for Epithelia Morphogenesis. *Front Bioeng Biotechnol* 2020, 8.

120. Zehnder SM, Suaris M, Bellaire MM, Angelini TE: Cell volume fluctuations in MDCK monolayers. *Biophys J* 2015, 108:247–250.

121. Sui L, Alt S, Weigert M, Dye N, Eaton S, Jug F, Myers EW, Jülicher F, Salbreux G, Dahmann C: Differential lateral and basal tension drive folding of Drosophila wing discs through two distinct mechanisms. *Nat Commun* 2018, 9.

122. Monier B, Gettings M, Gay G, Mangeat T, Schott S, Guarner A, Suzanne M: Apico-basal forces exerted by apoptotic cells drive epithelium folding. *Nature* 2015, 518:245–248.

123. Ambrosini A, Rayer M, Monier B, Suzanne M: Mechanical Function of the Nucleus in Force Generation during Epithelial Morphogenesis. *Dev Cell* 2019, 50:197-211.e5.

124. Sun Z, Amourda C, Shagirov M, Hara Y, Saunders TE, Toyama Y: Basolateral protrusion and apical contraction cooperatively drive Drosophila germ-band extension. *Nat Cell Biol* 2017, 19:375–383.

125. Abreu-Blanco MT, Watts JJ, Verboon JM, Parkhurst SM: Cytoskeleton responses in wound repair. *Cellular and Molecular Life Sciences* 2012, 69:2469–2483.

126. Khalilgharibi N, Mao Y: To form and function: On the role of basement membrane mechanics in tissue development, homeostasis and disease. *Open Biol* 2021, 11.

127. Shellard A, Mayor R: Sculpting with stiffness: rigidity as a regulator of morphogenesis. *Biochem Soc Trans* 2023, 51:1009–1021.

128. Ajeti V, Tabatabai AP, Fleszar AJ, Staddon MF, Seara DS, Suarez C, Yousafzai MS, Bi D, Kovar DR, Banerjee S, et al.: Wound healing coordinates actin architectures to regulate mechanical work. *Nat Phys* 2019, 15:696–705.

129. Ly M, Schimmer C, Hawkins R, Rothenberg K, Fernandez-Gonzalez R: Integrin-based adhesions promote cell-cell junction and cytoskeletal

remodelling to drive embryonic wound healing. *J Cell Sci* 2023, doi:10.1242/jcs.261138.

130. Pereira AM, Tudor C, Kanger JS, Subramaniam V, Martin-Blanco E: Integrin-dependent activation of the jnk signaling pathway by mechanical stress. *PLoS One* 2011, 6.

131. Wang Y, Antunes M, Anderson AE, Kadrmas JL, Jacinto A, Galko MJ: Integrin Adhesions Suppress Syncytium Formation in the Drosophila Larval Epidermis. *Current Biology* 2015, 25:2215–2227.

132. Lee EEL, Watto E, Malamy J: Characterizing Epithelial Wound Healing In Vivo Using the Cnidarian Model Organism Clytia hemisphaerica. *Journal of Visualized Experiments* 2023, 2023.

133. Pal-Ghosh S, Pajoohesh-Ganji A, Tadvalkar G, Stepp MA: Removal of the basement membrane enhances corneal wound healing. *Exp Eye Res* 2011, 93:927–936.

134. Yu W, Datta A, Leroy P, O'brien LE, Mak G, Jou T-S, Matlin KS, Mostov KE, Zegers MMP: Beta1-integrin orients epithelial polarity via Rac1 and laminin. *Mol Biol Cell* 2005, 16:433–445.

135. O'brien LE, Jou T-S, Pollack AL, Zhang Q, Hansen SH, Yurchenco P, Mostov KE: *Rac1 orientates epithelial apical polarity through effects on basolateral laminin assembly*. 2001.

136. Peglion F, Etienne-Manneville S: Cell polarity changes in cancer initiation and progression. *Journal of Cell Biology* 2024, 223.

137. Chang J, Chaudhuri O: Beyond proteases: Basement membrane mechanics and cancer invasion. *Journal of Cell Biology* 2019, 218:2456–2469.

138. Partanen JI, Tervonen TA, Klefström J: Breaking the epithelial polarity barrier in cancer: The strange case of LKB1/PAR-4. *Philosophical Transactions of the Royal Society B: Biological Sciences* 2013, 368.

139. Lee JL, Streuli CH: Integrins and epithelial cell polarity. *J Cell Sci* 2014, 127:3217–3225.

140. Walter C, Davis JT, Mathur J, Pathak A: Physical defects in basement membrane-mimicking collagen-IV matrices trigger cellular EMT and invasion. *Integrative Biology (United Kingdom)* 2018, 10:342–355.

141. Dvorak HF: Tumors: Wounds That Do Not Heal. *New England Journal of Medicine* 1986, 315:1650–1659.

142. Dvorak HF: Tumors: Wounds that do not heal-redux. *Cancer Immunol Res* 2015, 3:1–11.

143. Haigo SL, Bilder D: Global tissue revolutions in a morphogenetic movement controlling elongation. *Science (1979)* 2011, 331:1071–1074.

144. Pastor-Pareja JC, Xu T: Shaping Cells and Organs in Drosophila by Opposing Roles of Fat Body-Secreted Collagen IV and Perlecan. *Dev Cell* 2011, 21:245–256.

145. Ma M, Cao X, Dai J, Pastor-Pareja JC: Basement Membrane Manipulation in Drosophila Wing Discs Affects Dpp Retention but Not Growth Mechanoregulation. *Dev Cell* 2017, 42:97-106.e4.

146. Domínguez-Giménez P, Brown NH, Martín-Bermudo MD: Integrin-ECM interactions regulate the changes in cell shape driving the morphogenesis of the Drosophila wing epithelium. *J Cell Sci* 2007, 120:1061–1071.

147. Ramos-Lewis W, Page-McCaw A: Basement membrane mechanics shape development: Lessons from the fly. *Matrix Biology* 2019, 75–76:72–81.

148. Tozluoğlu M, Duda M, Kirkland NJ, Barrientos R, Burden JJ, Muñoz JJ, Mao Y: Planar Differential Growth Rates Initiate Precise Fold Positions in Complex Epithelia. *Dev Cell* 2019, 51:299-312.e4.

149. Nematbakhsh A, Levis M, Kumar N, Chen W, Zartman JJ, Alber M: Epithelial organ shape is generated by patterned actomyosin contractility and maintained by the extracellular matrix. *PLoS Comput Biol* 2020, 16.

150. Molè MA, Galea GL, Rolo A, Weberling A, Nychyk O, De Castro SC, Savery D, Fässler R, Ybot-González P, Greene NDE, et al.: Integrin-Mediated Focal Anchorage Drives Epithelial Zippering during Mouse Neural Tube Closure. *Dev Cell* 2020, 52:321-334.e6.

151. Luschnig S, Sanchez-Corrales YE, Blanchard GB, Rö Per K: Radially patterned cell behaviours during tube budding from an epithelium. 2018, doi:10.7554/eLife.35717.001.

152. Gómez-Gálvez P, Vicente-Munuera P, Tagua A, Forja C, Castro AM, Letrán M, Valencia-Expósito A, Grima C, Bermúdez-Gallardo M, Serrano-Pérez-Higueras Ó, et al.: Scutoids are a geometrical solution to three-dimensional packing of epithelia. *Nat Commun* 2018, 9.

153. Smith-Bolton R: Drosophila Imaginal Discs as a Model of Epithelial Wound Repair and Regeneration. *Adv Wound Care (New Rochelle)* 2016, 5:251–261.

154. Belacortu Y, Paricio N: Drosophila as a model of wound healing and tissue regeneration in vertebrates. *Developmental Dynamics* 2011, 240:2379–2404.

155. Bryant PJ: Pattern formation in the imaginal wing disc of Drosophila melanogaster: Fate map, regeneration and duplication. *Journal of Experimental Zoology* 1975, 193:49–77.

156. Adler' And PN, Bryant PJ: *Participation of Lethally Irradiated Imaginal Disc Tissue in Pattern Regulation in Drosophila*. 1977.

157. Beira J V., Paro R: The legacy of Drosophila imaginal discs. *Chromosoma* 2016, 125:573–592.

158. Hariharan IK, Serras F: Imaginal disc regeneration takes flight. *Curr Opin Cell Biol* 2017, 48:10–16.

159. Ugur B, Chen K, Bellen HJ: Drosophila tools and assays for the study of human diseases. *DMM Disease Models and Mechanisms* 2016, 9:235–244.

160. Webster N, Rui Jin J, Green S, Hollis M, Chambon P: *The Yeast UASG Is a Transcriptional Enhancer in Human HeLa Cells in the Presence of the GAL4 Trans-Activator*. 1988.

161. Kakidani' H, Ptashne M: *GAL4 Activates Gene Expression in Mammalian Cells*. 1988.

162. Tsao CK, Ku HY, Lee YM, Huang YF, Sun YH: Long term ex vivo culture and live imaging of Drosophila larval imaginal discs. *PLoS One* 2016, 11.

163. Handke B, Szabad J, Lidsky P V., Hafen E, Lehner CF: Towards long term cultivation of Drosophila wing imaginal discs in vitro. *PLoS One* 2014, 9.

164. Aldaz S, Escudero LM, Freeman M: Live imaging of Drosophila imaginal disc development. *Proc Natl Acad Sci U S A* 2010, 107:14217–14222.

165. Smith-Bolton RK, Worley MI, Kanda H, Hariharan IK: Regenerative Growth in Drosophila Imaginal Discs Is Regulated by Wingless and Myc. *Dev Cell* 2009, 16:797–809.

166. Bosch M, Serras F, Martín-Blanco E, Baguñà J: JNK signaling pathway required for wound healing in regenerating Drosophila wing imaginal discs. *Dev Biol* 2005, 280:73–86.

167. Pastor-Pareja JC, Ming W, Tian X: An innate immune response of blood cells to tumors and tissue damage in Drosophila. *DMM Disease Models and Mechanisms* 2008, 1:144–154.

168. Finnson KW, McLean S, Di Guglielmo GM, Philip A: Dynamics of Transforming Growth Factor Beta Signaling in Wound Healing and Scarring. *Adv Wound Care (New Rochelle)* 2013, 2:195–214.

169. Pan D: The hippo signaling pathway in development and cancer. *Dev Cell* 2010, 19:491–505.

170. Diaz-Garcia S, Ahmed S, Baonza A: Analysis of the function of apoptosis during imaginal wing disc regeneration in Drosophila melanogaster. *PLoS One* 2016, 11.

171. Katsuyama T, Paro R: Innate immune cells are dispensable for regenerative growth of imaginal discs. *Mech Dev* 2013, 130:112–121.

172. Díaz-García S, Baonza A: Pattern reorganization occurs independently of cell division during Drosophila wing disc regeneration in situ. *Proceedings of the National Academy of Sciences* 2013, 110:13032–13037.

173. Dye NA, Popović M, Spannl S, Etournay R, Kainmüller D, Ghosh S, Myers EW, Jülicher F, Eaton S: Cell dynamics underlying oriented growth of the drosophila wing imaginal disc. *Development (Cambridge)* 2017, 144:4406–4421.

174. Kumar N, Rangel Ambriz J, Tsai K, Mim MS, Flores-Flores M, Chen W, Zartman JJ, Alber M: Balancing competing effects of tissue growth and cytoskeletal regulation during Drosophila wing disc development. *Nat Commun* 2024, 15.

175. Lim Y, Shiver AL, Khariton M, Lane KM, Ng KM, Bray SR, Qin J, Huang KC, Wang B: Mechanically resolved imaging of bacteria using expansion microscopy. *PLoS Biol* 2019, 17.

176. Rieder F, Brenmoehl J, Leeb S, Schölmerich J, Rogler G: Wound healing and fibrosis in intestinal disease. *Gut* 2007, 56:130–139.

177. Betensley A, Sharif R, Karamichos D: A systematic review of the role of dysfunctional wound healing in the pathogenesis and treatment of idiopathic pulmonary fibrosis. *J Clin Med* 2017, 6.

178. Martin-Bermudo MD, Brown NH: *Uncoupling integrin adhesion and signaling: the PS cytoplasmic domain is sufficient to regulate gene expression in the Drosophila embryo*. 1999.

179. Guha A, Sriram V, Krishnan KS, Mayor S: shibire mutations reveal distinct dynamin-independent and -dependent endocytic pathways in

primary cultures of Drosophila hemocytes. *J Cell Sci* 2003, 116:3373–3386.

180. Chen ML, Green D, Liu L, Lam YC, Mukai L, Rao S, Ramagiri S, Krishnan KS, Engel JE, Lin JJC, et al.: Unique biochemical and behavioral alterations in Drosophila shibirets1 mutants imply a conformational state affecting dynamin subcellular distribution and synaptic vesicle cycling. *J Neurobiol* 2002, 53:319–329.

181. Brand AH, Perrimon N: Targeted gene expression as a means of altering cell fates and generating dominant phenotypes. *Development* 1993, 118:401–415.

182. Klein T: Immunolabeling of Imaginal Discs. In *Drosophila: Methods and Protocols*. Edited by Dahmann C. Humana Press; 2008:253–263.

183. Rosario M Del, Gómez-De-Mariscal E, Morgado L, Portela R, Jacquemet G, Pereira PM, Henriques R: PhotoFiTT: A Quantitative Framework for Assessing Phototoxicity in Live-Cell Microscopy Experiments. *bioRxiv* 2024, doi:10.1101/2024.07.16.603046.

184. Schindelin J, Arganda-Carreras I, Frise E, Kaynig V, Longair M, Pietzsch T, Preibisch S, Rueden C, Saalfeld S, Schmid B, et al.: Fiji: An open-source platform for biological-image analysis. *Nat Methods* 2012, 9:676–682.

185. napari contributors: napari: a multi-dimensional image viewer for python. 2019, doi:10.5281/zenodo.3555620.

186. Kasza KE, Zallen JA: Dynamics and regulation of contractile actin-myosin networks in morphogenesis. *Curr Opin Cell Biol* 2011, 23:30–38.

187. Duda M, Kirkland NJ, Khalilgharibi N, Tozluoglu M, Yuen AC, Carpi N, Bove A, Piel M, Charras G, Baum B, et al.: Polarization of Myosin II Refines Tissue Material Properties to Buffer Mechanical Stress. *Dev Cell* 2019, 48:245-260.e7.

188. Mary H, Brouhard GJ: Kappa (κ): Analysis of Curvature in Biological Image Data using B-splines. 2019, doi:10.1101/852772.

189. Stringer C, Wang T, Michaelos M, Pachitariu M: Cellpose: a generalist algorithm for cellular segmentation. *Nat Methods* 2021, 18:100–106.

190. Prabhakara C, Swaminathan Iyer K, Rao M, Saunders TE: Quantitative analysis of three-dimensional cell organisation and concentration profiles within curved epithelial tissues. *bioRxiv* 2022, doi:10.1101/2022.05.16.492131.

191. Gómez HF, Dumond MS, Hodel L, Vetter R, Iber D: 3D cell neighbour dynamics in growing pseudostratified epithelia. *Elife* 2021, 10.

192. Kusaka EM, Ostvar S, Wang X, Liu X, Kasza KE: Cell rearrangement progression along the apical-basal axis is linked with 3D epithelial tissue structure. *bioRxiv* 2024, doi:10.1101/2024.04.29.591620.

193. Theodosiou NA, Xu T: *Use of FLP/FRT System to Study Drosophila Development*. 1998.

194. Porfírio-Rodrigues P, Pereira T, Jacinto A, Carvalho L: Dachsous is a key player in epithelial wound closure through modulating cell shape changes and tissue mechanics. *J Cell Sci* 2025, 138.

195. Bendix PM, Koenderink GH, Cuvelier D, Dogic Z, Koeleman BN, Brieher WM, Field CM, Mahadevan L, Weitz DA: A quantitative analysis of contractility in active cytoskeletal protein networks. *Biophys J* 2008, 94:3126–3136.

196. Ershov D, Phan MS, Pylvänäinen JW, Rigaud SU, Le Blanc L, Charles-Orszag A, Conway JRW, Laine RF, Roy NH, Bonazzi D, et al.: TrackMate 7: integrating state-of-the-art segmentation algorithms into tracking pipelines. *Nat Methods* 2022, 19:829–832.

197. Kroeger B, Manning SA, Fonseka Y, Oorschot V, Crawford SA, Ramm G, Harvey KF: Basal spot junctions of Drosophila epithelial tissues respond to morphogenetic forces and regulate Hippo signaling. *Dev Cell* 2024, 59:262-279.e6.

198. Brown NH, Gregory SL, Rickoll WL, Fessler LI, Prout M, White RAH: Talin Is Essential for Integrin Function in Drosophila. *Dev Cell* 2002, 3:569–579.

199. Steib E, Tetley R, Laine RF, Norris DP, Mao Y, Vermot J: TissUExM enables quantitative ultrastructural analysis in whole vertebrate embryos by expansion microscopy. *Cell Reports Methods* 2022, 2.

200. Chen F, Tillberg PW, Boyden ES: Expansion microscopy. *Science (1979)* 2015, 347:543–548.

201. Chang JB, Chen F, Yoon YG, Jung EE, Babcock H, Kang JS, Asano S, Suk HJ, Pak N, Tillberg PW, et al.: Iterative expansion microscopy. *Nat Methods* 2017, 14:593–599.

202. Tillberg PW, Chen F, Piatkevich KD, Zhao Y, Yu CC, English BP, Gao L, Martorell A, Suk HJ, Yoshida F, et al.: Protein-retention expansion microscopy of cells and tissues labeled using standard fluorescent proteins and antibodies. *Nat Biotechnol* 2016, 34:987–992.

203. Klimas A, Gallagher BR, Wijesekara P, Fekir S, DiBernardo EF, Cheng Z, Stolz DB, Cambi F, Watkins SC, Brody SL, et al.: Magnify is a universal molecular anchoring strategy for expansion microscopy. *Nat Biotechnol* 2023, 41:858–869.

204. Ku T, Swaney J, Park JY, Albanese A, Murray E, Hun Cho J, Park YG, Mangena V, Chen J, Chung K: Multiplexed and scalable super-resolution imaging of three-dimensional protein localization in size-adjustable tissues. *Nat Biotechnol* 2016, 34:973–981.

205. Gambarotto D, Zwettler FU, Le Guennec M, Schmidt-Cernohorska M, Fortun D, Borgers S, Heine J, Schloetel JG, Reuss M, Unser M, et al.: Imaging cellular ultrastructures using expansion microscopy (U-ExM). *Nat Methods* 2019, 16:71–74.

206. Yu C-C, Orozco Cosio DM, Boyden ES: ExCel: Super-Resolution Imaging of C. elegans with Expansion Microscopy. 2022:141–203.

207. Yu CC, Barry NC, Wassie AT, Sinha A, Bhattacharya A, Asano S, Zhang C, Chen F, Hobert O, Goodman MB, et al.: Expansion microscopy of c. Elegans. *Elife* 2020, 9:1–78.

208. Chozinski TJ, Mao C, Halpern AR, Pippin JW, Shankland SJ, Alpers CE, Najafian B, Vaughan JC: Volumetric, Nanoscale Optical Imaging of Mouse and Human Kidney via Expansion Microscopy. *Sci Rep* 2018, 8.

209. Sim J, Park CE, Cho I, Min K, Eom M, Han S, Jeon H, Cho H-J, Cho E-S, Kumar A, et al.: Nanoscale resolution imaging of the whole mouse embryos and larval zebrafish using expansion microscopy. [date unknown], doi:10.1101/2021.05.18.443629.

210. Bissen D, Kracht MK, Foss F, Acker-Palmer A: Expansion microscopy of mouse brain organotypic slice cultures to study protein distribution. *STAR Protoc* 2022, 3.

211. Jiang N, Kim HJ, Chozinski TJ, Azpurua JE, Eaton BA, Vaughan JC, Parrish JZ: Superresolution imaging of Drosophila tissues using expansion microscopy. *Mol Biol Cell* 2018, 29:1413–1421.

212. Wainman A: Expansion microscopy on Drosophila spermatocyte centrioles. In *Methods in Cell Biology*. . Academic Press Inc.; 2021:217–245.

213. Freifeld L, Odstrcil I, Förster D, Ramirez A, Gagnon JA, Randlett O, Costa EK, Asano S, Celiker OT, Gao R, et al.: Expansion microscopy of zebrafish for neuroscience and developmental biology studies. *Proc Natl Acad Sci U S A* 2017, 114:E10799–E10808.

214. Seehra RS, Warrington SJ, Allouis BHK, Sheard TMD, Spencer ME, Shakespeare T, Cadby A, Bose D, Strutt D, Jayasinghe I: Geometry-preserving expansion microscopy microplates enable high-fidelity nanoscale distortion mapping. *Cell Rep Phys Sci* 2023, 4.

215. Hooper SL, Hobbs KH, Thuma JB: Invertebrate muscles: Thin and thick filament structure; molecular basis of contraction and its

regulation, catch and asynchronous muscle. *Prog Neurobiol* 2008, 86:72–127.

216. Daneshparvar N, Taylor DW, O'Leary TS, Rahmani H, Abbasiyeganeh F, Previs MJ, Taylor KA: CryoEM structure of Drosophila flight muscle thick filaments at 7 A resolution. *Life Sci Alliance* 2020, 3.

217. Huff J: The Airyscan detector from ZEISS: confocal imaging with improved signal-to-noise ratio and super-resolution. *Nat Methods* 2015, 12:ii.

218. Wu X, Hammer JA: ZEISS airyscan: optimizing usage for fast, gentle, super-resolution imaging. In *Methods in Molecular Biology*. . Humana Press Inc.; 2021:111–130.

219. Hennig S, Manstein DJ: Improvement of image resolution by combining enhanced confocal microscopy and quantum dot triexciton imaging. *FEBS Open Bio* 2021, 11:3324–3330.

220. Patterson GH, Piston DW: Photobleaching in two-photon excitation microscopy. *Biophys J* 2000, 78:2159–2162.

221. Chen TS, Zeng SQ, Luo QM, Zhang ZH, Zhou W: High-order photobleaching of Green fluorescent protein inside live cells in Two-photon excitation microscopy. *Biochem Biophys Res Commun* 2002, 291:1272–1275.

222. Damstra HGJ, Passmore JB, Serweta AK, Koutlas I, Burute M, Meye FJ, Akhmanova A, Kapitein LC: GelMap: intrinsic calibration and deformation mapping for expansion microscopy. *Nat Methods* 2023, 20:1573–1580.

223. Schueder F, Mangeol P, Chan EH, Rees R, Schünemann J, Jungmann R, Görlich D, Schnorrer F: Nanobodies combined with DNA-PAINT super-resolution reveal a staggered titin nanoarchitecture in flight muscles. *Elife* 2023, 12.

224. Lemke SB, Weidemann T, Cost AL, Grashoff C, Schnorrer F: A small proportion of talin molecules transmit forces at developing muscle attachments in vivo. *PLoS Biol* 2019, 17.

225. Antunes M, Pereira T, Cordeiro J V., Almeida L, Jacinto A: Coordinated waves of actomyosin flow and apical cell constriction immediately after wounding. *Journal of Cell Biology* 2013, 202:365–379.

226. Martin AC, Goldstein B: Apical constriction: Themes and variations on a cellular mechanism driving morphogenesis. *Development (Cambridge)* 2014, 141:1987–1998.

227. Murrell M, Oakes PW, Lenz M, Gardel ML: Forcing cells into shape: The mechanics of actomyosin contractility. *Nat Rev Mol Cell Biol* 2015, 16:486–498.

228. Shellard A, Mayor R: Sculpting with stiffness: rigidity as a regulator of morphogenesis. *Biochem Soc Trans* 2023, 51:1009–1021.

229. Cai D, Chen SC, Prasad M, He L, Wang X, Choesmel-Cadamuro V, Sawyer JK, Danuser G, Montell DJ: Mechanical feedback through E-cadherin promotes direction sensing during collective cell migration. *Cell* 2014, 157:1146–1159.

230. Liang X, Michael M, Gomez G: Measurement of Mechanical Tension at cell-cell junctions using two-photon laser ablation. *Bio Protoc* 2016, 6.

231. Gómez-González M, Latorre E, Arroyo M, Trepat X: Measuring mechanical stress in living tissues. *Nature Reviews Physics* 2020, 2:300–317.

232. Ham TR, Collins KL, Hoffman BD: Molecular tension sensors: moving beyond force. *Curr Opin Biomed Eng* 2019, 12:83–94.

233. Sugimura K, Lenne PF, Graner F: Measuring forces and stresses in situ in living tissues. *Development (Cambridge)* 2016, 143:186–196.

234. Kumar A, Ouyang M, Van den Dries K, McGhee EJ, Tanaka K, Anderson MD, Groisman A, Goult BT, Anderson KI, Schwartz MA: Talin tension sensor reveals novel features of focal adhesion force

transmission and mechanosensitivity. *Journal of Cell Biology* 2016, 213:371–383.

235. Yao M, Goult BT, Chen H, Cong P, Sheetz MP, Yan J: Mechanical activation of vinculin binding to talin locks talin in an unfolded conformation. *Sci Rep* 2014, 4.

236. Austen K, Ringer P, Mehlich A, Chrostek-Grashoff A, Kluger C, Klingner C, Sabass B, Zent R, Rief M, Grashoff C: Extracellular rigidity sensing by talin isoform-specific mechanical linkages. *Nat Cell Biol* 2015, 17:1597–1606.

237. Grashoff C, Hoffman BD, Brenner MD, Zhou R, Parsons M, Yang MT, McLean MA, Sligar SG, Chen CS, Ha T, et al.: Measuring mechanical tension across vinculin reveals regulation of focal adhesion dynamics. *Nature* 2010, 466:263–266.

238. Shrestha D, Jenei A, Nagy P, Vereb G, Szöllősi J: Understanding FRET as a research tool for cellular studies. *Int J Mol Sci* 2015, 16:6718–6756.

239. Berney C, Danuser G: FRET or no FRET: A quantitative comparison. *Biophys J* 2003, 84:3992–4010.

240. Bajar BT, Wang ES, Zhang S, Lin MZ, Chu J: A guide to fluorescent protein FRET pairs. *Sensors (Switzerland)* 2016, 16.

241. Hachet-Haas M, Converset N, Marchal O, Matthes H, Gioria S, Galzi JL, Legat S: FRET and colocalization analyzer - A method to validate measurements of sensitized emission FRET acquired by confocal microscopy and available as an ImageJ plug-in. *Microsc Res Tech* 2006, 69:941–956.

242. Roszik J, Lisboa D, Szöllosi J, Vereb G: Evaluation of intensity-based ratiometric FRET in image cytometry - Approaches and a software solution. *Cytometry Part A* 2009, 75:761–767.

243. Eder D, Basler K, Aegerter CM: Challenging FRET-based E-Cadherin force measurements in Drosophila. *Sci Rep* 2017, 7.

244. Pachitariu M, Stringer C: Cellpose 2.0: how to train your own model. *Nat Methods* 2022, doi:10.1038/s41592-022-01663-4.

245. Klapholz B, Herbert SL, Wellmann J, Johnson R, Parsons M, Brown NH: Alternative mechanisms for talin to mediate integrin function. *Current Biology* 2015, 25:847–857.

246. Camp D, Venkatesh B, Solianova V, Varela L, Goult BT, Tanentzapf G: The actin binding sites of talin have both distinct and complementary roles in cell-ECM adhesion. *PLoS Genet* 2024, 20.

247. Owen LM, Bax NA, Weis WI, Dunn AR: The C-terminal actin-binding domain of talin forms an asymmetric catch bond with F-actin. *PNAS* 2022, 119.

248. Hopt A, Neher E: *Highly Nonlinear Photodamage in Two-Photon Fluorescence Microscopy*. 2001.

249. Sui L, Dahmann C: Increased lateral tension is sufficient for epithelial folding in Drosophila. *Development (Cambridge)* 2020, 147.

250. Skorentseva K V., Bolshakov F V., Saidova AA, Lavrov AI: Regeneration in calcareous sponge relies on ‘purse-string’ mechanism and the rearrangements of actin cytoskeleton. *Cell Tissue Res* 2023, doi:10.1007/s00441-023-03810-5.

251. Ducuing A, Vincent S: The actin cable is dispensable in directing dorsal closure dynamics but neutralizes mechanical stress to prevent scarring in the Drosophila embryo. *Nat Cell Biol* 2016, 18:1149–1160.

252. White JS, Su JJ, Ruark EM, Hua J, Hutson MS, Page-McCaw A: Wound-Induced Syncytia Outpace Mononucleate Neighbors during Drosophila Wound Repair. *bioRxiv* 2023, doi:10.1101/2023.06.25.546442.

253. Rothenberg KE, Fernandez-Gonzalez R: Forceful closure: cytoskeletal networks in embryonic wound repair. *Mol Biol Cell* 2019, 30:1353–1574.

254. Korkmazhan E, Kennard AS, Garzon-Coral C, Vasquez CG, Dunn AR: Tether-guided lamellipodia enable rapid wound healing. *Biophys J* 2022, 121:1029–1037.

255. Ferguson SM, De Camilli P: Dynamin, a membrane-remodelling GTPase. *Nat Rev Mol Cell Biol* 2012, 13:75–88.

256. van der Bliek AM, Meyerowrtz EM: Dynamin-like protein encoded by the Drosophila shibire gene associated with vesicular traffic. *Nature* 1991, 351:411–414.

257. Goult BT, Yan J, Schwartz MA: Talin as a mechanosensitive signaling hub. *Journal of Cell Biology* 2018, 217:3776–3784.

258. Haage A, Goodwin K, Whitewood A, Camp D, Bogutz A, Turner CT, Granville DJ, Lefebvre L, Plotnikov S, Goult BT, et al.: Talin Autoinhibition Regulates Cell-ECM Adhesion Dynamics and Wound Healing In Vivo. *Cell Rep* 2018, 25:2401-2416.e5.

259. Ellis SJ, Goult BT, Fairchild MJ, Harris NJ, Long J, Lobo P, Czerniecki S, Van Petegem F, Schöck F, Peifer M, et al.: Talin autoinhibition is required for morphogenesis. *Current Biology* 2013, 23:1825–1833.

260. Park SH, Lee C wool, Lee JH, Park JY, Roshandell M, Brennan CA, Choea KM: Requirement for and polarized localization of integrin proteins during Drosophila wound closure. *Mol Biol Cell* 2018, 29:2137–2147.

261. Verma D, Meng F, Sachs F, Hua SZ: Flow-induced focal adhesion remodeling mediated by local cytoskeletal stresses and reorganization. *Cell Adh Migr* 2015, 9:432–440.

262. Dede Eren A, Lucassen AWA, Tuvshindorj U, Truckenmüller R, Giselbrecht S, Eren ED, Tas MO, Sudarsanam P, de Boer J: Cells Dynamically Adapt to Surface Geometry by Remodeling Their Focal Adhesions and Actin Cytoskeleton. *Front Cell Dev Biol* 2022, 10.

263. Cho E, Irvine KD: Action of fat, four-jointed, dachsous and dachs in distal-to-proximal wing signaling. *Development* 2004, 131:4489–4500.

264. Duffy JB: GAL4 system in Drosophila: A fly geneticist's Swiss army knife. *Genesis (United States)* 2002, 34:1–15.

265. Moe A, Holmes W, Golding AE, Zola J, Swider ZT, Edelstein-Keshet L, Bement W: Cross-talk-dependent cortical patterning of Rho GTPases during cell repair. *Mol Biol Cell* 2021, 32:1417–1432.

266. Abreu-Blanco MT, Verboon JM, Parkhurst SM: Coordination of Rho family GTPase activities to orchestrate cytoskeleton responses during cell wound repair. *Current Biology* 2014, 24:144–155.

267. di Pietro F, Osswald M, De las Heras JM, Cristo I, López-Gay J, Wang Z, Pelletier S, Gaugué I, Leroy A, Martin C, et al.: Systematic analysis of RhoGEF/GAP localizations uncovers regulators of mechanosensing and junction formation during epithelial cell division. *Current Biology* 2023, 33:858-874.e7.

268. Maartens AP, Wellmann J, Wictome E, Klapholz B, Green H, Brown NH: Drosophila vinculin is more harmful when hyperactive than absent, and can circumvent integrin to form adhesion complexes. *J Cell Sci* 2016, 129:4354–4365.

269. Alatortsev VE, Kramerova IA, Frolov M V., Lavrov SA, Westphal ED: Vinculin gene is non-essential in Drosophila melanogaster. *FEBS Lett* 1997, 413:197–201.

270. Neubueser D, Hipfner DR: Overlapping Roles of Drosophila Drak and Rok Kinases in Epithelial Tissue Morphogenesis. *Mol Biol Cell* 2010, 21:2869–2879.

271. Takatsuki H, Bengtsson E, Månsson A: Persistence length of fascin-cross-linked actin filament bundles in solution and the in vitro motility assay. *Biochim Biophys Acta Gen Subj* 2014, 1840:1933–1942.

272. Lamb MC, Anliker KK, Tootle TL: Fascin regulates protrusions and delamination to mediate invasive, collective cell migration in vivo. *Developmental Dynamics* 2020, 249:961–982.

273. Guo H, Swan M, He B: Optogenetic inhibition of actomyosin reveals mechanical bistability of the mesoderm epithelium during Drosophila mesoderm invagination. *Elife* 2022, 11.

274. Herrera-Perez RM, Cupo C, Allan C, Lin A, Kasza KE: Using optogenetics to link myosin patterns to contractile cell behaviors during convergent extension. *Biophys J* 2021, 120:4214–4229.

275. Mackrell AJ, Blumbergtt B, Haynes SR, Fessler JH: *The lethal myospheroid gene of Drosophila encodes a membrane protein homologous to vertebrate integrin 18 subunits*. 1988.

276. Devenport D, Bunch TA, Bloor JW, Brower DL, Brown NH: Mutations in the Drosophila αPS2 integrin subunit uncover new features of adhesion site assembly. *Dev Biol* 2007, 308:294–308.

277. Brower DL, Jaffe SM: Requirement for integrins during Drosophila wing development. *Nature* 1989, 342:285–287.

278. Wilcox M, Diantonio A, Leptin M: *The function of PS integrins in Drosophila wing morphogenesis*. 1989.

279. Zusman S, Patel-King RS, Ffrench-Constant C, Hynes RO: *Requirements for integrins during Drosophila development*. 1990.

280. Brabant MC, Fristrom D, Bunch TA, Brower DL: Distinct spatial and temporal functions for PS integrins during Drosophila wing morphogenesis. *Development* 1996, 122:3307–3317.

281. Tanentzapf G, Martin-Bermudo MD, Hicks MS, Brown NH: Multiple factors contribute to integrin-talin interactions in vivo. *J Cell Sci* 2006, 119:1632–1644.

282. Töpfer U, Santillán KYG, Fischer-Friedrich E, Dahmann C: Distinct contributions of ECM proteins to basement membrane mechanical properties in Drosophila. *Development (Cambridge)* 2022, 149.

283. Ng BF, Selvaraj GK, Mateos CSC, Grosheva I, Alvarez-Garcia I, Martın-Bermudo MD, Palacios IM: α-spectrin and integrins act together to regulate actomyosin and columnarization, and to maintain a

monolayered follicular epithelium. *Development (Cambridge)* 2016, 143:1388–1399.

284. Matejčić M, Salbreux G, Norden C: A non-cell-autonomous actin redistribution enables isotropic retinal growth. *PLoS Biol* 2018, 16.

285. Nyga A, Plak K, Kräter M, Urbanska M, Kim K, Guck J, Baum B: Dynamics of cell rounding during detachment. *iScience* 2023, 26.

286. Sauer FC: Mitosis in the neural tube. *Journal of Comparative Neurology* 1935, 62:377–405.

287. Carroll TD, Langlands AJ, Osborne JM, Newton IP, Appleton PL, Näthke I: Interkinetic nuclear migration and basal tethering facilitates postmitotic daughter separation in intestinal organoids. *J Cell Sci* 2017, 130:3862–3877.

288. Klußmann-Fricke BJ, Martín-Bermudo MD, Llimargas M: The basement membrane controls size and integrity of the Drosophila tracheal tubes. *Cell Rep* 2022, 39.

289. Stringer C, Pachitariu M: Cellpose3: one-click image restoration for improved cellular segmentation. *Nat Methods* 2025, 22:592–599.

290. Lecuit T, Lenne PF: Cell surface mechanics and the control of cell shape, tissue patterns and morphogenesis. *Nat Rev Mol Cell Biol* 2007, 8:633–644.

291. Taffoni C, Omi S, Huber C, Mailfert S, Fallet M, Rupprecht JF, Ewbank JJ, Pujol N: Microtubule plus-end dynamics link wound repair to the innate immune response. *Elife* 2020, 9.